Recent Advances in Perovskites: Processing and Properties

Carlos Moure, Octavio Peña

Recent Advances in Perovskites: Processing and Properties

Carlos Moure [1,*], Octavio Peña [2,*]

[1] *Instituto de Cerámica y Vidrio, CSIC, Electroceramics Department, 28049 Cantoblanco, Madrid, Spain*

[2] *Institut des Sciences Chimiques de Rennes, UMR 6226, Université de Rennes 1, 35042 Rennes, France*

**** Corresponding authors :***

Carlos MOURE / cmoure@icv.csic.es

Octavio PEÑA / octavio.pena@univ-rennes1.fr

phone (OP) : +(33)(0)223236757

Abstract

The perovskite structure is one of the most wonderful to exist in nature. It obeys to a quite simple chemical formula, ABX_3, in which A and B are metallic cations and X, an anion, usually oxygen. The anion packing is rather compact and leaves interstices for large A and small B cations. The A cation can be mono, di or trivalent, whereas B can be a di, tri, tetra, penta or hexavalent cation. This gives an extraordinary possibility of different combinations and partial or total substitutions, resulting in an incredible large number of compounds. Their physical and chemical properties strongly depend on the nature and oxidation states of cations, on the anionic and cationic stoichiometry, on the crystalline structure and elaboration techniques, etc.

In this work, we review the different and most usual crystalline representations of perovskites, from high (cubic) to low (triclinic) symmetries, some well-known preparation methods, insisting for instance, in quite novel and original techniques such as the mechanosynthesis processing. Physical properties are reviewed, emphasizing the electrical (proton, ionic or mixed conductors) and catalytic properties of Mn- and Co-based perovskites ; a thorough view on the ferroelectric properties is presented, including piezoelectricity, thermistors or pyroelectric characteristics, just to mention some of them ; relaxors, microwave and optical features are also discussed, to end up with magnetism, superconductivity and multiferroïsme. Some materials discussed herein have already accomplished their way but others have promising horizons in both fundamental and applied research.

To our knowledge, no much work exists to relate the crystalline nature of the different perovskite-type compounds with their properties and synthesis procedures, in particular with the most recent and newest processes such as the mechanosynthesis approach. Although this is not intended to be a full review of all existing perovskite materials, this report offers a good compilation of the main compounds, their structure and microstructure, processing and relationships between these features.

1. Introduction

The perovskite structure is one of the most wonderful to exist. It belongs to the ternary family of crystalline structures and has a formula ABX_3. It is built from a dense packing of X anions (oxygen preferentially), with two types of sites, one with coordination six and the other with coordination eight or twelve. The octahedral sites can host small cations of one, two, three, four, five or six valence oxidation states, whereas in eight or twelve coordination sites, mono-, di- or tri-valent large-sized cations can be located. The resulting compounds have a wide range of chemical formulae, properties and applications, as summarized in Table 1. Each A cation is surrounded by twelve X anions in a cubic-octahedral coordination, and each B cation is surrounded by six X anions, in an octahedral coordination. Each X anion is surrounded by two B-site cations and four A-site cations (figure 1). Several reviews are devoted to the different aspects of the crystalline perovskite-type compounds [1-4].

Only a few perovskite-type compounds exist in nature. Some of these compounds, their original scientific names and their discovery sites are listed in the following :

Latrappite	$Ca(Fe,Nb)O_3$	Oka, Quebec, Canada
Loparite	$(Na,Ce)TiO_3$	Khibiny, Kola Peninsula, Russia
Lueshite	$NaNbO_3$	Lueshe, Democratic Republic of Congo (former Zaire)
Macedonite	$PbTiO_3$	Crni Kamen, Macedonia
Perovskite	$CaTiO_3$	Zlatoust district, Ural Mountains, Russia
Tausonite	$SrTiO_3$	Murun complex, Yakutia, Russia

The mineral perovskite was discovered in 1839 in the Ural Mountains, Russia, by the German mineralogist and chemist Gustav Rose. It was named in honor of the dignitary, mineralogist and Russian military officer Lev Alexeievitch Perovsky.

In an ideal perovskite structure, as shown in figure 2 for the cubic $SrTiO_3$ oxide, the A cation (Sr) is coordinated to 12 oxygen anions whereas the B (Ti) cations are coordinated to 6 oxygen anions. The A cation is larger than the B cation; the oxygen anions are coordinated to 2 B cations and four A cations. In this way, there is contact between the A, B and O ions. (R_A + R_O) should be equal to $\sqrt{2}(R_B+R_O)$, where R_A, R_B and R_O correspond to the crystal radii for cations A and B and the anion O, respectively.

The stability of a perovskite-type phase for a particular group of cations and anions is related to the so-called "tolerance t" factor. This parameter defines the symmetry of the system and significantly affects its dielectric properties. The tolerance is a variable factor with regard to the limits for the cations size and allows the formation of a perovskite-type phase [1]. It is given by the expression $t = (R_A + R_O)/\sqrt{2}(R_B+R_O)$. When the t value is close to 1, the perovskite phase is formed, although some perovskite structures can form in the range between 0.90 and 1.10, as the cases of $BaZrO_3$ ($t = 1.01$, cubic) and $CaTiO_3$ ($t = 0.97$, pseudo-orthorhombic monoclinic). In the case of B-type complex perovskites $A(B_{0.5}B'_{0.5})O_3$, the above relation is modified to $t = (R_A + R_O)\sqrt{2}[(R_B+R_{B'})/2 + R_O]$.

When the tolerance factor is less than 1, the system is of low symmetry ; t larger than 1 corresponds to big A cations and small B cations, so the B cations have a larger space to move. When t is less than 1, the B cations have a bigger size.

The properties of the perovskite-like compounds as a function of their composition and crystalline structures and symmetries, are very wide. Many perovskite-type compounds are considered ionic compounds, but the bond type is commonly a mixing of ionic and covalent. With regard to the electrical and magnetic features, they may be insulators, ferroelectric compounds, semiconductors, superconductors, metallic conductors, ionic conductors, antiferro-, ferro- or ferrimagnetic compounds, multiferroics. Some examples are given in Table 1.

2. Crystalline structure

Perovskites can crystallize in all possible symmetries, from cubic (high symmetry) to triclinic (very low symmetry). The most typical and important examples are summarized in the following.

2.1 Ideal perovskite as cubic structure

The ideal (cubic) perovskite corresponds to $t = 1$. When t differs from 1, it gives place to perovskites with lower symmetry. The idealized cubic structure is obtained, for instance, in $CaRbF_3$ and $SrTiO_3$. The latter can be described as Sr^{2+} and O^{2-} ions forming a cubic close-packed lattice with Ti^{4+} ions occupying the octahedral holes created by the oxygens. The perovskite structure has a three-dimensional net of corner sharing $[TiO_6]$ octahedra with Sr^{2+} ions in the twelve fold cavities in between the polyhedra (figure 1). In the cubic ABX_3

perovskite structure (a = 0.3905 nm, space group Pm-3m, Z = 1), the A atoms are in Wyckoff position 1b (½,½,½), the B atoms in 1a (0,0,0) and the X atoms in 3d (½,0,0), (0,½,0), (0,0,½), all special positions (figure 2).

The ideal cubic perovskite $SrTiO_3$ has t = 1.00, r_A = 1.44 Å, r_B = 0.605 Å and r_O = 1.40 Å. If the A ion is smaller than the ideal value, then t becomes smaller than 1. As a result, the [BO_6] octahedra will tilt in order to fill the available space. However, the cubic structure occurs even if $0.89 < t < 1$.

2.2 Tetragonal-type perovskite structures

When A is larger, $t > 1$, then the B-O octahedral bond is distorted and an increase along the c-axis occurs. The most typical compound of this class is $BaTiO_3$ (figure 3). It crystallizes with space group P4mm, Z = 1, a_0 = 0.3994 nm and c_0 = 0.4038 nm. The parent compound, $PbTiO_3$, shows a higher distortion. In this latter compound, the increase of the volume of the A cation is combined with the lone-pair nature of the Pb^{2+} cation, leading to one of the largest tetragonality values c_0/a_0 of perovskite-type structures.

2.3 Rhombohedrally distorted perovskite

There are several compounds which show a rhombohedral distortion, one of the most commons being the $LaAlO_3$ compound. The room temperature $LaAlO_3$ structure has a primitive lattice with Z = 2 and a corresponding hexagonal cell with Z = 6. The distortion is, however, small and sometimes it can be described as a face-centered pseudocubic cell, with Z = 8 (figure 4, [5]). Parent compounds are $LnAlO_3$ with Ln = Pr, Ce, Nd. When the ionic radii of the rare-earth cations decrease, the aluminates crystallize with orthorhombic structure.

2.4 Orthorhombic perovskite compounds

Of all the orthorhombically distorted perovskites, the $GdFeO_3$ type is probably the most common one. It crystallizes with space group Pbnm and Z=4. The cell parameters are related to a pseudocubic cell of a´ parameter, by $a_0 \approx b_0 \approx \sqrt{2}a'$ and $c_0 \approx 2a'$.

This structure is very common among ABX_3 perovskite-type compounds, as summarized in the tables of Muller and Roy ; it includes much of $LnMO_3$ compounds in which Ln is a trivalent rare-earth and M a trivalent cation (Al, Fe, Mn, Ga, Cr, V) [1].

The orthorhombically distorted perovskite is a consequence of a low A-cation volume, attaining values for which the 12-fold site is hard to accomplish. To accommodate these cations, the B-X octahedral groups tilt about the pseudo-cubic axes in order to achieve the lowest energy level for the crystal (figure 5). The largest number of distorted perovskites is that of the orthorhombically distorted ones. There are, however, some subtle differences in this group of crystalline structures. Thus, as a function of the change in the tolerance factor (*t*), the so-called O'-type structure, with $c/\sqrt{2} < a < b$, occurs when the tolerance factor is moderately low ; it changes to the so-called O-phase (orthorhombic O-type structure, with $a < c/\sqrt{2} < b$) when a further lowering of the *t*-factor occurs.

2.5 Monoclinic symmetry

The $CaTiO_3$ perovskite shows a distorted monoclinic structure. It exists a controversy about the orthorhombic or monoclinic type of this natural perovskite, however its crystalline structure seems to be rather pseudocubic. A better example of monoclinic structure is the Sr_2GdRuO_6 complex double-perovskite [6,7] (figure 6).

Bismuth-based ferroelectric ceramics are currently under intense investigation for their potential as Pb-free alternatives to lead zirconate titanate-based piezoelectrics. In this respect, one of the most widely studied compositions, $Na_{0.5}Bi_{0.5}TiO_3$ (NBT), has been assumed thus far to exhibit the rhombohedral space group $R3^{-}c$ at room temperature. High-resolution powder X-ray diffraction patterns reveal, however, a peak splitting at room temperature that points toward a monoclinic structure with space group *Cc*. The peak splitting and *Cc* space group are only revealed in sintered powders whereas the calcined powders can be equally fitted by an $R3^{-}c$ model because the microstructure contributes to a peak broadening which obscures the peak splitting [8].

2.6 Triclinic perovskite compounds

The highest degree of distortion is found in compounds such as $BiMnO_3$, in which a lone-pair cation Bi^{3+} is combined with a cation of strong Jahn-Teller character, such as Mn^{3+} (figure 7). Some ordered double-perovskite compounds show also triclinic distortion [9].

Presence of a Mn^{3+} cation with a strong Jahn-Teller effect leads always to crystalline structures with this high degree of distortion. Thus, in $LnMnO_3$ compounds, when the Ln

ionic radius decreases, a hexagonal structure is formed and the perovskite structure is only attained by high-energy procedures [1].

Figure 8 shows the structure of the A-site scandium perovskite $(Sc_{0.94}Mn_{0.06})Mn_{0.65}Ni_{0.35}O_3$ (tilt system $a^+b^-c^-$) synthesized at high pressure. This structure shows two types of A site: large lighter grey (green online) spheres are pure Sc sites, whereas black spheres are mixed Sc/Mn sites. Lighter grey (red online) octahedra represent pure Mn sites, whereas darker grey (blue online) octahedra show mixed Mn/Ni sites. The small light grey spheres show the oxygen positions [10].

3. Processing

Solid-state reaction from oxides, sol-gel, hydrothermal synthesis, high-pressure synthesis, mechanically-activated synthesis and others have been used to prepare perovskite-like compounds. It is important to notice that different procedures may lead to compounds with the same chemical formulation but rather different crystalline symmetry and even different structures. In addition, most of the perovskite-like compounds are polyphasic as a function of temperature, in particular their oxygen content may be function of thermal treatments. For these reasons, well-controlled processing techniques are essential, not only to obtain pure and well-crystallized materials but also, to stabilize metastable phases. Needless to say that, with the recent advances of nanotechnologies, a control of the microstructure is fundamental to elaborate reproducible materials at less costs and lower working temperatures.

Some well-known techniques are reviewed in the following, insisting in rather novel processing such as the mechano-activation which allows preparing crystalline phases not available by some other methods.

3.1 Solid-state synthesis from oxides and carbonates

The first developed technique of synthesis for these oxides is the so-called ceramic route : an intimate mixture of oxides and/or carbonates subjected to heat treatments at high temperatures. The compound is then processed by traditional ceramic powder techniques. A large number of papers deal with the synthesis of ceramic materials by solid state reaction, among them perovskite-type structures with all possible symmetries. However, the solid state synthesis yields powders with poor properties compared to those needed for high-quality ceramic materials. More sophisticated procedures were then developed for the preparation of

technologically interesting perovskites, such as $BaTiO_3$. Some of these methods will be shortly summarized in the following, recalling some of the different problems encountered.

3.2 Mechanosynthesis

One of the most recent procedures to obtain fine particulate compounds is the High Energy Milling, also known as Mechanosynthesis. This technique allows not only the preparation of very fine nanoparticulate powder but also to synthesize, at room temperature, compounds which have been obtained only by high-temperature and/or high-pressure methods. Some examples of this novel technique are detailed below:

- The high energy transferred by the impacts during ball milling allowed single-phase orthorhombic perovskites of $ErMn_{1-x}Ni_xO_3$ (x = 0, 0.1) to be obtained, for the first time, by a straightforward solid-state method. This avoids the application of an external pressure, of the order of GPa, often used to transform the hexagonal stable structure of these compounds to the orthorhombic perovskite structure. Low Ni-doping at the Mn position, helps the perovskite-like structure to be retained, probably due to the reduction of the Jahn-Teller effect. The metastable character of the $ErMn_{1-x}Ni_xO_3$ (x = 0, 0.1) orthorhombic phase, which transforms to the stable hexagonal polymorph at relatively low temperatures, imposes the use of spark plasma sintering (SPS) to obtain high density ceramics (>90%) at low temperatures (~950ºC), always keeping the orthorhombic phase with Pbnm symmetry. This novel technique allowed the grain size to be maintained at the nanoscale range [11,12].
- The influence of the mechanical treatment in the processing of $La_{0.80}Sr_{0.20}Ga_{0.85}Mg_{0.15}O_{2.825}$ and $La_{0.80}Sr_{0.15}Ga_{0.85}Mg_{0.20}O_{2.825}$ ceramics was studied. The mechanosynthesis of these perovskites is achieved after 85 h of milling. When the milling time or the Mg content are increased, the formation of a single-phase perovskite is possible at lower temperatures than those needed by classical solid-state reaction. The solubility of the Sr and Mg dopants at lower temperatures is increased by the effect of prolonged milling [13].
- Energetic milling of a material of nominal composition $Bi_{0.60}Sr_{0.40}FeO_{2.8}$, in stainless-steel media, produces an amorphous and highly reactive ceramic precursor which allows the synthesis to be achieved at 50–100ºC lower temperatures than those needed through classical solid-state methods. The stability of the perovskite phase is increased by the presence of Sr. Ceramics with high relative density (up to 98%) are

obtained at low sintering temperatures (1000–1050ºC) thanks to the high reactivity of the precursors and the eventual aid of a liquid phase. To be noted that the dielectric permittivity increases with respect to the pure bismuth ferrite $BiFeO_3$, due to the influence of the oxygen vacancies. The conductivity is also higher in Sr-doped ceramics, due mainly to the increase of the grain boundary conductivity, a result reported for the first time in these materials [14].

3.3 High-pressure synthesis

A series of samples of the rare-earth (*R*) based hexagonal $RMnO_3$ system was synthesized for *R* = Y and from Ho to Lu, then transformed to the orthorhombic *OP*-$RMnO_3$ perovskites through high-pressure (HP) treatments. The same HP treatment was not adapted for the conversion of hexagonal phases *h*-$InMnO_3$ and *h*-$ScMnO_3$ into perovskites. Thus, the stability limit of the orthorhombic perovskite structure under HP conditions with respect to the ionic radii, $r(R^{III}$ or $In^{III})$, was found to be delimited by $r(In^{III})$ and $r(Lu^{III})$. A systematic study of the structural evolution showed that the progressive reduction of the R^{III} size increases the distortion of the *OP*-$RMnO_3$ perovskites. The Mn-O-Mn bond angle decreases from 144.3º for *OP*-$DyMnO_3$ to 140.3º for *OP*-$LuMnO_3$. The density of the $RMnO_3$ phase increases considerably as the structure changes from hexagonal to orthorhombic, which makes easy to understand why high pressure techniques are specially adapted to the perovskite phase.

Single-crystals of $RMnO_3$, *R* = Y, Ho...Lu were grown with an infrared-heating image furnace in flowing air. A mirror-like facet appearing on one side of the ingots was identified with Laue back-diffraction to be the hexagonal plane normal to the *c* axis. This feature also indicates that the as-grown ingots (5-mm diameter, 50-mm long) are single domain. Ceramic samples of the hexagonal phase were used as starting materials for high-pressure synthesis. Synthesis conditions of 40 kbar and 1000 °C were sufficient to convert the hexagonal phase of all Group II compounds into the perovskite phase [15-18].

3.4 Coprecipitation

Figure 9a shows a flow diagram that exposes briefly the general lines of a coprecipitation process in which different types of precursors are employed : oxides, alkoxides, inorganic salts and nitrates. Controlling the processing parameters (pH, coprecipitation rate, washing, drying and temperature of synthesis) results in homogeneous and weakly agglomerated nanopowders, which can be sintered at near theoretical densities at temperatures as low as

1250 ºC and for short times, 1–2 h, by using an improved coprecipitation procedure. Homogeneous microstructures with near-micron grain sizes are obtained, figure 9b. The hydroxide coprecipitation has been proved to be advantageous against cation oxalates precipitation. The process presented in figure 9a precludes the use of a third cation as a sintering aid, which in some cases could cause undesirable secondary effects. This particular case, referred to the preparation of a modified lead titanate $PbTiO_3$ (M-$PbTiO_3$) as piezoelectric transducer, solves the problem associated to the sintering of strongly distorted tetragonal perovskite [19].

3.5 Sol-gel synthesis of precursors

The Pechini method, quite general to many compounds [20,21], may be exemplified by the particular case presented in figure 10 for the $La_{0.8}Sr_{0.2}FeO_3$ perovskite, as follows : the synthesis is performed weighing all reagents at the stoichiometric ratio La:Sr:Fe of 0.8:0.2:1 under argon in a dry box. Lanthanum oxide, La_2O_3, and strontium carbonate, $SrCO_3$, are converted to the corresponding nitrates by dissolving in concentrated nitric acid. Excess nitric acid is removed by slow heating. Then, $Fe(NO_3)_3.9H_2O$ is added to the solution under stirring. When the iron salt is completely dissolved in the solution, controlled amounts of citric acid (CA) are incorporated and dissolved by stirring in a molar ratio (citric acid-to-total metal ions), of CA:(La+Sr+Fe)=¼:1. The pH of the resultant metal citrate solution is kept to 1. This solution is heated to 80ºC with stirring for 2 h, followed by the addition of ethylene-glycol in a molar ratio of citric acid:ethylene glycol=1:4. The solution is further heated to 130 ºC in an argon flow with a magnetic stirrer heating plate to obtain a viscous solution after about 10 h. Heating and stirring continue until the solution starts to solidify, forming an amber gel-like mass. At this stage, the temperature is raised to 150–200 ºC to obtain a foamy dried mass which is ground in a mortar, followed by overnight drying in a furnace. This precursor is calcined at different temperatures of 600, 850 and 1000 ºC in a muffle furnace to obtain the final product.

4. Properties

4.1 Proton conductivity

4.1.1 Proton conducting Perovskites

Nowick and Du reviewed the various perovskite-structured oxides found to be high-temperature protonic conductors [22]. Authors classified these oxides into two groups: the simple or ABO_3 types and the complex (or mixed) types of formula $A_2B'B''O_6$ and $A_3B'B_2''O_9$. Based on TEM and electron diffraction experiments, the authors pointed out some microstructural features and forwarded a simple "first-order" model for consideration of various fundamental aspects, in particular, the proton incorporation by exposure to water vapor at high temperatures, the environment in which protons are located in the lattice and the nature of proton migration. The proton incorporation was studied by water uptake experiments whereas the proton environment was identified through spectroscopic techniques. In their work, Nowick and Du [22] studied the proton migration through conductivity and isotope-effect experiments, which showed that migration occurred by simple hopping of protons from one O^{2-} ion to the next. However, the classical absolute rate theory (ART) requires modifications because of the low efficiency of energy transfer between an excited proton and the cage of heavy ions surrounding it.

4.1.2 Proton conductivity in oxides (based on works from the Solid State Ionics Research Group, California Institute of Technology, [23] and references therein).

The requirements for an oxide-based proton conductor can be simply stated as:

1) to possess an oxygen deficient lattice, either structurally or via doping,
2) to incorporate water at modest applied vapor pressures (~1 atm), and
3) to allow the rapid transport of protons once these have been formed.

A number of Me^{3+}-doped perovskites ($BaCeO_3$, $BaZrO_3$, $SrZrO_3$; with Me = Y, Gd, Nd or La) exhibit high proton conductivity after exposure to water vapor and thus have a potential use as electrolytes in mid-temperature fuel cells. Many works have been focused on the relationship between microstructure, defect chemistry and proton transport. It has been proved, for instance, that the conductivity of Gd-doped $BaCeO_3$ is highly sensitive to slight changes in stoichiometry, which may occur as a result of extreme processing conditions. However, glassy grain boundary phases, which were predicted to result from either excess barium content or dopant incorporation onto the Ba rather than the Ce sites, are not relevant to the transport mechanism. Transmission electron microscopy studies revealed the grain boundaries in polycrystalline $BaCe_{0.9}Gd_{0.1}O_3$ and $BaCe_{0.85}Gd_{0.15}O_3$ to be free of any secondary phases that could influence the proton transport. In a comprehensive study of the microstructural influence on proton transport, conductivities of samples with grain sizes ranging from 1 to 11 μm have been measured ; it was established that neither the bulk nor the

specific grain boundary conductivity depended on the grain size. Moreover, it was clearly demonstrated that the grain boundary impedance is in fact higher than in the bulk. Thus, for fuel cells and other applications, materials with large grains are preferable in order to minimize the total grain boundary volume and maximize the overall conductivity. Normally, when performing an impedance measurement, an "effective" grain boundary resistance is observed, but it is not possible to convert this value to a specific grain boundary resistivity because the grain size, and thus the number of grain boundaries contributing to the effective resistance, is not known. Under the assumption that the bulk and grain boundary dielectric constants are similar (and they certainly do not differ by more than one order of magnitude), then excellent estimates of the specific grain boundary resistivity can be directly obtained from the impedance data, in the absence of any microstructural knowledge. This has a significant impact since the grain boundary properties of different samples, prepared by different routes, can now be directly compared.

In general, protonic conductors of perovskite structure have attracted much attention over the last few years due to their high applicability in electrochemical devices for energy generation and hydrogen production (figure 11.a). Therefore, the investigation and knowledge of the defect chemistry and proton transport properties in these ceramic electrolytes are of great interest to transfer these possibilities to industrial scale process.

Specifically, for cerates and zirconates with barium in their general formula ($BaCeO_3$ and $BaZrO_3$), the high sintering temperatures typically required have been an obstacle to guarantee the desired stoichiometry and to avoid the deleterious effects on the electrical properties due to barium deficiency. The lack of really effective chemical synthesis and processing techniques for ceramic powder production have become a limiting factor which have led these materials to be so little explored. Obtaining nanoparticles of high surface activity and good control of the morphology might be a great departure for getting ceramic membranes of high relative density at rather low temperatures (< 1300 °C).

Current efforts aim toward improving the chemical stability of barium cerate $BaCeO_3$ in CO_2-rich atmospheres, as well as investigating related chemical systems, with a particular emphasis on developing mixed electron and proton conductors. One example of this is the use of barium zirconate ($BaZrO_3$) as an alternative electrolyte for application purposes. Inserting doping cations, mainly at the B-sites of the $BaCeO_3$ structure, has been used also as an alternative to minimize the chemical reactivity and optimize the ionic conductivity of the

material. Although several reports have commented about the relatively low conductivity of zirconates in relation to barium cerates, some results show that the large electrical resistivity due to the high grain-boundaries density can be reduced via grain growth. Thus, high electrical conductivity (~1 $\times 10^{-2}$ S.cm^{-1}) at intermediate temperatures (450 °C) have been attained for both $BaCeO_3$- and $BaZrO_3$-based compounds, placing the proton conductors with perovskite structure among the most studied ceramic solid electrolytes.

In this context, four proton conducting oxides of perovskite structure, $BaZrO_3$, $SrZrO_3$, $BaCeO_3$ and $SrCeO_3$, doped with 5 mol.% of gadolinium, were studied by the Caltech group [23], who compared the crystal structure, microstructure, sinterability, water sorption ability, ionic transference number, electrical conductivity and stability towards CO_2. The authors discussed the relations between proton conductivity, structural and chemical parameters (pseudo-cubic unit cell volume, lattice free volume, tolerance factor, crystal symmetry and electronegativity). The grain boundary resistance was shown to be the limiting factor of total proton-conductivity. The highest proton conductivity was observed for the Gd-doped $BaCeO_3$ specimen ; however, it turned out to be prone to degradation in CO_2-containing atmosphere and reduction at high temperatures. Better results were obtained when doping Er^{3+} in $BaCeO_3$ and co-doping with Yb^{3+} and Sc^{3+}, improving the chemical stability of the perovskite phase in CO_2 atmosphere. On the other hand, Ba and Sr zirconates, more chemically stable, exhibit low electrical conductivity. Electrical conductivity relaxation upon hydration is used to calculate proton diffusion coefficient. Selected materials were tested as electrolytes in solid oxide fuel cells.

Acceptor-doped $BaZrO_3$ perovskites are known to exhibit high bulk proton conductivity in the range of 300-700°C in humid atmosphere. However, grain boundaries severely lower the overall conductivity and thus decrease the performance of devices such as solid oxide fuel cells (SOFC). Chemically-stable high-temperature proton conductors, in particular electrolytes based on Y-doped $BaZrO_3$, are extremely promising for applications in SOFCs operating at reduced temperatures, i.e., 600 °C and below. The advances made on improving the sinterability of powders, bringing the sintering temperatures at values similar to those needed for yttria-stabilized zirconia (YSZ) and allowing powder-based and low-cost fabrication technologies compatible with mass production, encourage the development of a next generation of anode-supported SOFCs based on proton-conducting electrolytes, operating at 600 °C with hydrogen or even hydrocarbon and alcohol fuels (figure 11.b) [24-37].

4.2 Ionic conductors $LaGaO_3$ solid solutions [38,39]

Ceramics of $La_{1-x}Sr_xGa_{1-y}Mg_yO_{3-\delta}$ composition are good candidates to be used as electrolytes in SOFC applications at intermediate temperatures (700–1000ºC). Doping the $LaGaO_3$ perovskite with Sr (in La-sites) and Mg (in Ga sites) provokes oxygen vacancies, resulting in high conductivity values ($\sigma > 0.10$ S cm^{-1} at 800 ºC). These compositions have negligible electronic conduction at $T < 1000$ ºC over a broad range of oxygen partial pressure, from $P(O_2) = 1$ to $\sim 10^{-22}$ atm, and stable performance over long operating times. This results in a better performance of the cell. The highest conductivity obtained in these ceramics corresponds to compositions $x = 0.20$, $y = 0.17$, obtaining values of 0.166 S cm^{-1} at 800 ºC.

The new approach of combining mechanosynthesis and spark plasma sintering (SPS) allowed the elaboration of nanostructured ceramics of $La_{0.90}Sr_{0.10}Ga_{0.80}Mg_{0.20}O_{2.85}$ and $La_{0.80}Sr_{0.20}Ga_{0.83}Mg_{0.17}O_{2.815}$ under conditions not allowed by other processing methods, attaining a quite high densification (> 98%). Thus, the effect of prolonged milling and the external pressure applied during the SPS process yielded single-phase ceramics with higher bulk grain boundary and total conductivity due to the elimination of low-conducting secondary phases, which are partially located at the grain boundaries.

Another consequence of nanostructured ceramics processing when mechanosynthesis and SPS are combined, is the reduction of the activation energy of the conductivity, indicating that typical defect–vacant associations are not favored in such nanostructures. In addition, the high diffusivity of the grain boundaries results in high conductivities and low activation energies that make possible to reduce the working temperature of these devices [40-46]. Thus, this original approach constitutes a good alternative for processing materials as electrolytes in SOFC applications which can successfully operate at intermediate temperatures (600 ºC-800 ºC).

4.3 Mixed conductors $LaMeO_3$ solid solutions

A simple model presents a solid as a collection of weakly interacting atoms in which the atomic forces overlap enough to require corrections to a scheme of isolated atoms, but not so much as to discard the atomic description. This model may apply for bands from transition metal elements, with partially-filled d-levels. The basic idea is that, when the interaction between orbitals decreases, the bands become narrow, the conductivity decreases and finally localized states are attained [47].

The A cations present in oxides of perovskite structure have basic character and, in a first approximation, do not sufficiently interact with the O^{2-} anion or with the B cation to affect the band structure around the Fermi level. Thus, the only role of the A cations would be to donate electrons which would be integrated in the band. However there are a number of issues to be considered :

a) The A cations compete with the B ones to bond the p-orbital of the anion. If an A-O bond occurs, the π* band does not exist. Experimentally, it has been observed that, the greater the acidic nature of cation A, the narrower is the band,

b) Higher valence A cations correspond to lower valence B cations (lower λ_π) and tend to further narrow the π* band,

c) The greater is the overlap integral, the higher is the radial extension of the d-orbitals of cation B. This implies that bonds with oxygen lead to the formation of bands which, in the previous model, can be not formed,

d) The B cations can be promoted to a high-spin state as a result of magnetic exchange interaction, narrowing the σ* (e_g) band ; they can appear as localized states at the atomic levels e_g.

These issues are at the base of a molecular orbital model, highly simplistic but proved to be a reasonable approximation. In this scheme, the ABO_3 perovskites with d^1-d^5 or d^7-d^9 configuration will present a π* or σ* (e_g) band partially filled and of metallic conduction.

Taking as reference the overlap integrals, a critical value, Δ_{crit}, was established by Goodenough [48]. Above this value, the theory of collective electrons applies and below it, the theory of localized electrons. On this basis, oxides can be classified into three groups, in which the overlapping integrals are the following : Δ_{cc} (cation-cation bonding), Δ^{σ}_{cac} (cation-anion-cation bonding by means of σ bonds), $\Delta^{\pi\sigma}_{cac}$ (by means of π and σ bonds), Δ^{π}_{cac} (idem, through π bonds) :

a) Class 1 – oxides in which $\Delta^{\sigma}_{cac} > \Delta_{crit}$ ($\Delta_{cac} < \Delta_{crit}$) for all the occupied d-orbital ; therefore, it has a d-band of states on the subnetwork of cations and is partially full,

b) Class 2a – those where $\Delta^{\sigma}_{cac} > \Delta_{crit}$ (but $\Delta_{cc} < \Delta'_{crit}$); they show narrow and partially filled band,

c) Class 2b – those where $\Delta^{\pi}_{cac} > \Delta_{crit}$ (but $\Delta_{cc} < \Delta'_{crit}$) ; narrow and partially filled bands.

One of the most important questions in SOFC processing is the nature of the cathode material. Precious metals such as Pt, which are excellent conductors and catalyzers, are enormously expensive. If cheaper materials are to be used, they should be stable against oxygen and capable to work at elevated temperatures, 600-800 ºC, without corrosion. Ceramic materials, with adequate conductivity at those temperatures, proved to be a solution for this problem. Among the cathode materials, $(La,Sr)MnO_3$ (LSM)-based perovskites are the most extensively studied and investigated compounds for O_2 reduction due to their high stability and high electrocatalytic activity at the triple point gas-electrode-electrolyte at high temperatures. To improve their properties, significant work has been done to establish the mechanisms and kinetics of the O_2 reduction and to know their electrode behavior under fuel-cell operation conditions. A general consensus is now accepted on the O_2 reduction on LSM electrodes ; the main mechanism is a surface-controlled oxygen-dissociative adsorption process, gas-phase O_2 diffusion and oxygen diffusion at the LSM surface. $(La,Sr)MnO_3$ is a predominant electronic conductor with non-negligible oxygen-ion conductivity which favors the catalytic process. Studies of the geometry dependence of the cathode potential on a well-defined thin LSM microelectrode have shown that the polarization resistance varies inversely with the area of the electrodes. It has been proved that the reaction is related to the surface area or the electrolyte interface area of the LSM material.

A good review on the state-of-the-art was carried out by Jiang on the earliest 2000 [49], and it is a good base to initiate in this area.

One of the most important problems found by the use of $(La,Sr)MnO_3$ materials in some SOFC devices is the reaction at the cathode/electrolyte interface, as for instance in the LSM electrode|Y_2O_3–ZrO_2 (YSZ). At the working temperature, a reaction between Zr and La occurs, forming lanthanum zirconium pyrochlore, which is insulator. The formation of such a resistive lanthanum zirconate phase is closely related to the stoichiometric composition of LSM materials. On the other hand, manganese in the $(La,Sr)MnO_3$ perovskite structure is known to be mobile at high temperatures and under cathodic polarization potentials, with significant effects on the interfacial properties of cathode and electrolyte. One of the procedures to overcome these inconveniences is to use some parent rare-earth manganites,

such as (Sm,Sr)MnO_3 or (Nd,Sr)MnO_3 manganite perovskites. They show lower electrical conductivities but a higher chemical stability.

Cobaltites are known to be mixed ionic–electronic conductors (MIEC). As an example, the electronic conductivity of $La_{1-x}Sr_xCoO_{3-\delta}$ is above 1000 S/cm at 800 ºC, while the ionic conductivity is between 0.1 and 1 S/cm. MIECs are very attractive candidates for cathodes of solid oxide fuel cells (SOFCs), in which oxygen and hydrogen are converted into electrical energy and water ($2H_2 + O_2 \rightarrow 2H_2O$ + energy) at temperatures in the range of 700–1000ºC. At the cathode side of the fuel cell, oxygen gas is adsorbed and dissociated. The oxygen takes up two electrons from an outer current circuit ; then, the negatively charged oxygen ions move towards and through the electrolyte to the anode. Hence, a suitable cathode should conduct electrons as well as oxygen ions, and its surface must be capable of reacting with oxygen gas. Cobaltites fulfill these demands. The main drawback of cobaltites as cathodes for SOFCs is the very high coefficient of thermal expansion, about 20×10^{-6} K^{-1}, compared to the current state-of-the-art electrolyte yttria stabilized zirconia, YSZ, 10.5×10^{-6} K^{-1}, which results in high mechanical stresses, especially during thermal cycling [50-55].

4.4 Catalytic properties

Fe-based perovskites are low-cost alternatives to partly replace noble metals in conventional 3-way catalysts. Optimization of the surface composition strongly enhances the catalytic activity of the perovskite by increasing the accessibility of the active sites. Cu and Ca doping increase the catalytic activity, especially CO oxidation, which can avoid the CO inhibition on noble metals. Combination of partial substitution, non-stoichiometric formulation and low loading with noble metals allows promising catalytic performances in 3-way catalysis (see chapters 9 and 13 in ref. [3]).

One of their applications is the total oxidation of hydrocarbons. The perovskite-type oxides with partly-substituted A and/or B sites can desorb or adsorb a large amount of oxygen. Thus, several compositions with perovskite-type structure, such as $LaMO_3$ (M = Co, Mn, Fe, Cu, Ni, Cr), show good values for oxidation of methane although lower than the Pt catalyst. However, when La is partially substituted by Sr^{2+}, the catalytic activity strongly increases. Co- and Mn-based perovskites are the most interesting compounds for this application.

Another possible application as catalytic materials is in heterogeneous catalysis. Thus, the hydrogen-involving reactions, such as hydrogenation and hydrogenolysis of hydrocarbons can

be the field of applications of some pure compounds $LaMO_3$ (M = Co, Fe, Al). Hydrogenolysis of some alkenes such as propene and butane, and alkanes such as the C_3_C_5 ones, are well catalyzed in presence of $LaCoO_3$.

In 1971, W. F. Libby [56] had suggested that the $LaCoO_3$ perovskite might be a good catalyst for treating auto-exhaust gases by favoring the simultaneous reactions of CO oxidation and NO reduction.

$SrTiO_3$ has proved to be a good photocatalyst material for decomposing water in H_2 and O_2 with a suitable yield.

Finally, reduction of SO_2 to avoid poisoning of other catalytic systems has been studied by using $La_{0.5}Sr_{0.5}CoO_3$ perovskite and other parent compounds under the form of solid solutions.

Among all the studied perovskites, $LaNiO_3$ exhibit high activity and selectivity without coke formation. Among Fe-substituted catalysts, the following order of activity was observed : $LaNiO_3$ > $LaNi_{0.4}Fe_{0.6}O_3$ > $LaNi_{0.6}Fe_{0.4}O_3$ > $LaNi_{0.8}Fe_{0.2}O_3$ > $LaNi_{0.2}Fe_{0.8}O_3$ > $LaFeO_3$ [2, 57-67].

As an example of catalytic perovskites, the calcium-doped lanthanum cobaltite ($La_{1-x}Ca_xCoO_3$) with different concentrations (x = 0, 0.2, 0.4, 0.6, 0.8), was prepared by a modified Pechini-type polymerizable method. Their X-ray diffraction patterns showed the formation of a cubic structure. Scanning electron and transmission electron microscopies showed the porous nature of the prepared material. Conductance spectra revealed a frequency-independent behavior and a conductivity related to the particle size. A sample doped with 0.6% of calcium is found to show high conductivity. The conductivity indicated an Arrhenius type behavior [65].

4.5 Ferroelectricity

Ferroelectricity is a property of certain materials to have a spontaneous polarization which can be reversed by the application of an external electric field. Ferroelectricity was discovered in 1920 in Rochelle Salts by J. Valasek [68]. The term is used by analogy to ferromagnetism in which a material exhibits a permanent magnetic moment. Thus, the prefix *ferro*, meaning iron, was used despite the fact that most ferroelectric materials do not contain iron.

Ferroelectric materials show a spontaneous nonzero polarization even when the applied field E is zero. The outstanding feature of ferroelectrics is that the spontaneous polarization can be reversed by a strong applied electric field in the opposite direction ; the polarization is therefore dependent not only on the current electric field but also on its history, yielding hysteresis loops.

As a consequence of ferroelectricity, many polycrystalline (ceramic) materials show a series of derivative properties making very interesting their development and applications. $BaTiO_3$ is the most widely used ferroelectric material being the first oxide compound with ferroelectric behavior. Its structure, first studied by Megaw [69] and others [70,71], is of perovskite-type.

A great controversy exists, even in more recent times, about the origin of ferroelectricity in oxide compounds. Several mechanisms have been forwarded to explain the ferroelectric behavior : presence of lone-pair cations (Pb^{2+},Bi^{3+}), shift from the equilibrium site (Ti^{4+}) and others. Bussmann-Holder compiled a comprehensive review in 2012 [72]. The author concluded that "unconventional polarizability of the oxygen ion and its homologues is certainly not only playing an essential role for perovskite ferroelectrics but should also be taken into account when physics of other oxides are considered".

Table 2 lists some of the properties and applications associated to ferroelectricity.

4.5.1 Piezoelectric perovskites [73]

In ferroelectric materials the polar axes also have a random orientation after synthesis and sintering ; however, these polar axes can be reoriented under the influence of an electric field and, as a consequence, an overall orientation remains after polarization.

Piezoelectric ceramics are ferroelectric materials in which the ferroelectric behavior is not observed above a certain temperature called the Curie temperature (T_C). Below that temperature, a ferroelectric transition takes place, inducing a polar axis leading to spontaneous polarization. Therefore the ferroelectric state is at the same time a piezoelectric state.

Barium titanate was the first ferroelectric ceramics used as a piezoelectric material [74,75]. One of the most notorious characteristics of perovskite materials of lower symmetry than the ideal cubic structure is their polymorphism as a function of temperature. Thus, $BaTiO_3$

transforms upon cooling from cubic to tetragonal, then to orthorhombic and finally to a rhombohedral phase (figure 12). At high temperature, $BaTiO_3$ crystallizes in the cubic perovskite-type structure, with Curie temperature of 120 ºC. Then, a first transition takes place and a tetragonal distortion occurs, with the elongated c-axis as polarization axis. Two other transitions take place, the second one at approximately 5 ºC, and the third one at -70 °C with the (011) and (111) directions as new polarization axes.

At the first transition, T_C ~120°C, the six-cubic directions have equal chances to become the polar axis. Below the Curie temperature T_C, a domain structure is formed which can be changed by an external force. For example, by applying an electric field along one of the original cubic axes, all domains can be rotated to form a one-domain single crystal. By changing the sense of the electric field, the polarization switches to the opposite direction. In this way, in an alternating field, the polarization will describe a hysteresis loop (figure 13). Contrary to what occurs in ferromagnetic ceramics, complete saturation of the polarization cannot be achieved in piezoelectric ceramics due to a high distortion of the crystal lattice. In this way, only 30% of saturation polarization can be obtained in $BaTiO_3$ associated with 180° switching only. Its coupling factor is relatively high (K_p = 0.40) and very sensitive to the ceramic microstructure (density, grain size, etc). Other disadvantages of $BaTiO_3$ are the presence of the disturbing second transition temperature at 5°C, and a high temperature coefficient of resonance frequency. In any case, $BaTiO_3$ is a very good piezoelectric ceramic and has been used in many applications. However, the discovery of better piezoelectric properties in the more complex PbO-ZrO_2-TiO_2 system bypasses the disadvantages of the $BaTiO_3$ ceramic materials.

4.5.1.1. Lanthanide-containing piezoelectric $PbTiO_3$ [76]

The piezoelectric characteristics of pure $PbTiO_3$ are very promising and therefore of great interest. Nevertheless, the large tetragonal distortion of its crystalline structure makes almost impossible to prepare ceramic bulks with adequate microstructure. Incorporation of other cations allows overcoming this inconvenience and leads to good piezoelectric materials.

The ferroelectric properties of lead titanates modified by rare earths (La,Nd,Sm,Gd) at the A-site and MnO at the B-site ($Pb_{0.92}La_{0.08}(Ti_{0.98}Mn_{0.02})O_3$) and/or by CaO at the A-site and (Co+W) at the B-site ($Pb_{0.76}Ca_{0.24}((Co_{0.5}W_{0.5})_{0.04}Ti_{0.96})O_3$) were investigated by Durán et al [76]. Their experimental results lead to the following conclusions :

a) The substitution of lead (A site) by rare earths or CaO strongly influences the crystallographic, dielectric and piezoelectric properties of lead titanate ceramic. Thus the addition of 8 mol% lanthanide oxide diminishes the tetragonality of the $PbTiO_3$ perovskite structure, changing monotonically when the rare-earth goes from Gd to La. Such decrease in tetragonality allows the normal sintering of $PbTiO_3$. In the case of the CaO additive, addition of at least 24 mol% was necessary to avoid macrocracking in the sintered samples,

b) Both the Curie temperature (T_C) and the dielectric constant e_T^{33} of $PbTiO_3$ strongly decrease after addition of 8 mol% La_2O_3 or 24 mol% CaO, such a decrease being more pronounced in the case of the CaO addition,

c) The combined addition of (La_2O_3+MnO) or (CaO+(Co+W)) facilitates the poling process of the modified lead titanates. In this way, the calcium-modified lead titanate was sufficiently poled at 35kVcm^{-1}, Sm-lead titanate at 40 to 50kVcm^{-1}, and still higher than 60kVcm^{-1} for the other members of the lanthanide series,

d) The electromechanical coupling factors and the frequency constants are also influenced by these substitutions, changing gradually with increasing tetragonality *(c/a).* In all cases, the longitudinal coupling factor K_t increases with increasing poling field, whereas the planar coupling factor K_p, decreases. In the case of the calcium titanate, K_p was negligible at approximately 50kVcm^{-1} while K_t was as high as 60%. Therefore, the K_t/K_p ratio is probably the largest value reported to date. In the lanthanide oxide series, only Sm-lead titanate showed a reasonably high K_t/K_p ratio, of approximately 20 ; in the other cases, such a ratio was never higher than 5,

e) The large electromechanical anisotropy present in these piezoelectric ceramics makes d_{31} and g_{31} almost negligible and, therefore, the hydrostatic constant d_h can be considered equal to d_{33}. In this way, the figure of merit d_hg_h was as high as 2200 in the case of the calcium-modified lead titanate, comparable to that of $PbNb_2O_6$. In the La-PT ceramics, d_hg_h was always smaller than 1500,

f) The high remnant polarization P_r evaluated to 32 μC cm^{-2} in the titanate and the relatively high coercive field E_c found in the La-PT series, suggest that the microstructure (grain size ~1μm) may have a clamping effect on the polarization reversal process. The higher grain size present in the Ca-PT microstructure contributes to both a larger total domain alignment and to a 90º domain rotation,

g) Both tetragonality and grain size are responsible for the appearance of macro- and micro-crackings in the modified lead titanate ceramics and, therefore, for its mechanical behavior. In that sense, the fracture toughness, K~c, increases with increasing tetragonality as a consequence of more compressively stressed microstructure. The hardness decreases with increasing tetragonality, probably as a consequence of a higher microcracking present in the ceramic materials. In both cases a higher grain size produced a decrease in these two mechanical parameters [73].

4.5.1.2. PZT ($PbTiO_3$-$PbZrO_3$ solid solution)

Lead zirconate titanate (PZT) ceramics are widely used as piezoelectrics in different applications. The ceramic materials possess several advantages over single crystals : they are easy to produce and can be machined in different shapes, with tailored properties thanks to chemical modifications introduced by dopants. The highest piezoelectric coupling coefficients have been found near the morphotropic phase boundary (MPB) where coexistence of the Ti-rich tetragonal and Zr-rich rhombohedral phases appears (figures 14a and 14b). The morphotropic phase boundary (MPB) region has been believed to be a sharp transition, but in practice it has a finite range of compositions over which the tetragonal and rhombohedral phases coexist. The width of the MPB has been investigated by many authors and found to be related to the heterogeneous distribution of Zr^{4+} and Ti^{4+} cations on the B site [77-80]. Perfect chemical homogeneity is often assumed in these systems, but local segregation of Ti and Zr could result in changes in symmetry and have dramatic influence on the overall properties. Atom-probe-tomography was shown to be an excellent technique for establishing the correct composition in the MPB region [81]. The compositional fluctuations were smaller for coprecipitated or sol-gel ceramics [82]. Even, the monophasic perovskite ceramics of the MPB composition, or near the MPB region, become two-phase materials within a lapse of time after poling. Strict conditions with regard to the nature environment have led to developing a series of new piezoelectric ceramic materials known as lead-free piezoelectric ceramics [83-87].

4.5.2 PTC (positive-temperature-coefficient) thermistors

Barium titanate $BaTiO_3$-based ceramics are largely used in the electronics industry. At present, their most important application is as dielectric layers in multilayer ceramic capacitors (MLCC) (figure 15a). The research on the miniaturization of electric and electronic

parts has been widely carried out, together with materials processing. The miniaturization of multilayer ceramic chip capacitors among passive components is remarkable, as the MLCC manufacturers have focused on the development of products with smaller size and higher capacitance. The manufacturing of thinner dielectric films is absolutely necessary for higher capacitance. At present, dielectric sheets of MLCCs have been elaborated by dip coating and slip coating ; their thickness has been decreased to about 1 µm (figure 15b). The thicknesses of the dielectric layers in MLCC are expected to become less than 0.3 – 0.5 µm within the next 10 years. Consequently, the particle size of the $BaTiO_3$ raw materials will decrease to a few ten units of nm. Thus, composition and processing must be carefully controlled to provide the highest permittivity values possible, a homogeneous fine-grained microstructure and to allow the reduction of the sintering temperature [88-90]. A review was recently published by Chen and Yang [91].

The electrical resistivity of n-type semiconducting barium titanate increases by several orders of magnitude near the ferroelectric Curie temperature (120 ºC). At the Curie temperature, $BaTiO_3$ undergoes a ferroelectric-to-paraelectric transition. Polycrystalline n-type semiconducting barium titanate ($BaTiO_3$) exhibits a behavior known as the positive temperature coefficient of resistivity (PTCR) effect, although it has been also reported that single crystals exhibit a negative coefficient (NTCR), as shown in figure 16.a [92-97]. The resistance increase is predominantly associated with an increase in the grain-boundary barrier height, therefore it is important to gain information about the grain boundary character in these devices. Figures 16.b and 16.c present some additional features of such devices, respectively the multilayer structure and a flow sheet of its processing.

Donor dopant incorporation is achieved by either electronic compensation at low concentration of dopants, or by vacancy compensation at high concentration. The electronic compensation explains the high conductivity of materials when donors are at low concentrations, whereas at high concentrations, grain boundaries inhibit the grain growth. As the dopant concentration increases, the local donor concentration at the grain boundary increases rapidly due to segregation, changing from electronic to vacancy compensation and resulting in the formation of highly resistive layers.

4.5.3 Pyroelectric and electrothermal characteristics.

The electrothermal (electrocaloric and pyroelectric) properties stem from the coupling between the electrical and thermal properties of a polar dielectric solid. The electrocaloric effect is an adiabatic change in temperature (ΔT) in response to an applied electric field, whereas the pyroelectric effect is the change in the charge density (polarization) in response to a change in temperature T. Both electrocaloric and pyroelectric effects are described by the same coefficient, $p = (\partial S/\partial E)T = (\partial P/\partial T)E$, where S is the entropy, T is the temperature, E is the electric field and P is the electric polarization. The property coefficient p is non-zero only for crystals belonging to one of the ten polar point groups, in which there exists a unique polar axis. Ferroelectric crystals represent a sub-group where the spontaneous polarization may be reoriented among symmetry-equivalent directions under the application of an electric field.

The electrothermal properties of ferroelectric materials have recently attracted considerable interest for their use in a variety of applications such as solid-state cooling systems and infra-red (IR) devices (Table 3). Such devices may find applications, for example, in thin film micro-coolers used as thermal management systems for next-generation integrated circuits (IC) or other high-power density microelectronic components. Applications in infra-red devices include intruder alarms, fire detection, environmental monitoring, gas analysis, radiometers, laser detectors and 2D arrays for uncooled thermal imaging. Ferroelectric materials are important for these applications due to their ability to be used at ambient temperatures (thereby eliminating the need for expensive cooling systems), their relatively low cost, low power consumption and wide operating range of temperature compared to photoconductive detectors. Furthermore, they are eco-friendly compared with conventional domestic and industrial refrigeration which produces greenhouse gases heavily. The temperature change resulting from the electrocaloric effect is analogous to the adiabatic demagnetization, which has long been used to cool cryogenic systems to temperatures approaching absolute zero. Like magnetocaloric materials, solid-state coolers based on electrocaloric materials may provide efficiency, size, weight and device integration benefits relative to conventional vapor compression systems. Electrocaloric materials based on ferroelectrics are known to have high electrothermal conversion factors (~0.95) and a maximum in response that can be varied over a wide temperature range (~100K to 800K) according to the temperature of the ferroelectric Curie point. The easiness of applying electric fields, as opposed to magnetic, makes electrocaloric coolers especially attractive for cooling device applications.

There are essentially two modes of operation for pyroelectric IR sensors. One mode operates at a temperature below (but typically near) the Curie temperature T_C of the ferroelectric where the variation in the spontaneous polarization as a function of temperature is large. In the dielectric bolometer mode, one works slightly above T_C in the paraelectric state of the ferroelectric and with an applied bias field to induce polarization [98-102]. In either case, it is required that the ferroelectric is deposited in a thin film form on a substrate compatible with the integrated circuits technology.

4.5.4 Optical devices.

Ferroelectrics will also play a major role in the next generation of optical devices. They have the potential to be the backbone of wireless laser communication systems or ground-based fiber optics, capable of carrying large amounts of information at ultrafast speeds. Even though their industrial and technological uses are very promising, ferroelectric materials will also continue to provide consumers with accessories and gadgets that will pleasure and simplify the everyday life. With the recent push on miniaturization of practical devices and the advancement of nanotechnology, ferroelectric materials may be fabricated to exhibit transducer effects at a scale small enough to be useful at the nanometer resolution.

Lead lanthanum zirconate titanate (PLZT) perovskite ceramics of chemical formula $Pb_{1-x}La_x(Zr_yTi_{1-y})_{1-0.25x}V^B_{0.25x}O_3$ (where V are oxygen vacancies), are typically known as PLZT(100x/100y/100(1-y)). Compositional changes within this quaternary ferroelectric system, especially along the morphotropic phase boundaries (figure 17), can significantly alter the material's properties and behavior under applied electric fields or temperature variations. This allows such a system to be tailored to a variety of transducer applications. For instance, PLZT ceramics have been suggested for use in optical devices because of their good transparency from the visible to the near-infrared and because of their high refractive index ($n \approx 2.5$), which is advantageous in optical waveguide applications [103-105]. PLZT compositions near the tetragonal and rhombohedral ferroelectric phases and cubic antiferroelectric phases, typically with compositions (a/65/35), with $7<a<12$, are known as relaxor ferroelectrics, since they exhibit a frequency-dependent diffuse ferroelectric-paraelectric phase transition in their complex dielectric permittivity [106]. Relaxor ferroelectrics are particularly attractive in transducer applications because they can be electrically or thermally induced into a ferroelectric phase possessing a large dipole moment accompanied by a large mechanical strain, and revert back to a non-ferroelectric state upon

the removal of the field or temperature. They also exhibit a slim hysteretic behavior in the transition region upon the application of an electric field, making them ideal for precise control actuator applications [107,108].

Modification of the lead zirconate titanate (PZT) system by the addition of lanthanum sesquioxide (PLZT) has a beneficial effect on several other basic properties of the material, such as increased squareness of the hysteresis loop, decreased coercive field, increased dielectric constant, maximum coupling coefficients, increased mechanical compliance and enhanced optical transparency. Many possibilities of uses of the PLZT system have been reported, such as thin films for capacitors in ultra-high density dynamic random access memories (DRAMs) [109], new types of actuators as wireless remote control photo-actuators, high-speed optical shutters, modulators, photo-acoustic devices for the optical communication systems, etc. (figure 18.a). The PLZT ceramic materials are presently used in our daily life as electronics, optics, medicine, communication and new possibilities still waiting for discovery (figure 18.b). Recently, other systems have proved to be suitable for fabricating transparent ferroelectric ceramics, such as $Pb(Mg_{1/3}Nb_{2/3})O_3$–$PbTiO_3$ when doping with small amounts of La [110] (figure 18.c).

For the same reasons of safety that led to the search of Pb-free piezoelectric and relaxor compounds, Pb-free transparent ferroelectric ceramics have been developed. For example, $K_{0.5}Na_{0.5}NbO_3$, with good piezoelectric behavior, can be prepared as transparent ceramics by pressureless sintering. For these ceramics, the optical transmittance reaches a high value of 60%–70% in the near-infrared region. The ceramics also exhibit a good linear EO response, giving an effective EO coefficient of 30–40 pm/V, which are comparable to those found in the PLZT ceramics [111-113].

4.5.5 Pb-based and Pb-free ceramic relaxors [114]

Lead-based relaxor ferroelectrics are compounds with the general formula $PbBO_3$ in which the *B*-site is disordered. They exhibit exceptionally large piezoelectric coefficients d_{33} = 2500 pC/N and dielectric constants above 25 000, making them attractive for device applications. $PbMg_{1/3}Nb_{2/3}O_3$ (PMN) and $PbZn_{1/3}Nb_{2/3}O_3$ (PZN) are prototypical relaxor ferroelectrics and the most studied ones ; both display a broad and unusually frequency-dependent zero-field dielectric response (figure 19) that contrasts with the sharp and comparatively frequency-independent peaks observed in conventional ferroelectrics such

as $PbTiO_3$ (PTO) and $BaTiO_3$ (BTO). This anomalous dielectric behavior is matched by the odd structural properties of the lead-based relaxors, as represented by PMN and PZN. Instead of a well-defined structural transition to a long-range ordered ferroelectric ground state, which normally characterizes a typical ferroelectric, lead-based relaxors develop short-range ferroelectric correlations on cooling that are consistent with tiny domains of ferroelectric order embedded within a paraelectric matrix, while the average structural unit cell remains cubic. On doping with $PbTiO_3$, these domains coexist with a long-range ferroelectric structural distortion. These local regions of ferroelectric order, known as Polar nanoregions or PNRs, were first postulated to explain the temperature dependence of the optical index of refraction of a variety of disordered ferroelectric materials. The existence of PNRs has since been confirmed by numerous X-ray and neutron-scattering studies, which report the presence of strong diffuse scattering at low temperatures. The diffuse scattering in PMN, for example, was recently investigated in great detail and shown to vanish above ~420 K [115-123].

Lead iron niobate $Pb(Fe_{1/2}Nb_{1/2})O_3$ (PFN), a single-phase multiferroic, is a site and charge disordered relaxor ferroelectric. It undergoes a paraelectric to ferroelectric phase transition at a Curie temperature $T_C \approx 385$ K, below which the tetragonal phase (P4mm) is stable down to 355K. The room-temperature crystal structure has been proposed to be either monoclinic (Cm) or rhombohedral (R3m). There is a paramagnetic to antiferromagnetic (AF) transition at a Néel temperature $T_N \approx 145$ K. Other parent compounds of PFN are $Pb(Sc_{1/2}Nb_{1/2})O_3$ or $Pb(In_{1/2}Nb_{1/2})O_3$.

Unlike the $Pb(B_{1/3}B'_{2/3})O_3$ relaxor, the $Pb(B_{1/2}B'_{1/2})O_3$ compound does not undergo a typical diffuse phase transition without lead vacancies on A-site which enhances random fields (figure 20).

Relaxors based on $Pb(Zn_{1/3}Nb_{2/3})O_3$-$PbTiO_3$ (PZN-PT) and $Pb(Mg_{1/3}Nb_{2/3})O_3$-$PbTiO_3$ (PMN-PT) exhibit much better electromechanical properties compared to the conventional PZT ceramics which have been dominating piezoelectric applications for more than 40 years. The theoretical studies for the physical mechanism of this multi-domain system have generated a great deal of interest in the scientific community. From both fundamental study and device design purposes, it is necessary to get the complete set of matrix properties for those crystals. A complete set of elastic, piezoelectric and dielectric constants has been recently reported for $0.95Pb(Zn_{1/3}Nb_{2/3})O_3$-$0.045PbTiO_3$ (PZN-4.5%PT) and $0.92Pb(Zn_{1/3}Nb_{2/3})O_3$-$0.08PbTiO_3$ (PZN-8.0%PT) single crystals. It is known that the PZN-4.5%PT single crystal system is

fairly far away from the morphotropic phase boundary (MPB) composition, therefore it does not represent the maximum electromechanical capability of this solid solution. It has been shown that the PZN-8.0%PT single crystal possesses much larger piezoelectric strain constant d_{33} than that of PZN-4.5%PT. The electromechanical coupling coefficient k_{33} of PZN-8.0%PT could reach 0.94, which is higher than that of PZN-4.5%PT [124].

The strain induced by the electrostrictive effect is generally small when compared with that induced by piezoelectricity, so a limited attention has been focused on it [124]. In the 1980's, a systematic study on electrostriction was carried out on relaxor ferroelectrics with perovskite structure, such as $Pb(Mg_{1/3}Nb_{2/3})O_3$, $Pb(Zn_{1/3}Nb_{2/3})O_3$ and $0.9Pb(Mg_{1/3}Nb_{2/3})O_3$-$0.1PbTiO_3$ (PMN-0.1PT) single crystals/ceramics, in which a high electrostrictive strain was observed because of the high dielectric response of the relaxors [125-127]. Relaxors offer several advantages over ferroelectric materials, including low hysteresis in the strain-field response (excellent displacement accuracy), no remnant strain, reduced aging effects and they do not require poling [128-132]. Compared with classical ferroelectric ceramics, these materials are believed to have potentials for their use in actuator applications such as inchworms, micro-angle adjusting devices and bi-stable optical devices, where reproducible and non-hysteretic deformation responses are required.

However, the presence of lead oxides poses serious environmental and health concerns, especially during manufacturing and disposal after usage ; therefore, the research community is actively engaged in developing Pb-free alternatives [128,129]. In particular, $(Bi_{1/2}Na_{1/2})TiO_3$ (BNT)-based relaxors have attracted a lot of attention during the last decade. Upon application of an electric field, these systems exhibit large electromechanical strains as they undergo a field-induced phase transformation to a polar ferroelectric phase with metastable domains. This transformation is irreversible in non-ergodic compositions and reversible in ergodic compositions. A temperature-dependent transition from an ergodic to a non-ergodic state is also observed around 100-200 ºC [130-132] ; above the transition temperature, the polarization loops are pinched and electromechanical strain data show no negative values, characteristic of a reversible field-induced phase transformation in ergodic relaxors.

4.5.6 Ultra-low loss in ordered perovskites

Mobile phone networks allow communication from cell to cell via antennas located on masts and associated base stations. Within a cellular network, the average base station coverage is a diameter of 35 and 18 km at 900 and 1800 MHz, respectively. Each base station houses microwave (MW) resonators that are used to carry signals of a specific frequency and filter spurious signals and sidebands that interfere with the quality of the transmitted/received frequency band [133].

Ceramic resonators are simple in concept, but controlling their dimensions and precise phase assemblage during processing is difficult. Any slight differences from batch to batch or within a batch may alter their resonant frequency and temperature stability. Ceramic resonators of differing geometries, with single mode pucks and multimode functions are manufactured, often with unusual geometries to induce several resonant MW modes within their body at any one time. In service, the ceramic conventionally rests within a silver-coated square cavity. Typically, many hundreds of these cavities will reside in the base stations of a cellular network [134].

With the current worldwide explosion in the development of microwave-based communications technologies, the production of dielectric resonators has emerged as one of the most rapid growth areas in electronic ceramic manufacturing. Nowadays, with the development of wireless communication, especially the third-generation telecommunication (3G), the complex perovskite ceramics such as $Ba(B'_{1/3}B''_{2/3})O_3$ ($B' = Zn^{2+}$, Mg^{2+}, Co^{2+}, Ni^{2+}; $B'' = Ta$, Nb), with excellent microwave dielectric properties, have attracted much scientific and commercial attention.

An explosive increase of microwave communications occurred in the 1950-60s. As a consequence, several oxides were developed to fulfill the electronic requirements for a commercial microwave resonator system, being at the same time cheap and reproducible. These materials should combine high relative permittivities ($\varepsilon_r > 25$), low dielectric losses and high Q ($Q = 1/\tan\delta > 5000$), together with a near zero-temperature coefficient of resonant frequency ($\tau_f = 40 \pm 10$ ppm), for use in variable climates. Microwave resonator ceramics in the BaO–TiO_2 system ($Ba_2Ti_9O_{20}$, $BaTi_4O_9$), in zirconia-modified systems ZrO_2–SnO_2–TiO_2 ($Zr_{1-x}Sn_xTiO_4$) and in the BaO-PbO-RE_2O_3–TiO_2 systems, have found widespread commercial applications as filters and oscillators in wireless communication technologies. These ceramics proved to be adequate for current applications, but needs for further miniaturization and improved filtering capabilities led to the development of new oxides with

even higher dielectric constants and lower losses. An understanding of the critical chemical and structural requirements for a successful ceramic resonator was progressively attained. Also in this field, some perovskite-type compounds have proved to be a suitable solution to attain more complex requirements. This progress has been carried out by studying the complex crystal chemistry of many of the existing oxide dielectric perovskites, whose structures are strongly ordered on the B-sites [135,136].

In the early 1980s, a series of complex perovskites, in which the B-sites are occupied by a mixture of M^{2+} and M'^{5+} cations, showed dielectric properties suitable for use in resonators. The most interesting perovskites were based in the formula $Ba(M^{2+}_{1/3}Ta^{5+}_{2/3})O_3$, where M = Zn, Mg. For the Zn-compound, a permittivity value $\varepsilon_r \approx 30$ was measured and for the Mg-compound, $\varepsilon_r \approx 25$. Both attained Q values higher than 10 000 at 10 GHz. Previously studied complex perovskites, with large A cations, such as Ba and Sr, and a 1:2 mixture of divalent and pentavalent cations in B-sites, showed that these cations can be ordered in the <111> crystalline planes. This long-range ordering leads to a subsequent displacement of oxygen anions between the cation planes. The crystalline structure is then trigonal, with a sequence $\{...M^{2+}\text{-}M^{5+}\text{-}M^{5+}\ldots\}$ along the {111} direction of the parent cubic disordered perovskite, coincident with the c-direction of a superlattice (figure 21).

The perovskite systems based on Ta_2O_5 and divalent cations M^{2+}, in which a certain B-site cation-ordering degree exists, revealed that this ordering is fundamental for lowering the dielectric losses in the microwave region. Inducing a long-range cation order by means of high-temperature annealing, allowed to increase the Q factor from 500 to < 35 000, for a microwave window of 10 GHz. This effect could be increased by controlling the volatilization of Zn in the case of $Ba(Zn_{1/3}Ta_{2/3})O_3$, but it has been well established that the long-range cation ordering is the main parameter for controlling the dielectric features of these perovskite-type compounds, particularly the dielectric losses [138-140].

The dielectric loss tangent at microwave frequencies for the complex perovskite $Ba(Zn_{1/3}Ta_{2/3})O_3$ was calculated with respect to the degree of structural disorder on B-sites. Starting out from the equations of ion motion, the dielectric loss is expressed in terms of the pair-correlation functions corresponding to the ordering of Zn and Ta ions on B-sites. The characteristic length included in the pair-correlation functions corresponds to the average size of the region containing disorder in the ion arrangements at the B-sites ; thus the relation between the structural disorder on the B-site and the dielectric loss tangent at microwave

frequencies was clarified theoretically. The numerical results show that the microwave loss tangent values change their power from –3 to –6 with increasing degree of order on the B-site, which agrees well with the experimental observations. Results confirm the physical origin of the microwave loss of complex perovskite $Ba(Zn_{1/3}Ta_{2/3})O_3$ [141,142].

$Ba(B'_{1/2}B''_{1/2})O_3$-type microwave dielectric ceramics are also promising material components in resonators and filters because of their suitable permittivity (ε), near-zero temperature coefficients at resonant frequencies (τ_f) and high quality factors (Q×f). In recent years, numerous investigations of materials with excellent microwave dielectric properties were focused on the complex perovskite ceramics $Ba(Mg_{1/2}W_{1/2})O_3$ (BMW), which is one of the better microwave ceramics in this group with ε = 17, $\tau_f = -33.6\times10^{-6}$ °C^{-1}, and Q×f = 42 000 GHz [137,143].

4.6. Metallic conduction and superconductors

4.6.1 Metallic conductors

$LaNiO_3$ is a conductive oxide with a perovskite-type structure, which can be used as an electrode for fatigue-free ferroelectric random access memories, in solid oxide fuel cells, as an absorber of oxygen or in oxidation catalyst. However, $LaNiO_3$ is the only one in the $LnNiO_3$ series (Ln: lanthanides) exhibiting a metallic character down to 4.2 K. Other $LnNiO_3$ have a metal–insulator transition temperature (T_{MI}) which increases as the size of the rare-earth decreases. For example, $SmNiO_3$, with a smaller rare-earth ionic radius, presents a T_{MI} of 400 K and is insulator at room temperature. The metal-insulator phase diagram for $LnNiO_3$ as a function of the tolerance factor or the ionic radius of the rare-earth, was determined. For small rare-earths, the structure has a smaller electronic transfer parameter, presents bent Ni-O-Ni bonds and a lower bandwidth ; they are insulators at $T < T_{MI}$ with a charge-transfer gap between the occupied O^{2p} valence band and the unoccupied Ni^{3d} conduction band due to electron localization [144] (figure 22).

4.6.2 Superconductors, YBaCuO

The cubic perovskite $BaBi_{1-x}Pb_xO_3$ is distorted depending upon composition. The tetragonal x = 0.75 compound is a superconductor ; x< 0.65 results in an orthorhombic semiconductor ; $BaBiO_3$ is monoclinic. The valence of Bi has been a matter of dispute [145]. This perovskite

was the first oxide compound showing a superconducting transition at a relatively high temperature.

The compound $YBa_2Cu_3O_{7-\delta}$, also of perovskite structure, was the first superconductor attaining a transition temperature above liquid nitrogen temperatures [146]. It has a perovskite-type structure with a high oxygen deficiency in their cell lattice (figure 23). The superconducting behavior of this compound is much influenced by the degree of oxygen deficiency : only those materials with $0 \leq \delta \leq 0.65$ are superconducting. For $\delta \sim 0.07$, the material is a superconductor at the highest transition temperature T_C of 95 K, with very high critical magnetic fields : 120T for **B** perpendicular and 250 T for **B** parallel to the CuO_2 planes. For values above 0.65, the compound is insulating. The δ-value also has a strong influence on the crystalline structure : for values near 0, $YBa_2Cu_3O_7$ crystallizes with orthorhombic symmetry while increasing δ leads to a tetragonal-like structure.

The understanding of the superconducting properties in oxides has greatly improved over the last years and new ways to change their properties are constantly being found. Old problems are being overcome and, with such a large amount of experimental and theoretical work, it can be expected that in the near future it would be possible to fabricate samples with optimal compositional and microstructural properties [147-149]. An excellent review on different types of superconducting oxides can be found in ref. [150].

4.7. Multiferroics

The term multiferroic is applied to materials presenting simultaneously two or three ferroic behaviors : ferroelectricity, ferromagnetism and ferroelasticity, i.e., the electrical charges can be controlled by an applied magnetic field, and magnetic order can be controlled by applied voltages. A major issue that makes difficult the study of such materials is the scarce number of phases presenting these properties at the same time.

Magnetic and ferroelectric materials are found in many fields of modern science and technology. For example, ferromagnetic materials with switchable spontaneous magnetization driven by an external magnetic field are widely used in data-storage. The discovery of the giant magnetoresistance effect (to be discussed later on) significantly promoted magnetic-memory technology in connection with areas of magnetoelectronics and spintronics. The fundamental and applicative issues associated with magnetic random-access memories (MRAMs) and related devices, have been deeply studied in order to achieve high-density

integration and also to improve the relatively high writing energy. A good review on the multiferroics is given by Wang et al. [151].

Ferroelectricity appears in perovskite structures where the B-site is occupied by transition metals with empty d-shells. On the contrary, partially filled d-shells are required for magnetism to occur. These are mutually exclusive phenomena and, therefore, it is difficult to attain a multiferroic state in such oxides. Even more scarce are the phases where simultaneous properties appear at room temperature [152,153].

Among the few materials presenting this possibility there is the bismuth ferrite $BiFeO_3$, where the polarization is mostly caused by the lone pair (s^2 orbital) of Bi^{3+}, so that the polarization comes mostly from the A-site, while the magnetization comes from the B-site (Fe^{3+}), with a Néel temperature corresponding to its antiferromagnetic order at 370 °C and a ferroelectric Curie temperature at 820-830 °C. Theoretical values of spontaneous polarization have been proposed to be close to 90pC/cm^2, while the experimental values are as high as 40pC/cm^2 in polycrystalline ceramics. The antiferromagnetic character is due to a spatially modulated spin structure which does not allow net magnetization and inhibits the observation of a notable linear magnetoelectric coupling between polarization (P) and magnetization (M). With the purpose to induce a net magnetic signal in $BiFeO_3$, substitution of Bi in the A position by an alkaline-earth element such as Sr has been successfully tested, and a weak ferromagnetism has been obtained. Important magnetoelectric effects, as the increase of the spontaneous polarization at increasing applied magnetic fields, have been observed in Sr-doped $BiFeO_3$ ceramics. In addition, doping with Sr helps to stabilize the perovskite phase, inhibiting the formation of other phases (e.g., $Bi_2Fe_4O_9$), this being one of the major issues in the development of these materials [154,155].

Also regarded as a true multiferroic material is the bismuth manganite $BiMnO_3$, with both ferromagnetic and ferroelectric properties. $BiMnO_3$ possesses a distorted perovskite structure with monoclinic symmetry due to highly polarizable bismuth ions and Jahn-Teller (JT) active manganese ions. Its magnetic moment certainly arises from the $3d^4$ electrons of the Mn^{3+} ion, while the ferroelectric polarization comes from the Bi $6s^2$ lone pair. The saturation magnetization for a $BiMnO_3$ polycrystalline sample was reported to be 3.6 μ_B by Mn^{3+}, with a ferromagnetic transition temperature at 105 K. No noticeable structural change associated with the ferromagnetic transition was observed. The ferroelectric remanent polarization at 200-K for a polycrystalline sample is about 0.043μC/cm^2 ; however, there is no consensus on

the ferroelectric transition temperature T_{FE}. Some authors reported T_{FE}≈450 K as the reversible structural transition temperature without symmetry change, but others suggested $T_{FE} \approx$ 750–770 K, at which a centrosymmetric-noncentrosymmetric structural transition occurs.

The detailed structure of $BiMnO_3$ at room temperature was investigated by neutron powder diffraction. A compatible orbital order was proposed although some unresolved issues still remain, such as the temperature dependence of the degree of ordering at high temperatures and the determination of the transition temperature itself, T_0. A better knowledge of the relationship between ferroelectricity and orbital order in this multiferroic compound is clearly an issue of interest [9,156]. Potential applications for this material mainly concern some alternative ways to encode and store data using both electric polarization and magnetization. Magnetoelectric coupling between these properties involve huge potential applications in the sensor industry, spintronics and others.

4.8. Magnetic properties of some perovskites

The compound $LaMnO_3$ is an insulator of perovskite structure, composed of ferromagnetic planes of Mn^{3+} spins oriented in the basal plane, antiferromagnetically coupled along the *c*-axis. Substitution of the trivalent rare-earth cation by a divalent ion oxidizes the MnO_6 array, creating Mn^{4+} ions. This fact makes that the solid solutions develop interesting semiconducting features. At the same time, the antiferromagnetic phase is progressively destroyed with varying content of dopant and transforms first, into a canted structure before becoming fully ferromagnetic. The electrical and magnetic properties of these mixed valence perovskites are closely related to the ratio Mn^{3+}/Mn^{4+}, which depends on the degree of substitution of the trivalent rare-earth element by divalent cations and therefore, on the overall stoichiometry of both the cationic sites and the oxygen amount. As a consequence of the ferromagnetic response, an interaction between electrical conduction and magnetic order occurs. The discovery of giant and colossal magneto-resistance phenomena in doped perovskite manganites of formula $RE_{1-x}M_xMnO_3$ (RE = rare-earth element, M = divalent cation) (figure 24) was followed by an enormous work during the past years [157-159]. Of particular interest was the observation of a very strong magneto-resistance behaviour, named colossal magneto-resistance CMR [160,161] in some solid solutions $La^{3+}_{1-x}Me^{2+}_xMnO_3$, or the experimental observation of large CMR effects in $Nd_{0.5}Pb_{0.5}MnO_3$ by Kusters et al. [162] and in $La_{2/3}Ba_{1/3}MnO_3$ by von Helmolt et al. [163]. In a pioneer work, Searle and Wang were

the first to report CMR features in $La_{1-x}Pb_xMnO_3$ manganites prepared as single crystals [164].

The nature and size of the modifying cation play an important role in the electrical behavior of the doped manganites, giving place to different conduction mechanisms : large-bandwidth manganites $\{La_{1-x}Sr(Ba)_xMnO_3\}$, intermediate-bandwidth manganites, $\{La_{1-x}Ca_xMnO_3\}$ and low-bandwidth manganites $\{Pr_{1-x}Ca_xMnO_3\}$ [165-167]. Besides, the magneto-resistance coefficient also varies, increasing when the ionic size of the divalent cation decreases, in a sequence Ba, Pb, Sr, Ca [168,169].

The magnetic behaviour of these solid solutions, with general formula $\{La_{1-x}Me^{2+}{}_xMnO_3\}$, is explained by double-exchange mechanisms between the Mn^{3+} and Mn^{4+} ions situated in the B sublattice, that is, in the unique magnetic sublattice of the crystalline structure. Indeed, in this type of solid solutions, the RE cation is usually a diamagnetic (La^{3+}) or a weakly paramagnetic (Pr^{3+}, Nd^{3+}, Sm^{3+}) cation. Therefore, interactions between sublattices A and B or in the A sublattice are expected to be null or very weak. In other groups of $REMnO_3$ perovskites compounds, the presence of a Mn^{4+} cation can be achieved by substituting part of the Mn^{3+} cations in the B sublattice by divalent cations of adequate size. These cations, Ni^{2+}, Cu^{2+} or Co^{2+}, are paramagnetic. Cobalt can adopt the +2 and the +3 valence states under special conditions of synthesis [170-173]. A large amount of work concerning this type of substitutions has been achieved on rare-earth manganites with both primitive orthorhombic perovskite and Mn-hexagonal-type derived structures, in which the cations situated in the A sublattice have large or very large magnetic moments, e.g., Gd, Dy or Er.

The complexity of forming magnetic sublattices when Mn is partially substituted by other paramagnetic ions, combined with the presence of strong paramagnetic rare-earth cations in the A sublattice, are at the origin of a series of features appearing in several of these solid solutions ; some of them, discussed hereafter, can be described as :

Spin reversal as a function of temperature (thermal spin reversal), fig. 25,
Crossing branches in the hysteresis loops at low applied fields, fig. 26,
Abrupt jumps in step-like magnetic hysteresis cycles, figs. 26 and 27,
Exchange bias displacement, fig. 28.

Thermal spin reversal appears in manganite perovskites in which the large A cation is a paramagnetic ion, such as Pr^{3+}, Ce^{3+}, Gd^{3+}, independently of the magnitude of the magnetic

moment of the A cation. Spin reversal behavior at high temperatures has been also observed in ferro-chromites of perovskite structure, such as $\{La_{1-x/2}Bi_{x/2}\}\{Fe_{0.5}Cr_{0.5}\}O_3$, in which the A cation is diamagnetic and the magnetic ions, Fe and Cr, occupy only one and the same sublattice ; in this case, an unusual zero-magnetization phenomenon was observed at a compensation temperature T_{comp} under relatively high external magnetic fields (~ 0.1-0.3 Tesla). It is remarkable that this zero-magnetization phenomenon does not originate from a ferrimagnetic ordering of the Fe^{3+} and Cr^{3+} cations, but is due to the canting of pure '$La_{1-x}Bi_xFeO_3$' and '$La_{1-x}Bi_xCrO_3$' domains or clusters, antiferromagnetically coupled [174].

4.8.1 Crossing branches in the hysteresis loops

The phenomenon of a spin reversal in perovskites (as shown in figure 25), in which the Mn cation is substituted by divalent cations and with an A-cation possessing a strong paramagnetic moment, can be reasonably predicted due to the existence of double-exchange interactions in the B-sublattice between Mn^{3+} and Mn^{4+} cations and an antiferromagnetic mechanism between the A and the B sublattices. Other phenomena are, however, less predictable. Perovskites of composition $ErCo_xMn_{1-x}O_3$ showed magnetic loops in which the two branches, corresponding to the decreasing and increasing magnetic fields, intersect at low magnetic applied fields (figure 26) [175-177]. From these results, it is quite evident that two contributions are superposed : a ferromagnetic component, characterized by an irreversible behavior and rather low coercive fields, and an antiferromagnetic component, characterized by an almost linear variation of M versus H at low fields. The partial substitution of manganese by cobalt, in a disordered fashion, has an incidence on the ferromagnetic component, lowering the coercive field. The coercive fields H_{coerc} are extremely low and tend to be zero at x(Co) = 0.30 and for x(Co) $\geq$ 0.60, in spite of the strong ferromagnetic interactions deduced from the ZFC/FC (zero-field-cooling/field-cooling) cycles and the compositional dependence of T_C. The antiferromagnetic interaction between A and B sublattices seems to be enhanced at a composition $ErCo_{0.50}Mn_{0.50}O_3$, for which the spin-reversal effects are observed (figure 25). The crossing of the magnetic branches (fig. 26, main panel) is only observed at temperatures below that of the spin reversal (fig. 26, insert). This fact points to the existence of two exchange coupling mechanisms. In addition to this, the magnetization loop performed on the $ErCo_{0.50}Mn_{0.5}O_3$ sample at $T < T_{comp}$ shows a second anomaly at high fields, which corresponds to a sudden increase of the magnetization when the applied magnetic field increases. Both anomalies are also seen, although less pronounced, in

some other compositions, all of them situated close to the 50/50 = Mn/Co substitution rate. These anomalies are not found in the near parent $ErNi_xMn_{1-x}O_3$ system.

4.8.2 Step-shaped magnetic hysteresis cycles

The step changes observed at high fields in some samples deserve much attention, and current works aim toward a better characterization [176-179]. This is a dynamical phenomenon which depends on the sweep rate of the applying magnetic field. Such time dependence has been noticed in several magnetic systems, and it has been thoroughly described in the works of Hardy et al. concerning $(Pr,Ca)MnO_3$ [178], Tang et al. in $Pr_{0.6}Na_{0.4}MnO_3$ [179] and others. In some cases, slow changes of the magnetic field lead to a smooth variation of the magnetization curve at high fields, while sudden changes of the applied field (typically, 0.2 T/min) provoke a sudden jump of the magnetization. Higher fields and a better control of the magnetic-field sweep rate will give a much better understanding of this phenomenon. The step-like loops are basically associated to the presence of both Mn and Co cations when the B-site substitution is carried out. Dy- and Eu-based solid solutions, $RECo_{0.5}Mn_{0.5}O_3$, which do not show spin reversal, present loops with more than one step (figure 27, left panels) [177]. For the same compositions, with Ni instead of Co, no step-like magnetization cycles have been seen (figure 27, right panels). In the case of Eu, up to five steps have been observed at 2.5 K. Eu is a Van Vleck ion and this fact could explain the unusual multiple-step behavior. The multiple valence state of cobalt is probably the reason for which solid solutions containing Co show a more complex behavior than those containing a more stable valence state, such as Ni in B-sites or Ca in A-sites. In the case of Co cations, the possible cationic configuration $RE^{3+}\{Co^{2+}_{1-x}Mn^{4+}_{1-x}Co^{3+}_{2x-1}\}O_3$ leads to the existence of new magnetic exchange pairs, such as Co^{2+}-Co^{3+}.

4.8.3 Exchange bias displacement [180]

The discovery of exchange bias (EB) effect by Meiklejohn and Bean [180] has gathered enormous interest from the scientific community for its intriguing fundamental and technological aspects. Recent impetus on EB have opened numerous and various aspects of research, such as electronics and their usages in spin valves, magnetic recording read-heads, giant magnetoresistive sensors, etc. The EB is usually characterized by an asymmetric shift in the magnetic hysteresis loop along the field axis when a ferromagnetic (FM)-antiferromagnetic (AFM) layered or composite system is cooled in a static magnetic

field through the Néel temperature (T_N) of the AFM phase (figure 28). The magnitude of the loop shift (HEB) depends on various factors, such as the interfacial roughness, the characteristics of the involved FM and AFM layers, the complex spin structure at the interface, the uncompensated moments at the interface, etc. Rana et al [181] studied the heterostructure (AFM)$La_{0.3}Sr_{0.7}FeO_3$/(FM)$SrRuO_3$ and found that unusual low-field positive exchange bias, cooling-field-driven reversal of positive to negative exchange-bias and layer thicknesses, optimized the unusual vertical magnetization shift, all these being novel facets of exchange bias being explored for the first time in magnetic oxides. The successive magnetic training induced a transition from positive to negative exchange bias regime with changes in domain configurations. These observations were well corroborated by the hysteresis loop asymmetries which displayed modifications in the AFM spin correlations. These exotic features emphasized the key role of : i) mosaic disorder inducing subtle interplay of competing AFM-superexchange and FM double exchange at the exchange biased interface and, ii) training inducing irrecoverable alterations in the AFM spin structure.

Gibert et al [182] have studied the EB developed in $LaNiO_3$–$LaMnO_3$ (LNO-LMO) superlattices in which one of the components is paramagnetic, $LaNiO_3$, whereas the other, $LaMnO_3$, is weakly ferromagnetic. The observation of exchange bias in (111)-oriented LNO-LMO super-lattices, manifested as a shift of the magnetization field loop, not only implies the development of interface-induced magnetism in the paramagnetic LNO layers, but also provides a very subtle tool for probing the interfacial coupling between the LNO and LMO layers. First-principles calculations made by those authors [182] seemed to indicate that this interfacial interaction may give rise to an unusual spin order, resembling a spin-density wave, within the LNO layers. The observation of exchange bias phenomena at the interfaces between a paramagnet and a ferromagnet, highlights once more the potential of interface engineering for tailoring the properties of complex oxides and extending their functionalities towards new technological applications.

The above examples of EB were studied on heterostructures combining two different perovskite compounds. Some double perovskites have also shown EB behavior [183]. For instance, Sr_2FeCoO_6, which is a spin glass compound, develop antiphase boundaries between the ferromagnetic and antiferromagnetic regions in the disordered glassy phase ; it is assumed that these boundaries are responsible for the observed effect, which is reflected in the cooling field dependence and temperature evolution of the exchange bias field and training effect (figure 29).

5. Conclusions

Oxides with perovskite-type structure have shown a great potential in a wide range of applications. Their versatility with regard to the crystalline symmetry and their ability to incorporate many modifying cations, lead to a series of new properties ; the facility for tailoring composition, properties and shaping (bulk, thick and thin films, nanoparticles) allows to think that their future will be as important as their splendid past.

Some of the compounds and materials exposed in this review, such as PZT-based piezoelectric materials, $BaTiO_3$ as capacitor, bulk or multilayer, $PbTiO_3$-based pyroelectrics, PLZT as optoelectronic, etc., have accomplished their scientific way, and their future aims toward technological improvements to enhance their applications. However, in the case of Pb-based compounds, environmental requirements and health considerations are presently retarding their use in the future. Lead-free piezoelectric compounds have a more promising future for their use in advanced technologies.

Magnetic perovskites have a wide field of research and applications since new types of magnetic features appear, thus opening significant opportunities for devices in electronics and informatics. The strong advances in nanotechnologies, along with the developing of new multiferroics compounds and heterostructures, open some of the most promising horizons for researches in the field of materials science, heading towards the study of materials based on perovskite-type structures.

References

[1] Muller O., Roy R., "*The Major Ternary Structural Families"*, (1974), Springer Verlag (Berlin, Heidelberg, New York)

[2] Navrotsky A., Weidner D.J. (eds.), "*Perovskite: a structure of great interest to geophysics and materials science"*, (1989), American Geophysical Union, Geophysical Monograph Series, volume 45.

[3] Tejuca L.G., Fierro J.L.G. (eds.), "*Properties and applications of Perovskite-type Oxides"*, (1993), Marcel Dekker, Inc. (New York)

[4] Mitchell R.H., "*Perovskites, Modern and Ancient"*, (2002) Thunder Bay, Ontario (Almaz Press)

[5] Sanz-Ortiz M.N., Rodriguez F., Rodriguez J., Demazeau G., (2011), *J. Phys.: Condens. Matter* **23**, 415501

[6] Triana C.A., Corredor L.T. , Landinez-Téllez D.A., Roa-Rojas J. (2012) *Physica B,* **407,** 3150

[7] Corredor L.T., Landinez-Téllez D.A., Pimentel Jr. J.L., Pureur P., Roa-Rojas J., (2011), *J. Modern Phys.,* **2**, 154

[8] Priya S., Nahm S. (eds.), "*Lead-Free Piezoelectrics"*, (2012) ,(Springer Science + Business Media (New York, Dordrecht, Heidelberg, London)

[9] Belik A.A., Iikubo S., Yokosawa, T., Kodama K., Igawa N., Shamoto S., Azuma M., Takano M., Kimoto K., Matsui Y., Takayama-Muromachi E., (2007), *J. Am. Chem. Soc*., **129**, 971

[10] Thomas C.I., Suchomel M.R., Duong G.V., Fogg A.M., Claridge J.B., Rosseinsky M.J., (2014), *Philos. Trans. R. Soc.A.* **372**, 20130012

[11] Moure A., Hungría T., Castro A., Galy J., Peña O., Tartaj J., Moure C., (2010), *Chem. Mater.,* **22**, 2908

[12] Moure A., Hungría T., Castro A., Galy J., Peña O., Martinez I., Tartaj J., Moure C., (2012) *Ceram. Intern.,* **38,** 1507

[13] Moure A., Castro A., Tartaj J., Moure C., (2009) *Ceram. Intern.,* **35,** 2659

[14] Moure A, Tartaj J., Moure C, (2011) *J. Alloys Compds,* **509,** 7042

[15] Waintal A., Chenavas J., (1967) *Mat. Res. Bull.*, **2,** 819

[16] Zhou J.-S., Goodenough J.B., Gallardo-Amores J.M., Moran E., Alario-Franco M.A., Caudillo R., (2006) *Phys. Rev. B*, **74**, 014422

[17] Uusi-Esko K., Malm J., Imamura N., Yamauchi H., K arppinen M., (2008) *Mater. Chem. Phys.,* **112,** 1029

[18] Huang Y.H., Fjellvåg H., Karppinen M., Hauback B.C., Yamauchi H., Goodenough J.B., (2006) *Chem. Mater.,* **18,** 2130

[19] Duran P., Fernández-Lozano J.F., Capel F., Moure C., (1988), *J. Mater.Sci*. **23**, 4463

[20] Go Y.B., Jacobson A.J., (2007).*Chem. Mater*., **19**, 4702

[21] Del Toro R., Hernández P., Díaz Y., Brito J.L., (2013) *Mater. Lett.,* **107**, 231

[22] Nowick A.S., Du Y., (1995) *Solid State Ionics,* **77,** 137

[23] Shao Z., Haile S.M., (2004), Nature, **431**, 170, and references therein

[24] Zając W., Rusinek D., Zheng K., Molenda J., (2013), *Central Europ. J. Chem.,* **11**, 471

[25] Fabbri E., Bi L., Pergolesi D., Traversa E., (2012) *Adv. Mater.* **24**, 195

[26] Rezlescu N., Rezlescu E., Popa P.D., Doroftei C., Ignat M., (2014), *Composites: Part B,* **60,** 515

[27] de Souza E.C.C., Muccillo R., (2010) *Materials Research*, **13,** 385

[28] Iwahara H., Esaka T., Uchida H., Maeda N., (1981), *Solid State Ionics*, **3/4,** 359

[29] Uchida H., Maeda N., Iwahara H., (1983) *Solid State Ionics*, **11,** 117

[30] Iwahara H., Uchida H., Ono K., Ogaki K., (1988), *J. Electrochem. Soc.,* **135,** 529

[31] Choi S.M., Lee J-H., An H., Hong J., Kim H., Yoon K.J., Son J.-W., Kim B.-K., Lee H.-W., Lee J.-H., (2014), *Intern. J. Hydrogen Energy,* **39**, 12812

[32] Babu A.S., Bauri R., (2014), *Intern. J. Hydrogen Energy,* **39,** 14487

[33] Iwahara H., Asakura Y., Katahira K., Tanaka M., (2004) *Solid State Ionics,* **168,** 299

[34] Mather G.C., Garcia-Martin S., Benne D., Ritter C., Amador U., (2011) *J. Mater. Chem.*, **21**, 5764 ;

[35] Antunes I., Mather G.C., Frade J.R., Gracio J., Fagg D.P., (2010) *J. Solid State Chem.*, **183,** 2826

[36] Kreuer K.D., (2003) *Ann. Rev. Mater. Res*., **33,** 333

[37] Liu Y., Ran R., Tade M.O., Shao Z., (2014), *J. Membrane Science*, **467,** 100

[38] Moure A., Castro A,. Galy J., Moure C., Tartaj J., (2010), *J. Am. Ceram. Soc.*, **93,** 3206

[39] Moure A., Castro A., Tartaj J., Moure C., (2009), *J. Power Sources*, **188**, 489

[40] Morales M., Pérez-Falcón J.M., Moure A., Tartaj J., Espiell F., Segarra M., (2014), *Intern. J. Hydrogen Energy,* **39,** 5451

[41] Huang K., Tichy R.S., Goodenough J.B., (1998), *J. Am. Ceram. Soc*., **81**, 2565

[42] Ishihara T., Matsuda H., Takita Y., (1994) *J. Am. Chem. Soc.*, **116**, 3801

[43] Huang P.-N., Petric A, (1996), *J. Electrochem. Soc*., **143**, 1644

[44] Wolfenstine J., Huang P., Petric A, (2000), *J. Electrochem. Soc.,* **147**, 1668

[45] Rozumek M., Majewski P., Aldinger F. (2004), *J. Am. Ceram. Soc.,* **87,** 656

[46] Morales M., Roa J.J., Perez-Falcon J.M., Moure A., Tartaj J., Espiell E., Segarra M., (2014) *J. Power Sources*, **246,** 918

[47] Sanchez L., Jurado J.R., (2001), *Bol. Soc. Esp. Cerám. Vidrio,* **40,** 253

[48] Goodenough J.B., (1966), *J. Appl. Phys.*, **37**, 1415

[49] Jiang S.P., (2003), *J. Power Sources* **124**, 390, and references therein

[50] Gil V., Tartaj J., Moure C., (2009), *J. Europ. Ceram. Soc.,* **29,** 1763

[51] Adler S.B., (2004), *Chemical Reviews*, **104**, 4791

[52] Perez-Falcon J.M., Moure A., Tartaj J., (2011), *Fuel Cells*, **11,** 75

[53] Xu Q., Huang D.-P., Chen W., Zhang F., Wang B-T., (2007) *J. Alloys Compds*., **429**, 34

[54] Baumann S., Meulenberg W.A., Buchkremer H.P., (2013), *J. Europ. Ceram. Soc.,* **33**, 1251

[55] Goupil G., Delahaye T., Sala B., Lefebvre Joud F., Gauthier G., (2014) *Solid State Ionics,* **263**, 15

[56] https://fr.wikipedia.org/wiki/Willard_Frank_Libby

[57] Liu Y., Tan X., Li K., (2006), *Catalysis Reviews : Science and Engineering*, **48**,145

[58] Ciambelli P., Cimino S., De Rossi S., Faticanti M., Lisi L., Minelli G., Pettiti I., Porta P., Russo G., Turco M., (2000), *Appl. Catalysis B: Environm*., **24**, 243

[59] Liu S.-K., Lin Y.-Ch., (2014), *Catalysis Today,* **237**, 62

[60] Price P.M., Rabenberg E., Thomsen D., Misture S.T., Butt D.P., (2014), *J. Am. Ceram. Soc.,* **97,** 2241

[61] Barbero B.P., Gamboa J.A., Cadus L.E., (2006), *Appl. Catalysis B: Environm*., **65,** 21

[62] Isupova L.A., Pavlyukhin Y.T., Rogov V.A., Alikina G.M., Tsybulya S.V., Yakovleva I.S., Sadykov V.A., *MRS Proceeedings, **848**, Symposium FF*. Brese N., Jansen M., Kanatzidis M., Li J. (eds.), (2004), doi:10.1557/PROC-848-FF10.5)

[63] Isupova L.A., Tsybulya S.V., Kryukova G.N., Alikina G.M., Boldyreva N.N., Yakovleva I.S., Ivanov V.P., Sadykov V.A., (2001), *Solid State Ionics*, **141-142**, 417

[64] Isupova L.A., Yakovleva I.S., Gainutdinov I.I., Pavlyukhin Y.T., Sadykov V.A., (2004). *React. Kinet. Catal. Lett.,* **81,** 373

[65] Arun Kumar D., Selvasekarapandian S., Nithya H., Leiro J., Masuda Y., Kim S.-D., Woo S.-K., (2013) *Powder Technology,* **235,** 140

[66] Popescu I., Wu Y., Granger P., Marcu I.-C., (2014), *Appl. Catalysis A: General*, **485**, 20

[67] Luo Y., Wang X., Qian Q., Chen Q., (2014) *International J. Hydrogen Energy,* **39,** 15836

[68] http://ieeexplore.ieee.org/stamp/stamp.jsp?arnumber=522283

[69] Megaw H.D., (1945) *Nature*, **155,** 484

[70] Miyake S., Ueda R., (1946). *J. Phys. Soc. Jpn*., **1,** 32

[71] Kay H.F, Vousden P., (1949)., *Philos. Mag. Series 7,* **40,** 1019

[72] Bussmann-Holder A. (2012), *J. Phys.:Condens. Matter,* **24,** 273202

[73] Durán P., Moure C., (1986) *Mater. Chem. Phys.*, **15**, 193

[74] Dranetz A.E., Howatt G.N., Crownover J.W., (1949), *Tele-Tech, The Institute of Radio Engineers (eds.),* **8,** 29

[75] Goodman G., (1963), *J. Am. Ceram. Soc.*, **46**, 48

[76] Durán P., Fernandez-Lozano J.F., Capel F., Moure C, (1989) *J. Mater. Sci*., **24,** 447

[77] Jaffe B., Roth R.S., Marzullo S., (1954), *J. Appl. Phys.*, **25**, 809

[78] Jaffe B., Cook Jr. W.R., Jaffe H., "*Piezoelectric Ceramics"*, (1971), Academic Press (London, New York)

[79] Shindo Y., Narita F., (2012), *http://dx.doi.org/10.5772/50495*

[80] Noheda B., Cox D.E., Shirane G., Guo R., Jones B., Cross L.E., (2000), *Phys. Rev. B*, **63**, 014103

[81] Kirchhofer R., Diercks D.R., Gorman B.R., Ihlefeld J.F., Kotula P.G., Shelton C.T. Brennecka G.L., (2014), *J. Am. Ceram. Soc.,* **97,** 2677

[82] Fernandez J.F., Moure C., Villegas M., Duran P., Kosec M., Drazic G., (1998), *J. Eur. Ceram. Soc.,* **18**, 1695

[83] Saito Y., Takao H., Tani T., Nonoyama T., Takatori K., Homma T., Nagaya T., Nakamura M., (2004) *Nature*, **432**, 84

[84] Fang J., Wang X., Tian Z., Zhong C., Li L., (2010), *J. Am. Ceram Soc*., **93**, 3552

[85] Gomah-Pettry J.-R., Saïd S., Marchet P., Mercurio J-P., (2004), *J. Eur. Ceram. Soc.,* **24**, 1165

[86] Li J.-F., Wang K., Zhu F.-Y., Cheng L.-Q., Yao F.-Z., (2013), *J. Am. Ceram. Soc*., **96**, 3677

[87] Taghaddos E., Hejazi M., Safari A., (2014), *J. Am. Ceram. Soc*., **97,** 1756

[88] Aksel E., Jones J.L., (2010) *Sensors*, **10**, 1935

[89] Park S.-S., Ha J-H., Wadley H.N., (2007), *Integrated Ferroelectrics*, **95**, 251

[90] Beaudrouet E., Vivet A., Lejeune M., Santerne C., Rossignol F., Dossou-Yovo C., Mougenot M., Noguera R., (2014), *J. Am. Ceram. Soc*., **97**, 1248

[91] Chen Y.L., Yang S.F., (2011), *Adv. Appl.Ceramics*, **110**, 257

[92] Wada S., Hoshina T., Takizawa K., Ohishi M., Yasuno H., Kakemoto H., Tsurumi T., Moriyoshi C., Kuroiwa Y., (2007) *J. Korean Phys. Soc.*, **51**, 878

[93] MacChesney J.B., Potter J.F., (1965), *J. Am. Ceram. Soc*. **48**, 81

[94] Zhou D.X., Liu H., Gong S.P., Zhang D.L., (2007) *Key Engin. Mater.,* **280-283,** 1921

[95] Ertuğ B., (2013) *Amer. J. Engineer. Research,* **2**, issue 08, 1

[96] Klubovich V.V., Shut V.N., Mozzharov S.E., Trublovsky V.L., (2013) *Inorg. Materials,* **49**, 1162

[97] Zajc I., Drofenik M., (2014), *Ceramics Internat.*, **40,** 8033

[98] Whatmore R.W., (1986), *Rep. Prog. Phys*., **49**, 1335

[99] Lee M.H., Guo R., Bhalla A.S., (1998), *J. Electroceram.* **2**, 229

[100] Muralt P., (2001), *Rep. Prog. Phys*., **64**, 1339

[101] Rogalski A., (2002), *Infrared Phys. Technol*., **43**, 187

[102] Whatmore R.W, Zhang Q., Shaw C.P., Dorey R.A., Alcock J.R., (2007), *Phys. Scr*., **T129**, 6

[103] Haertling G.H., (1987), *Ferroelectrics,* **75**, 25

[104] Haertling G.H. (1971), *J. Am. Ceram. Soc.,* **54**, 303.

[105] Haertling G. H., Land C.E. (1971), *J. Am. Ceram. Soc*., **54,** 1

[106] Czerwiec M., Zachariasz R., Ilczuk J., (2007), *Archives of Acoustics*, **32**, 59

[107] Kamba S., Bovtun V., Petzelt J., Rychetsky I., Mizaras R., Brilingas A., Banys J., Grigas J., Kosec M., (2000), *J. Phys.: Condens. Matter,* **12**, 497

[108] Tong S., Ling Z., (2014), *J. Asian Ceramic Societies,* **2,** 1

[109] Goto H., Sato A., Okada M., (1998), *Electrical Engineering in Japan,* **122,** 25

[110] Fujii I., Yoshida R., Imai T., Yamazoe S., Wada T., (2013), *J. Am. Ceram. Soc*., **96,** 3782

[111] Kwok K.W., Li F., Lin D., (2011), *Funct. Mater. Lett.*, **4,** 237

[112] Li F., Kwok K.W., (2013), *J. Eur. Ceram. Soc*., **33,** 123;

[113] Li F., Kwok K.W, (2013), *J. Am. Ceram. Soc.,* **96,** 3557

[114] Stock C., Van Eijck L., Fouquet P., Maccarini M., Gehring P.M., Xu G., Luo H., Zhao X., Li J.-F., Viehland D., (2010), *Phys. Rev. B,* **81**, 144127

[115] Gehring P.M., Park S.-E., Shirane G., (2000), *Phys. Rev. Lett.*, **84,** 5216

[116] Shirane G., Gehring P.M., (2003) *Ceramic Transactions*, in *"Morphotropic Phase Boundary Perovskites, High Strain Piezoelectric and Dielectric Ceramics"*, Guo R., Nair K.M., Vong-Ng W.K., Bhalla A.S., Vieland D., Suvorov D., Wu C., Hirano S.-I. (eds), American Ceramic Society, vol 136, 17

[117] Tomita Y., Kato T., (2013), *J. Phys. Soc. Jpn.,* **82,** 063002

[118] Kim Y.J., Lee J.H., (2008), *J. Korean Vacuum Soc.,* **17,** 148

[119] Kojima S., Ahart M., Sivasubramanian V., Bokov A.A., Ye Z.-G., (2012) *J. Adv. Dielectrics,* **2**, 1241004

[120] Bokov A.A., Ye Z.-G., (2006), *J. Mater. Science*, **41**, 31

[121] Akbas M.A., Davies P.K., (1997) *J. Am. Ceram. Soc.,* **80,** 2933

[122] Skulski R., Bochenek D., Wawrzała P., Dercz G., Brzezinska D., (2013), *Int. J. Appl. Ceram. Technol*., **10,** 330

[123] Frenkel A.I., Pease D.M., Giniewicz J., Stern E.A., Brewe D.L., Daniel M., Budnick J., (2004), *Phys. Rev. B,* **70**, 014106

[124] Zhang R., Jiang B., Cao W., Amin A., (2002), *J. Materials Sci. Letters,* **21**, 1877

[125] Li F., Jin L., Xu Z., Zhang S., (2014), *Appl. Phys. Rev.,* **1**, 011103

[126] Uchino K., Nomura S., Cross L.E., Jang S.J., Newnham R.E., (1980*). J. Appl. Phys.,* **51**, 1142

[127] Jang S.J., Uchino K., Nomura S., Cross L.E., (1980), *Ferroelectrics,* **27,** 31

[128] Uchino K., Nomura S., Cross L.E., Newnham R.E., Jang S.J., (1981), *J. Mater. Sci.,* **16**, 569

[129] Aksel E., Jakes P., Erdem E., Smyth D.M., Ozarowski A., van Tol J., Jones J.L., Eichel R.-A., (2011), *J. Am. Ceram. Soc,* **94,** 1363

[130] Glaum J., Simons H., Acosta M., Hoffman M., (2013), *J. Am. Ceram. Soc*. **96**, 2881

[131] Kumar N., Ansell T.Y., Cann D.P., (2014), *J. Appl. Phys.,* **115**, 154104

[132] Kumar N., Cann D.P., (2013), *J. Appl. Phys*., **114**, 054102

[133] Reaney I.M., Iddles D., (2006), *J. Am. Ceram. Soc*., **89,** 2063

[134] Cava R.J., (2001), *J. Mater. Chem.,* **11**, 54

[135] Sebastian M.T., in *"Dielectric Materials for Wireless Communication"*, Elsevier Science (UK, NL), 2008

[136] Davies P.K., Tong J., Negas T., (1997), *J. Am. Ceram. Soc.,* **80,** 1727

[137] Diao C-L., Wang C-H., Luo N-N., Qi Z-M;, Shao T., Wang Y-Y., Lu J., Shi F., Jing X-P., (2013), *J. Am. Ceram. Soc*., **96**, 2898

[138] Ma P.P., Yi L., Liu X.Q., Li L., Chen X.M., (2013), *J. Am. Ceram. Soc*., **96,** 1795

[139] Nomura S., (1983), *Ferroelectrics*, **49**, 61

[140] Fu M.S., Liu X.Q., Chen X.M., Zeng Y.W., (2010), *J. Am. Ceram. Soc*., **93,** 787

[141] Ioachim A., Toacsan M.I., Nedelcu L., Banciu M.G., Dutu C.A. Andronescu E., Jinga S., Nita P., Alexandru H.V., (2007), *J. Optoelectronics Adv. Mater*., **9,** 1833

[142] Dai J.-Q., Song Y.-M., Zhang H., (2014), *Ferroelectrics*, **467**, 22

[143] Brik M.G., (2012), *J. Phys. Chem. Solids*, **73,** 252

[144] Kuo D.H., Chou C.Y., Kuo Y.K., (2010), *Int. J. Appl. Ceram. Technol.*, **7,** 217

[145] Sleight A.W., Gillson J.L., Bierstedt P.E., (1975), *Solid State Commun*., **17,** 27

[146] Chu C.W., Hor P.H., Meng R.L., Gao L., Huang Z.J., (1987), *Science*, **235**, 567

[147] Claeson T., Boyce J.B., Bridges F., Geballe T.H., Remeika J.M., Sleight A.W., (1989), *Physica C,* **162-164,** 544

[148] Larsson S**.**, (2013), *J. Modern Physics*, **4,** 29

[149] Stoneham A.M., Smith L.W. (1991) *J. Phys.: Condens. Matter*, **3,** *225*

[150] Cava R. J, (2000), *J. Am. Ceram. Soc.,* **83,** 5

[151] Wang K.F., Liu J.-M., Ren Z.F., (2009), *Adv. Phys.*, **58**, 321

[152] Fiebig M., (2005), *J. Phys. D: Appl. Phys.* **38,** R123

[153] Sahu J.R., Serrao C.R., Ray N., Waghmare U.V., Rao C.N.R., (2007). *J. Mater. Chem*., **17**, 42

[154] Ju S., Cai T.-Y., Guo G.-Y., (2009), *J. Chem. Phys.,* **130**, 214708

[155] Gareeva Z.V., Popkov A.F., Soloviov S.V., Zvezdin A.K., (2013), *Phys. Rev B*, **87,** 214413

[156] Yang C.-H., Koo J., Song C., Koo T.Y., Lee K.-B., Jeong Y.H., (2006), *Phys. Rev B*, **73**, 224112

[157] Wollan E.O., Koehler W.C., (1955), *Phys. Rev.,* **100,** 545

[158] Kawano H., Kajimoto R., Kubota M., Yoshizawa H., (1996), *Phys. Rev B*, **53,** 2202

[159] Tokura Y., (2006), *Rep. Prog. Phys*., **69,** 797

[160] Chahara K.-I., Ohno T., Kasai M., Kozono Y., (1993), *Appl. Phys. Lett.,* **63,** 1990

[161] Jin S., Tiefel T.H., McCormack M., Fastnacht R.A., Ramesh R., Chen L.H., (1994), *Science* **264,** 413

[162] Kusters R.M., Singleton J., Keen D.A., McGreevy R., Hayes W., (1989), *Physica B,* **155**, 362

[163] von Helmolt R., Wecker J., Holzapfel B., Schultz L., Samwer K., (1993), *Phys. Rev. Lett.,* **71**, 2331

[164] Searle C.W., Wang S.T., (1969), *Canad. J. Phys.,* **47**, 2703

[165] Yahia M., Batis H., (2003), *Eur. J. Inorg. Chem.,* **13**, 2486

[166] Demin R.V., Koroleva L.I., Muminov A.Z., Mukovskii Ya.M., (2006), *Phys. Solid State,* **48,** 322

[167] Mandal P., Ghosh B., (2003), *Phys. Rev B*, **68**, **0**14422

[168] Tokura Y., Tomioka Y., (1999), *J. Magn. Magn. Mater.,* **200,** 1

[169] Jirak Z., Hejtmanek J., Pollert E., Martin C., Maignan A., Raveau B., Savosta M.M., Tomioka Y., Tokura Y., (2001), *J. Appl. Phys.*, **89, 7**404

[170] Peña O., Bahout M., Ma Y., Guizouarn T., Gutiérrez D., Durán P., Moure C., (2003), *Mater. Science Engin.* B, **104,** 126

[171] Antunes A.B., Gil V., Moure C., Peña O., (2007), *J. Europ. Ceram. Soc.,* **27,** 3927

[172] Peña O., Barahona P., Gil V., Tartaj J., Moure C., (2008), *Bol. Soc. Esp. Ceram. V.,* **47,** 138

[173] Moure C., Moure A., Tartaj J., Peña O., (2010), *Bol. Soc. Esp. Ceram. V.,* **49,** 423

[174] Vijayanandhini K., Simon Ch., Pralong V., Bréard Y., Caignaert V., Raveau B., Mandal P., Sundaresan A., Rao C.N.R., (2009) *J. Phys.: Condens. Matter,* **21,** 486002

[175] Peña O, Antunes A.B, Baibich M.N., Lisboa-Filho P.N., Gil V, Moure C. (2007) *J. Magn. Magn. Mater.,* **312,** 78

[176] Antunes A.B., Baibich M.N., Gil V., Moure C., Allegret-Maret V., Peña O., (2008) *J. Magn. Magn. Mater.,* **320**, e464

[177] Antunes A.B., Moure C., Moure A., Peña O., (2010), *J. Low Temp. Phys.*, **159**, 114

[178] Hardy V., Majumdar S., Crowe S.J., Lees M.R., Paul D.McK., Hervé L., Maignan A., Hébert S., Martin C., Yaicle C., Hervieu M., Raveau B., (2004), *Phys. Rev B*, **69,** 020407

[179] Tang T., Tien C., Huang R.S., Hou B.Y., (2008) *Solid State Commun.,* **146,** 133

[180] Meiklejohn W.H., Bean C. P., (1956), *Phys. Rev.*, **102**, 1413.

[181] Rana R., Pandey P., Singh, R.P., Rana D.S., (2014) *Nature*, DOI: 10.1038/srep04138

[182] Gibert M., Zubko P., Scherwitzl R., Íñiguez J., Triscone J.-M., (2012), *Nature Materials*, **11**, 195

[183] Pradheesh R., Nair H.S., Sankaranarayanan V., Sethupathi K. (2012), *App. Phys. Lett.*, **101**, 142401

Table 1

Properties and applications of perovskites.

Property	Application	Material
Proton conductivity	SOFC electrolyte	$BaCeO_3$, $SrCeO_3$, $BaZrO_3$
Ionic conductivity	Solid electrolyte Hydrogen sensor H_2 production/extraction	$(La,Sr)(Ga,Mg)O_{3-\delta}$
Mixed conductivity	SOFC electrode Piezoelectric transducer	$La(Sr,Ca)MnO_{3-\delta}$, $LaCoO_3$ $(La,Sr)(Co,Fe)O_{3-\delta}$ $BaTiO_3$, $Pb(Zr,Ti)O_3$ $Pb(Mg,Nb)O_3$
Catalytic	Catalyst	$LaFeO_3$, $La(Ce,Co)O_3$
Electrical / dielectric	Multilayer capacitor Dielectric resonator Thin film resistor	$BaTiO_3$, $BaZrO_3$
Ferroelectric / piezoelectric	Thermistor, actuator Thin film resistor	
Magnetic	Magnetic memory Ferromagnetism	$GdFeO_3$, $LaMnO_3$
Optical	Electrooptical modulator Laser	$(Pb,La)(Zr,Ti)O_3$ $YAlO_3$, $KNbO_3$
Superconductivity	Superconductor	$Ba(Pb,Bi)O_3$, $BaKBiO_3$ $YBa_2Cu_3O_{7-\delta}$

Table 2

Some compounds and their properties as ferroelectric materials

Material	Properties	Applications
$BaTiO_3$	Dielectric	Capacitors, Sensors
$(Ba,Sr)TiO_3$	Pyroelectric	Pyroelectric sensors
$PbTiO_3$	Pyroelectric	Pyroelectric sensors
	Piezoelectric	Electromechanical transducers
$Pb(Zr,Ti)O_3$	Dielectric	Non-volatile memories
	Pyroelectric	Pyroelectric sensors
	Piezoelectric	Electromechanical transducers
$(Pb,La)(Zr,Ti)O_3$	Pyroelectric	Pyroelectric sensors
	Electrooptic	Waveguides, optical displays
$LiNbO_3$	Piezoelectric	Surface acoustic waves
$(LiNbO_3/Ti)$	Electrooptic	Optical modulators
$K(Ta,Nb)O_3$	Pyroelectric	Pyroelectric sensors
	Electrooptic	Waveguide devices
$Pb(Mg_{1/3}Nb_{2/3}Ti)O_3$	Dielectric	Capacitors, Memories

Table 3

Polar oxides with pyroelectric / pyroelectric-electrocaloric properties

Polar Dielectric		**Crystal Structure**	**Crystal Symmetry**
Poled Ceramics			
BTO :	$BaTiO_3$	Perovskite	Tetragonal, 4*mm*/∞*m*
PZT :	$Pb(Zr_{0.95}Ti_{0.05})O_3$	Perovskite	Trigonal, 3*m* /∞*m*
BST :	$Ba_xSr_{1-x}TiO_3$	Perovskite	Tetragonal 4*mm*/∞*m*
STO :	$SrTiO_3$	Perovskite	Cubic, *Pm*3*m* (Oh1)

Figures captions.

Figure 1. Ideal (cubic) perovskite structure. Cation B is surrounded by 6 oxygen anions in octahedral configuration. A is surrounded by 12 oxygen anions (from http://www.kek.jp/en/NewsRoom/Release/20140516150000/#06)

Figure 2. $SrTiO_3$, an example of an ideal cubic perovskite (from http://www.princeton.edu/~cavalab/tutorials/public/structures/perovskites.html)

Figure 3. $BaTiO_3$, tetragonal-type perovskite structure (from http://commons.wikimedia.org/wiki/File:BaTiO3_oxygen_coordination.png)

Figure 4. $LaAlO_3$, rhombohedrally distorted perovskite structure (from Ref. [5])

Figure 5. Distorted orthorhombic perovskite: (a) $GdFeO_3$ type structure, (b) ideal cubic perovskite (from http://cheminfo2011.wikispaces.com/XiangLiu-Final)

Figure 6. Double perovskite Sr_2GdRuO_6, with monoclinic-type distortion and $P2_1/n$ space group (from Ref. [7])

Figure 7. Fragments of the crystal structure of $BiMnO_3$ viewed along the a-axis at (a) 300 K and (b) 550 K; only MnO_6 octahedra are shown. The black solid lines present the longest Mn-O bond lengths. Space group C2 (from Ref. [9])

Figure 8. Structure of the A-site scandium perovskite $(Sc_{0.94}Mn_{0.06})Mn_{0.65}Ni_{0.35}O_3$. (a) view down [001] (pseudocubic a-axis). (b) view along [110] (pseudocubic b-axis). (c) view down [11$\bar{0}$] (pseudocubic c-axis). (d) A site ions, only shown in a projection close to the view down the a-axis (from Ref. [10])

Figure 9a. Flow diagram for the preparation of modified lead titanates (top) and XRD patterns of washed, co-precipitated and calcined oxalates (bottom) (from Ref. [19])

Figure 9b. Microstructure of modified lead titanates M-$PbTiO_3$ (M = La, Nd, Sm, Ca) sintered at 1150 ºC (M = rare-earths) and 1100 ºC (M = Ca). (a) La-$PbTiO_3$, (b) Nd-$PbTiO_3$, (c) Sm-$PbTiO_3$, and (d) Ca-$PbTiO_3$ (from Ref. [19])

Figure 10. Flow diagram of Pechini-type synthesis (examples : Me = Ba, Sr, Ca ; Ln = La, Nd, Sm ; M = Mn, Fe, Cr)

Figure 11a. Schemes for a solid oxide fuel cell (SOFC) with proton-conductive electrolyte (from Refs. [24], left-hand side, and [25], right-hand side)

Figure 11b. Scanning electron microscopy image (SEM) of the fractured cross section of a BZPY10-based ($BaZr_{0.7}Pr_{0.1}Y_{0.2}O_{3-\delta}$) single cell after fuel-cell testing (from Ref. [25])

Figure 12. Temperature evolution of the lattice parameters (bottom) of the different crystallographic phases of $BaTiO_3$ and the different crystalline structures (top) from rhombohedral (low temperature phase) to cubic (high temperature phase) (from Refs. [70,75])

Figure 13. Hysteresis loop and electric polarization of piezoelectric ceramics (from Ref. [73])

Figure 14. Pseudobinary $PbZrO_3$-$PbTiO_3$ system. a) phase diagram showing the morphotropic phase boundary, MPB (from http://electronicstructure.wikidot.com/first-principles-study-of-piezoelectricity-in-pzt), b) Revised phase diagram showing the crystalline symmetry of the different phases (from Ref. [79])

Figure 15. (a) Transversal cross section of a multilayer ceramic capacitor (MLCC) device ; (b) SEM image of a cross section of a $BaTiO_3$ multilayer ceramic capacitor (from "History of the first ferroelectric oxide, $BaTiO_3$" ; http://ceramics.org/wp-content/uploads/2009/03/elec_division_member_papers1.pdf)

Figure 16a. Conductivity anomaly in semiconducting (Sm-doped) $BaTiO_3$ ceramic (from Ref. 75)

Figure 16.b Cross section of a $BaTiO_3$-based positive-temperature-coefficient (PTC) device (from Ref. 94])

Figure 16c. Fabrication process of a PTC multilayer chip (from Ref. 94])

Figure 17. Quaternary phase diagram of the PLZT system (from "Structure having light modulating film and optical controlling device using same", Patent EP-1662298-A1 ; fig.8 / see http://www.google.com/patents/EP1662298A1)

Figure 18.a) Schematic diagram of a PLZT modulator (PLZT : lead lanthanum zirconium titanate) (from http://www.marekczerwiec.com/artykuly/TRANSPARENT_PLZT_CERAMICS.pdf)

Figure 18.b) An example of applications for transparent PLZT, the visor anti-flash (from http://www.flightgear.dk/flash.htm)

Figure 18.c) La-undoped (left) and 3 mol% La-doped (right) 0.9PMN-0.1PT ceramics (PMN : $Pb(Mg_{1/3}Nb_{2/3})O_3$; PT : $PbTiO_3$) (from Ref. [110])

Figure 19. Temperature dependence of real and imaginary parts of the relative dielectric permittivity in a crystal of $Pb(Mg_{1/3}Nb_{2/3})O_3$ (PMN). Insert : universal relaxor dispersion (from Ref. [120])

Figure 20 Comparative schemes of the relaxor and normal ferroelectric compounds (from http://guava.physics.uiuc.edu/~nigel/courses/563/Essays_2005/PDF/delgado.pdf)

Figure 21 : (a) Schematic illustration of a 1:2 cation-ordering in $Ba(Zn_{1/3}Ta_{2/3})O_3$. Upper left shows two of the possible {111} directions for the ordering of Zn and Ta. Center image shows a 1:2 ordering for one of the orientational variants (oxygen anions omitted for clarity). Bottom shows an idealized $[110]_{subcell}$ projection of the ordered structure : open circles, oxygen anions; shaded circles, Ba cations; the anions that project onto the A-site positions are omitted for clarity (from Ref. [136]). (b) Double perovskite structure of $Ba(Mg_{1/2}W_{1/2})O_3$ (BMW); primitive cell in the unit cell (only cations are shown) (from Ref. [137])

Figure 22. a) Unit cell of $RNiO_3$ with distorted NiO_6 octahedra. b) The Ni-O-Ni bond angle as a measure of the lattice distortion ; for different rare-earths the lattice distortion (described by γ) changes. c) Phase diagram of $RNiO_3$ as a function of the tolerance factor (from http://physics.unifr.ch/de/page/547/)

Figure 23. Crystalline structure of superconducting $YBa_2Cu_3O_{7-\delta}$ (see, for instance, J.D. Jorgensen et al, Phys. Rev. B, 41 (1990) 1863)

Figure 24. Temperature dependence of the resistivity of $La_{1-x}Sr_xMnO_3$ with x=0.3, at various magnetic fields (from http://www2.lbl.gov/Science-Articles/Archive/colossal-magnetoresistance.html)

Figure 25. Temperature dependence of the ZFC (a) and FC (b) magnetizations, under given applied fields, for composition $ErCo_{0.50}Mn_{0.50}O_3$ (from Ref. [175])

Figure 26. Magnetization loop at 2 K for $ErCo_{0.50}Mn_{0.50}O_3$ while increasing (open symbols) and decreasing the magnetic field (solid symbols). The inset shows the temperature (T_{comp}) of reverse magnetization (from Ref. [176])

Figure 27. Top : Magnetization loops at 2.5 K for (**a**) $EuCo_{0.50}Mn_{0.50}O_3$ and (**b**) $EuNi_{0.50}Mn_{0.50}O_3$. Bottom : Magnetization loops at 2.5 K for (**a**) $DyCo_{0.50}Mn_{0.50}O_3$ and (**b**) $DyNi_{0.50}Mn_{0.50}O_3$ (from Ref. [177])

Figure 28. Maximum M_{shift} (~35%) for the optimized bilayer [$La_{0.3}Sr_{0.7}FeO_3$(110 nm)/$SrRuO_3$(10 nm)] (from Ref. [181])

Figure 29. Exchange bias and memory effects in the double perovskite Sr_2FeCoO_6. The field-cooled hysteresis curves at different cooling fields H_{FC} display vertical displacement that signify FM clusters present in the system (from Ref. [183])

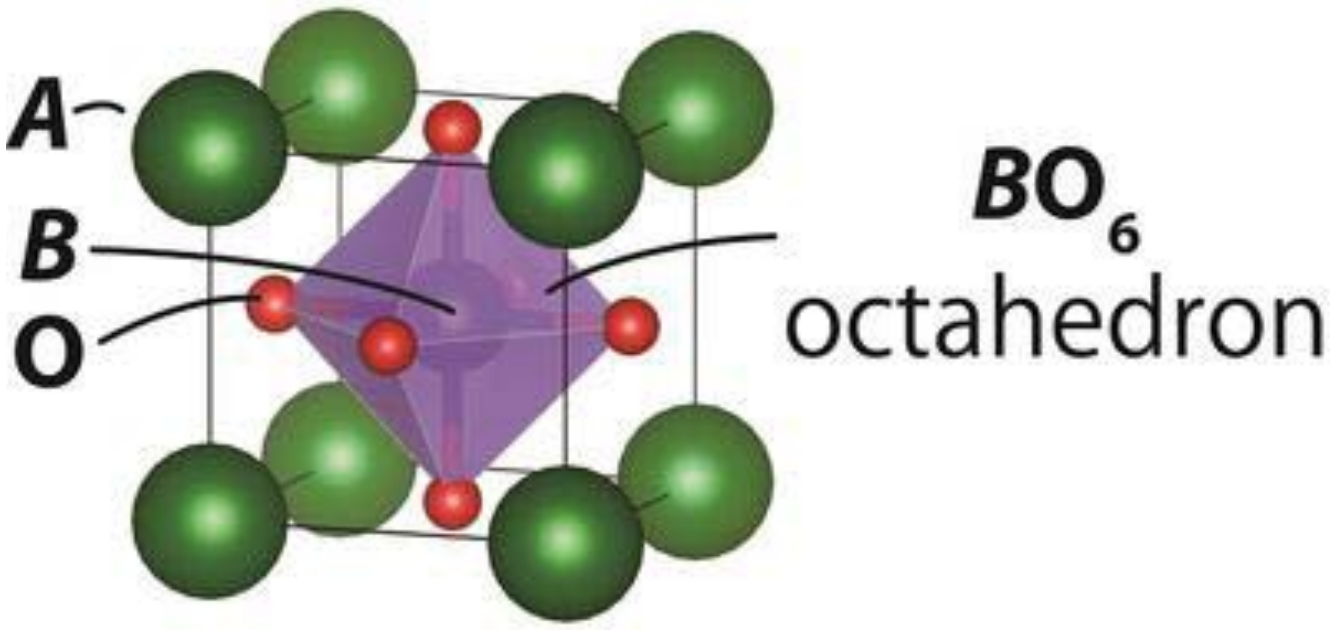

Figure 1

Ideal (cubic) perovskite structure. Cation B is surrounded by 6 oxygen anions in octahedral configuration.
A is surrounded by 12 oxygen anions
(from http://www.kek.jp/en/NewsRoom/Release/20140516150000/#06)

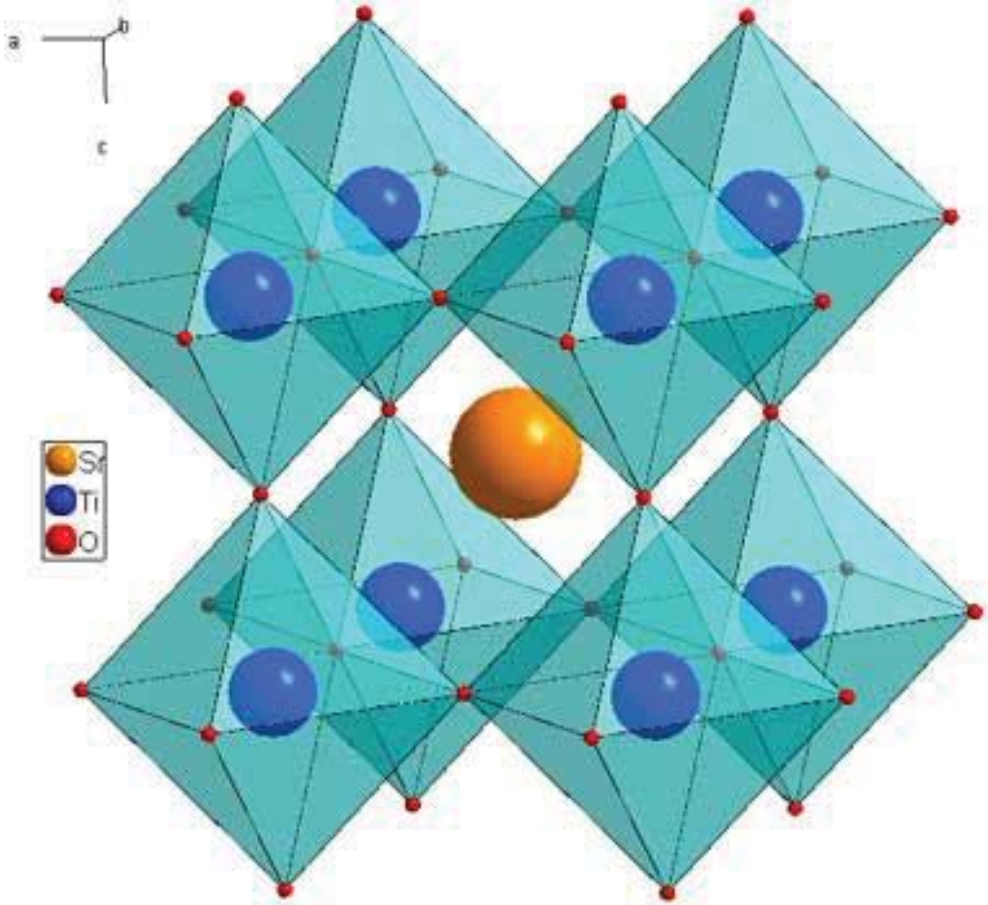

Figure 2

$SrTiO_3$, an example of an ideal cubic perovskite
(from http://www.princeton.edu/~cavalab/tutorials/public/structures/perovskites.html)

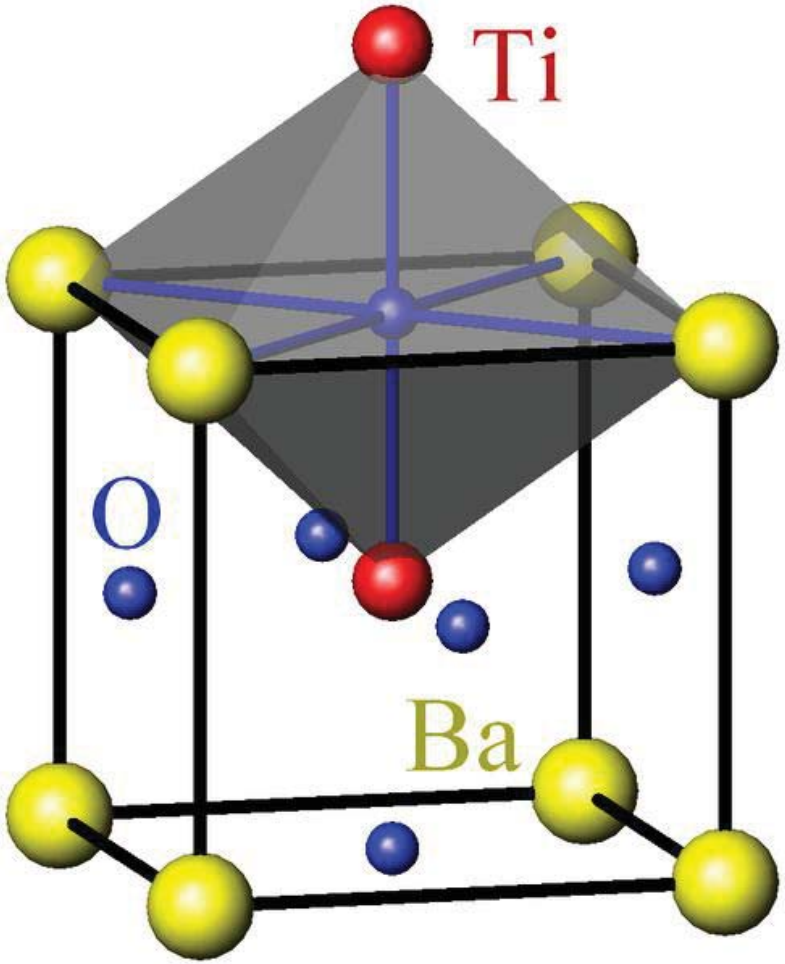

Figure 3

$BaTiO_3$, tetragonal-type perovskite structure
(from http://commons.wikimedia.org/wiki/File:BaTiO3_oxygen_coordination.png)

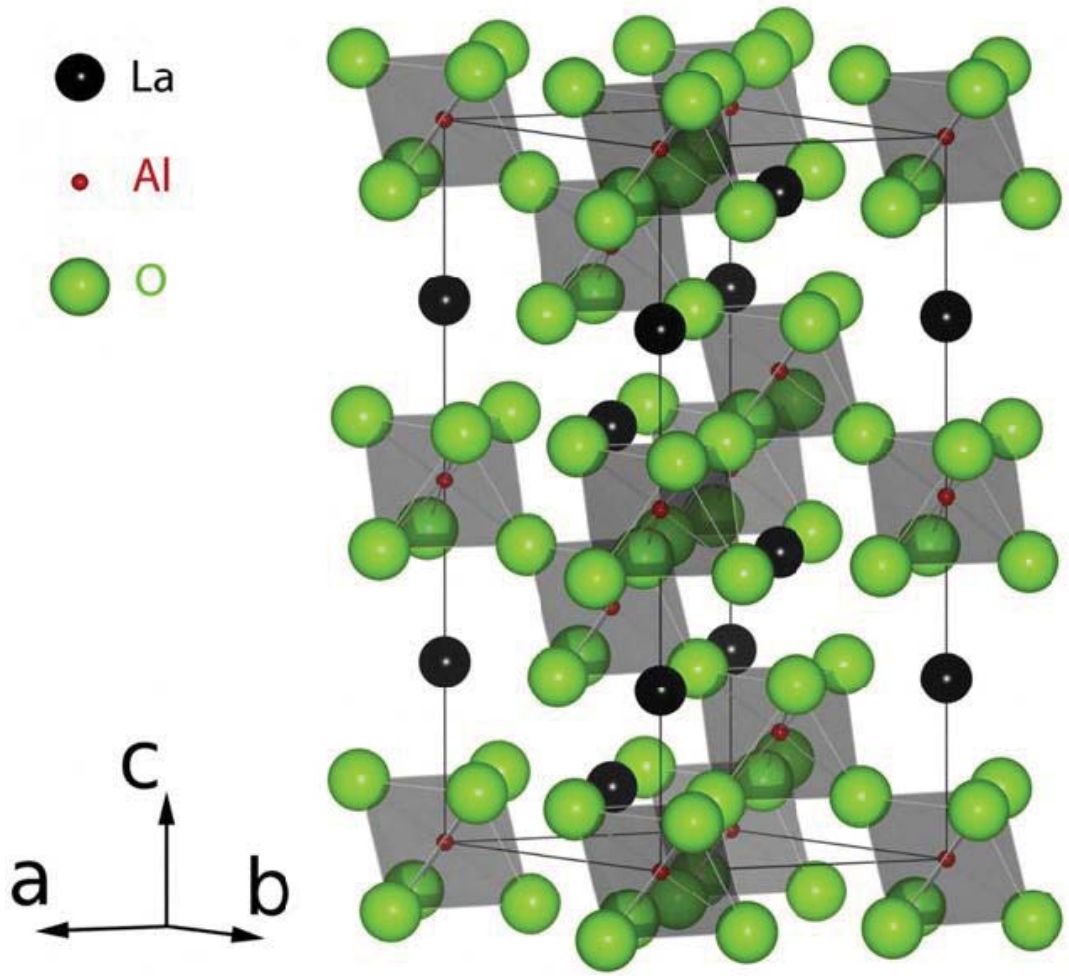

Figure 4

$LaAlO_3$, rhombohedrally distorted perovskite structure
(from Ref. [5])

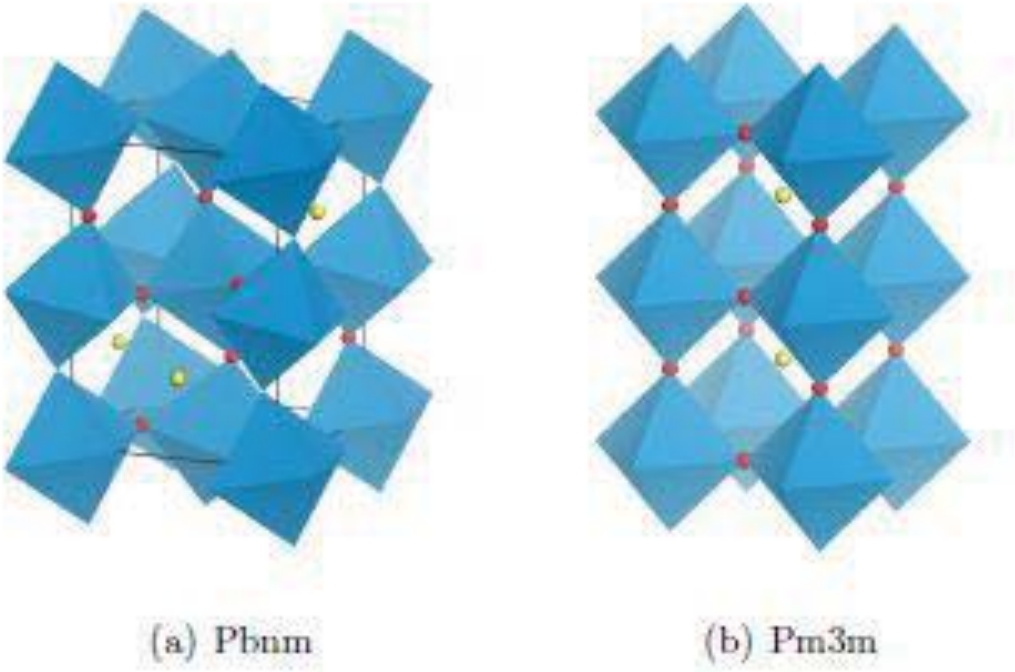

Figure 5

Distorted orthorhombic perovskite: (a) $GdFeO_3$ type structure, (b) ideal cubic perovskite
(from http://cheminfo2011.wikispaces.com/XiangLiu-Final)

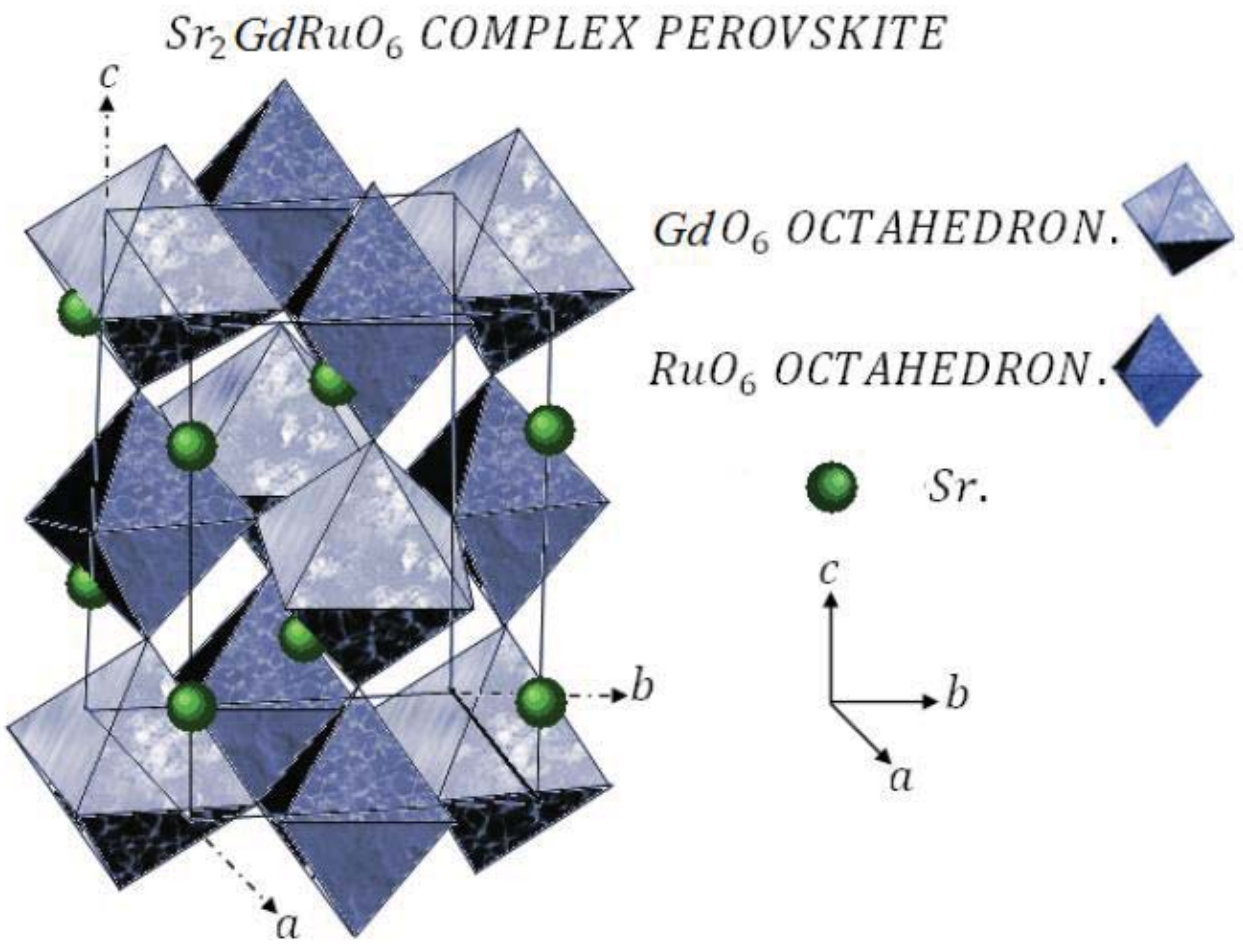

Figure 6

Double perovskite Sr_2GdRuO_6, with monoclinic-type distortion and $P2_1/n$ space group (from Ref. [7])

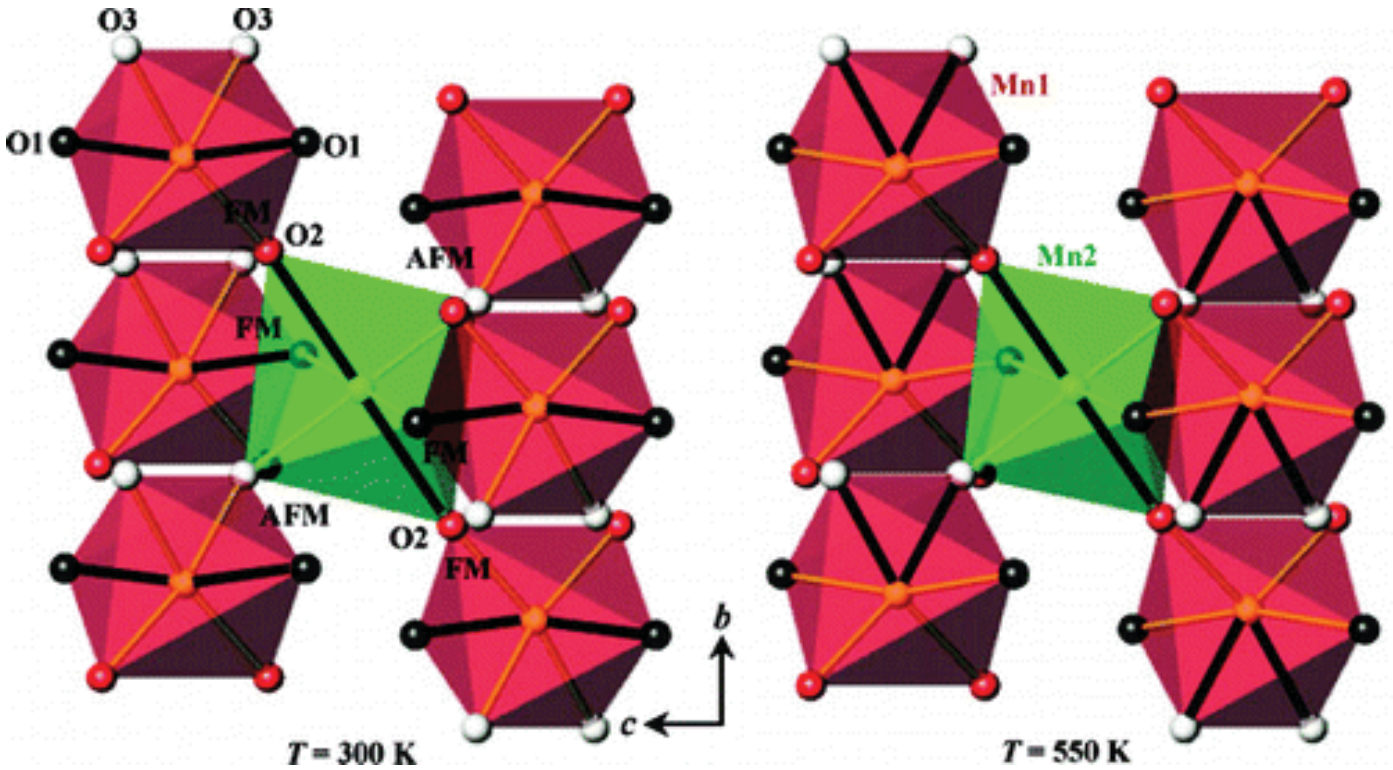

Figure 7

Fragments of the crystal structure of $BiMnO_3$ viewed along the a-axis at (a) 300 K and (b) 550 K; only MnO_6 octahedra are shown. The black solid lines present the longest Mn-O bond lengths. Space group C2 (from Ref. [9])

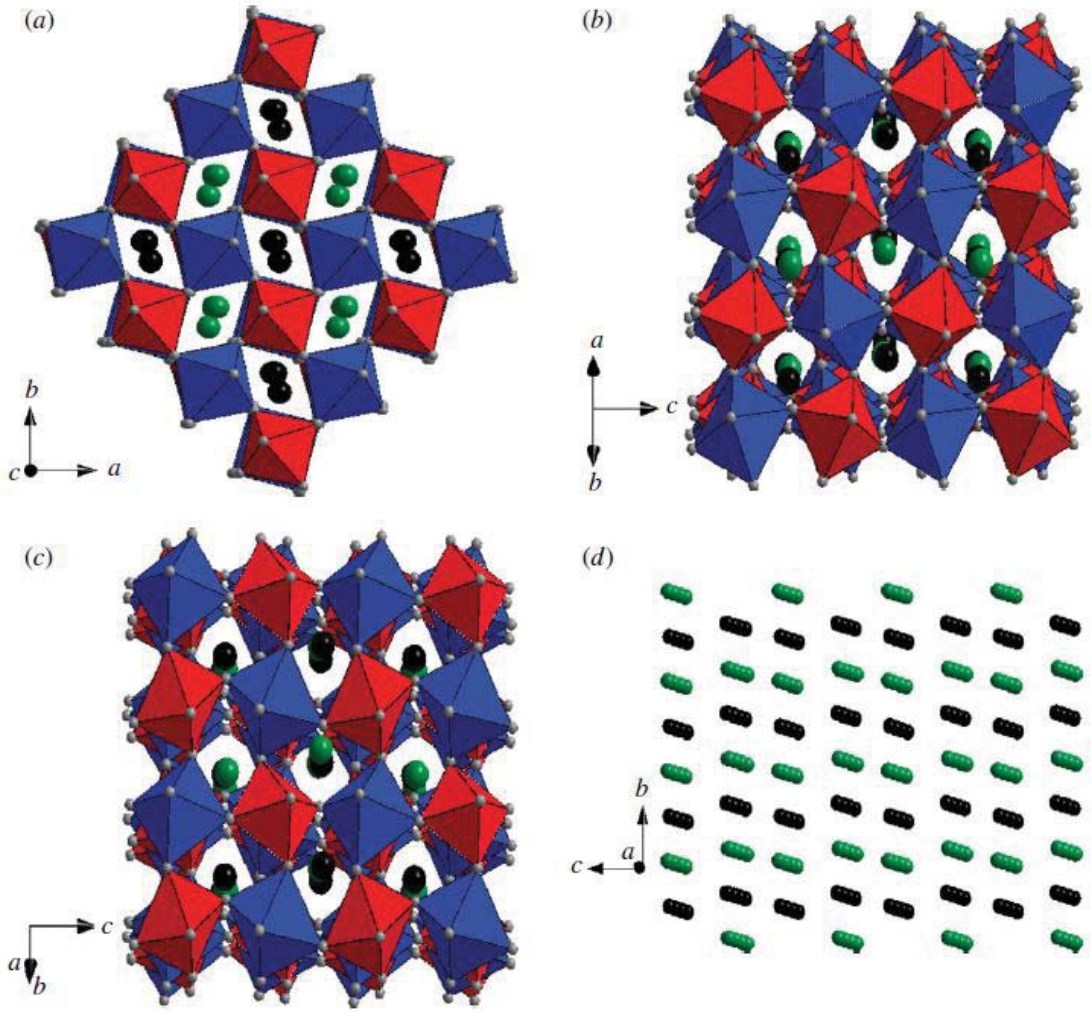

Figure 8

Structure of the A-site scandium perovskite $(Sc_{0.94}Mn_{0.06})Mn_{0.65}Ni_{0.35}O_3$. (a) view down [001] (pseudocubic a-axis). (b) view along [110] (pseudocubic b-axis). (c) view down [11$^-$0] (pseudocubic c-axis). (d) A site ions, only shown in a projection close to the view down the a-axis
(from Ref. [10])

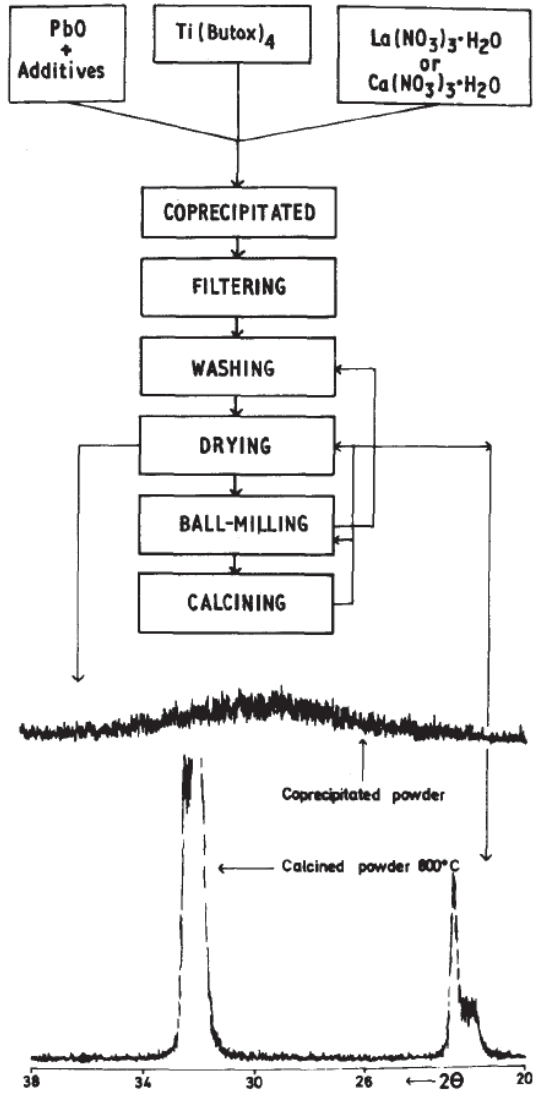

Figure 9.a

Flow diagram for the preparation of modified lead titanates (top) and XRD patterns of washed, co-precipitated and calcined oxalates (bottom)
(from Ref. [19])

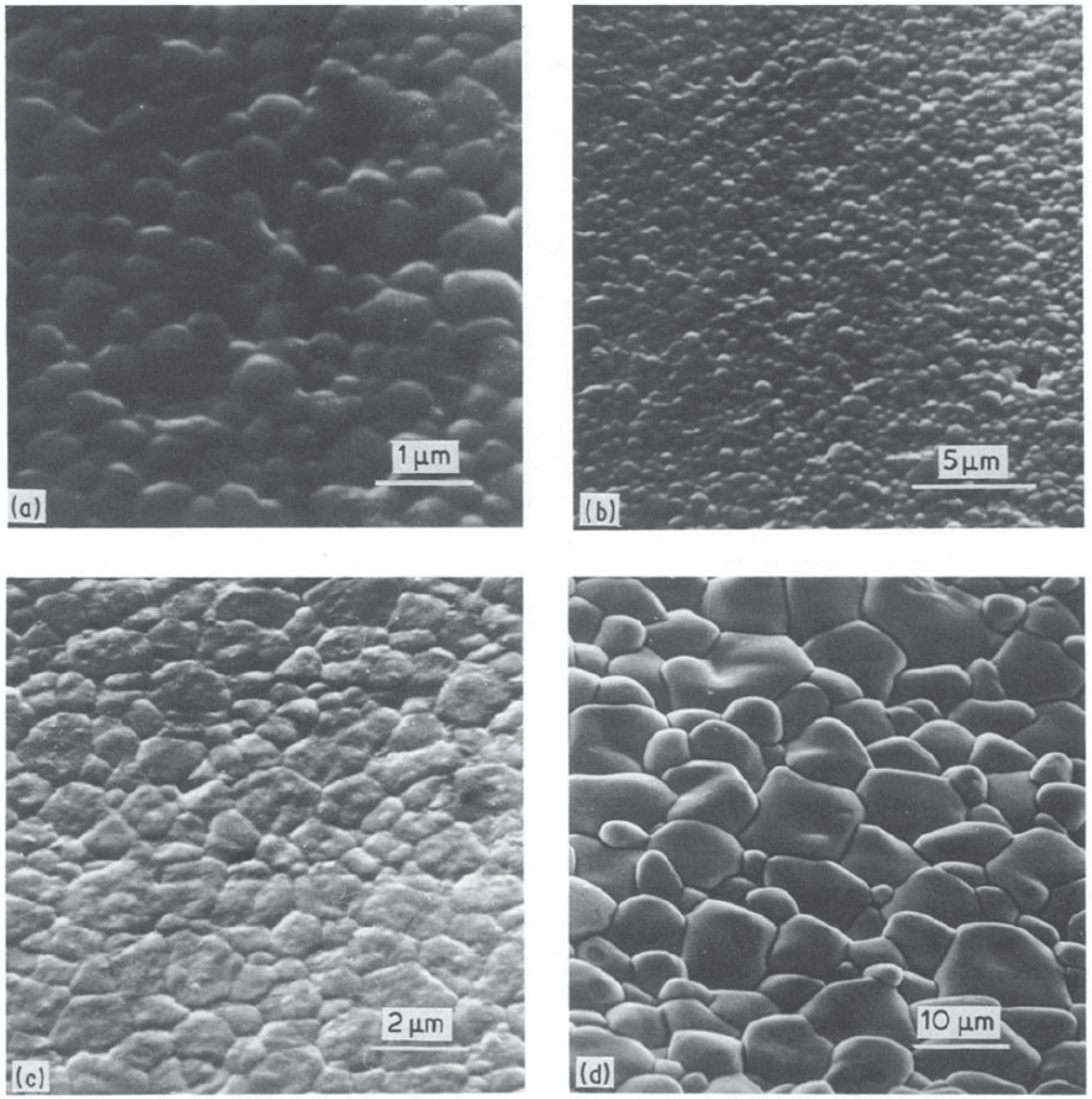

Figure 9.b

Microstructure of modified lead titanates M-$PbTiO_3$ (M = La, Nd, Sm, Ca) sintered at 1150 ºC (M = rare-earths) and 1100 ºC (M = Ca). (a) La-$PbTiO_3$, (b) Nd-$PbTiO_3$, (c) Sm-$PbTiO_3$, and (d) Ca-$PbTiO_3$ (from Ref. [19])

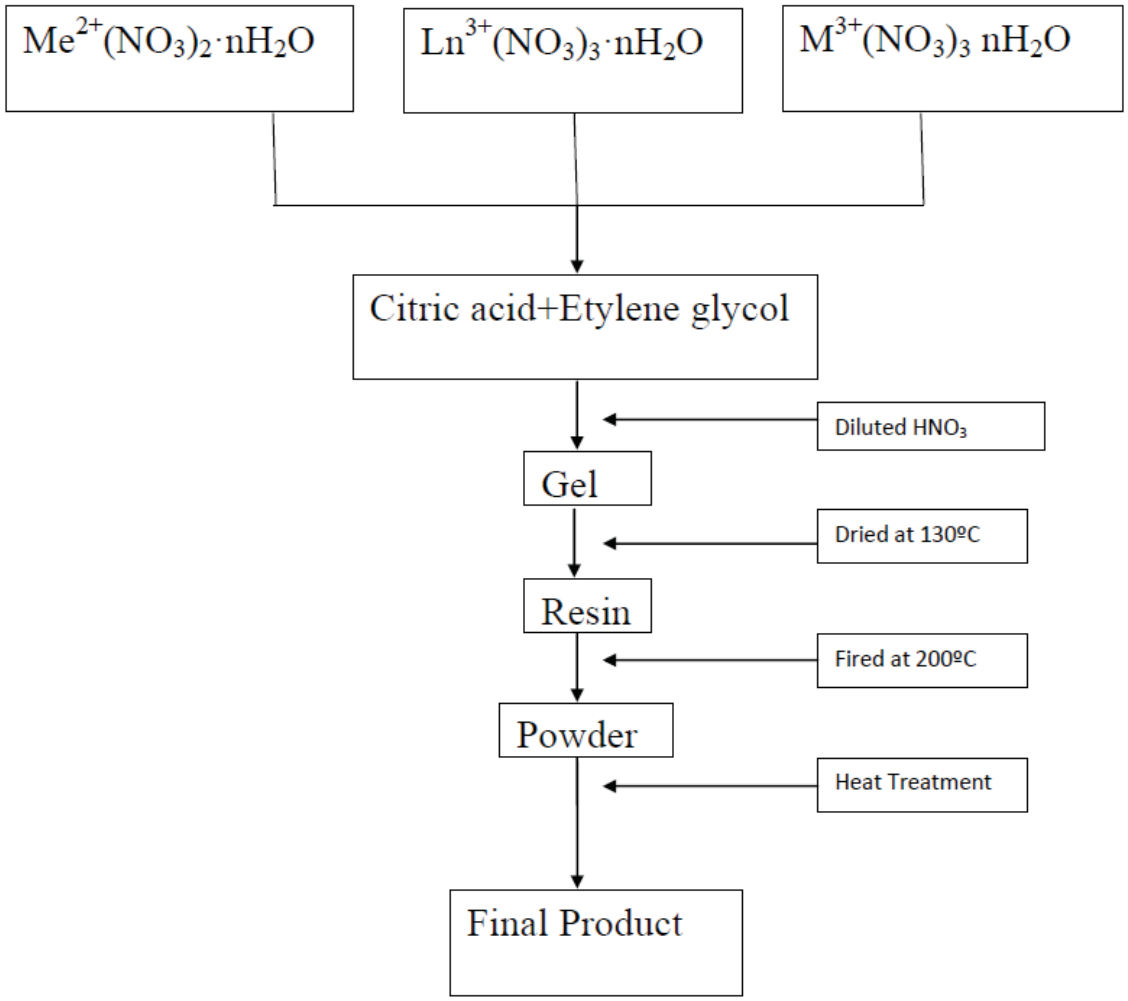

Figure 10

Flow diagram of Pechini-type synthesis (examples : Me = Ba, Sr, Ca ; Ln = La, Nd, Sm ; M = Mn, Fe, Cr)

Figure 11.a

Schemes for a solid oxide fuel cell (SOFC) with proton-conductive electrolyte (from Refs. [24], left-hand side, and [25], right-hand side)

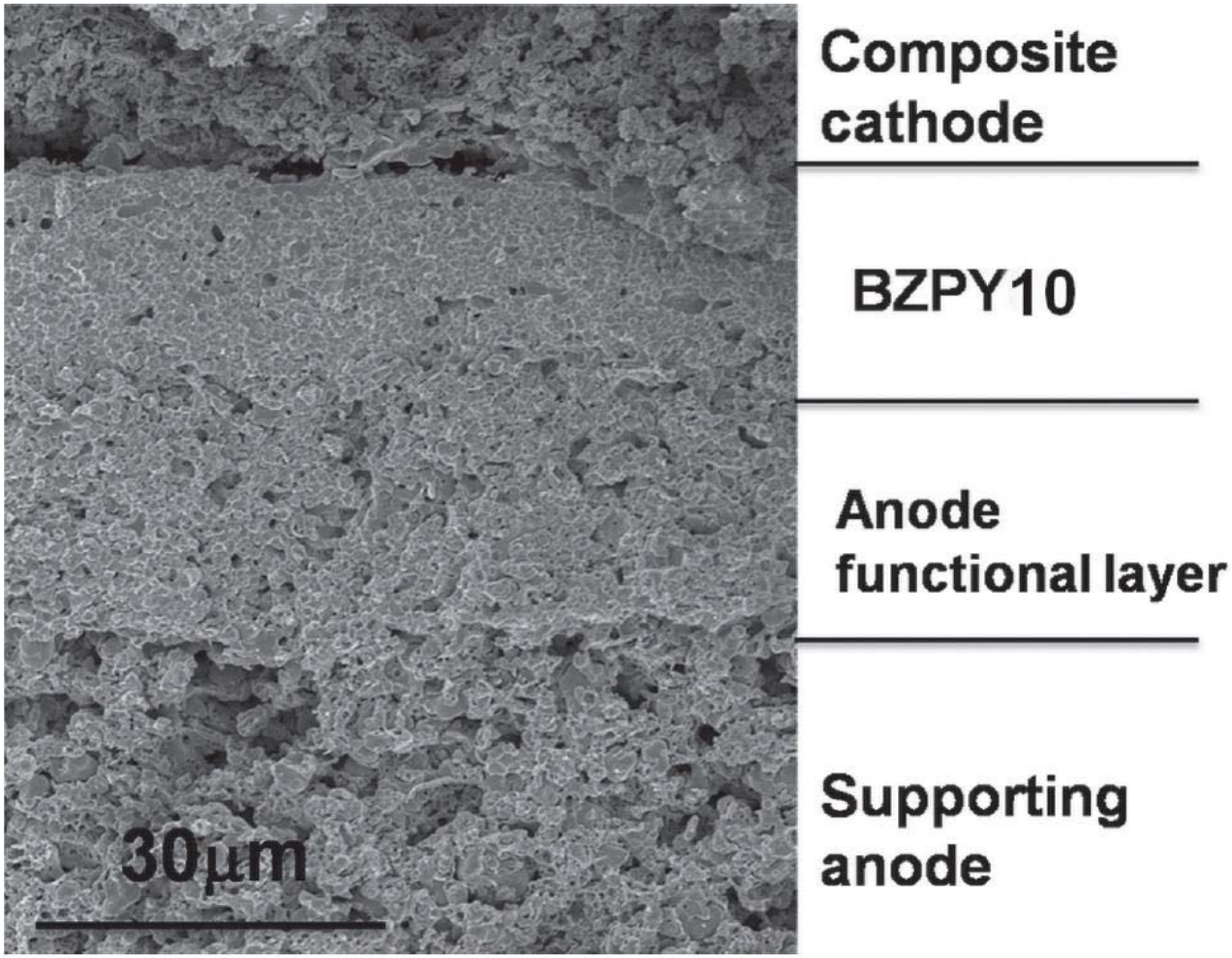

Figure 11.b

Scanning electron microscopy image (SEM) of the fractured cross section of a BZPY10-based ($BaZr_{0.7}Pr_{0.1}Y_{0.2}O_{3-d}$) single cell after fuel-cell testing (from Ref. [25])

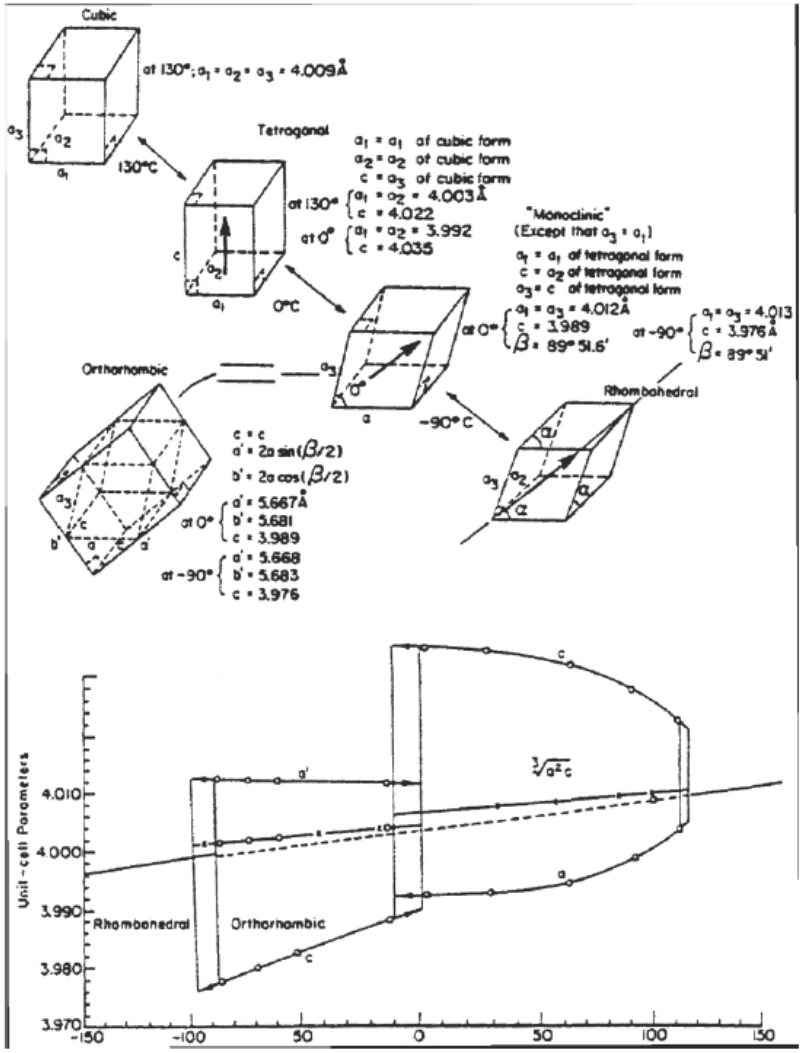

Figure 12

Temperature evolution of the lattice parameters (bottom) of the different crystallographic phases of $BaTiO_3$ and the different crystalline structures (top) from rhombohedral (low temperature phase) to cubic (high temperature phase) (from Refs. [70,75])

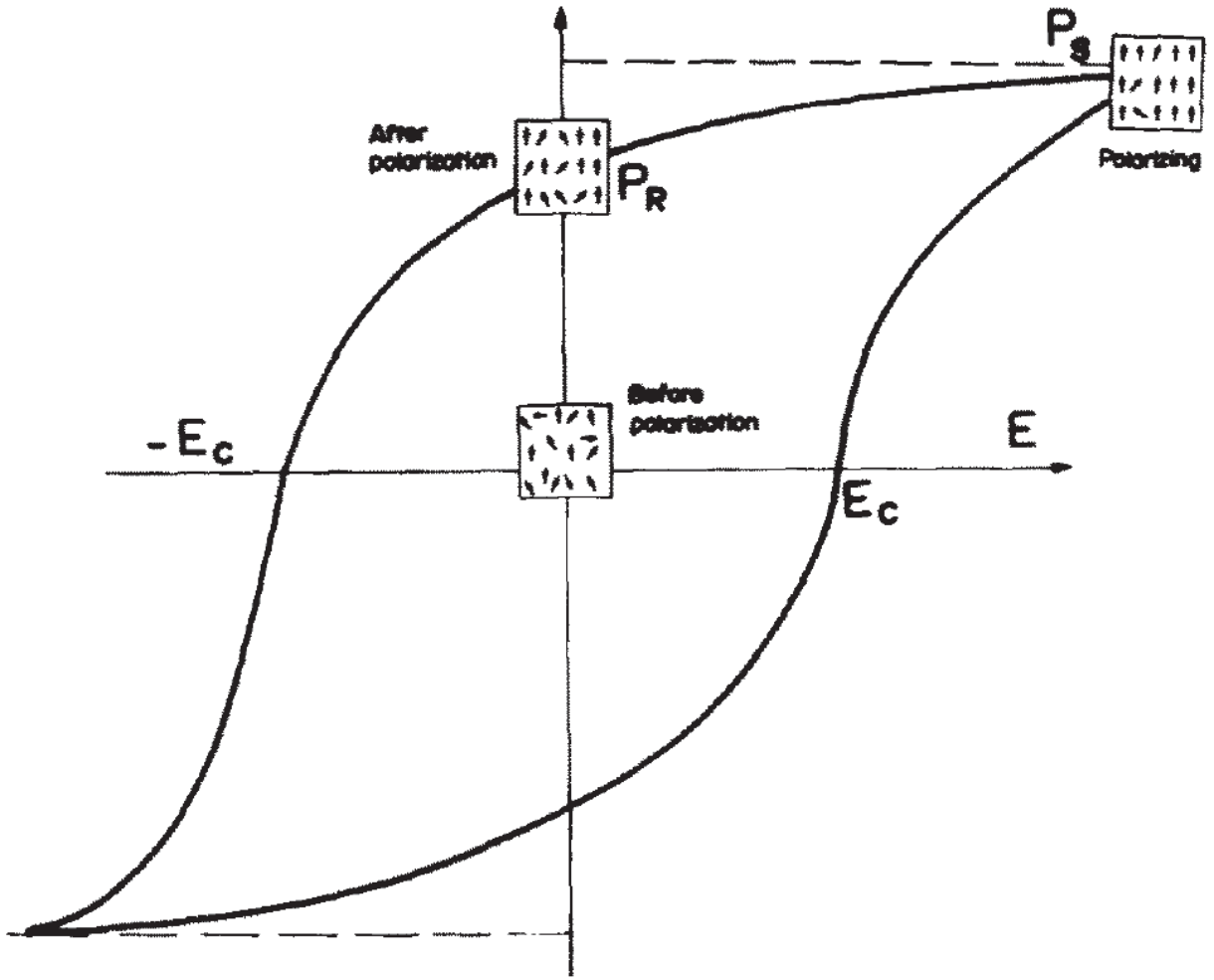

Figure 13

Hysteresis loop and electric polarization of piezoelectric ceramics
(from Ref. [73])

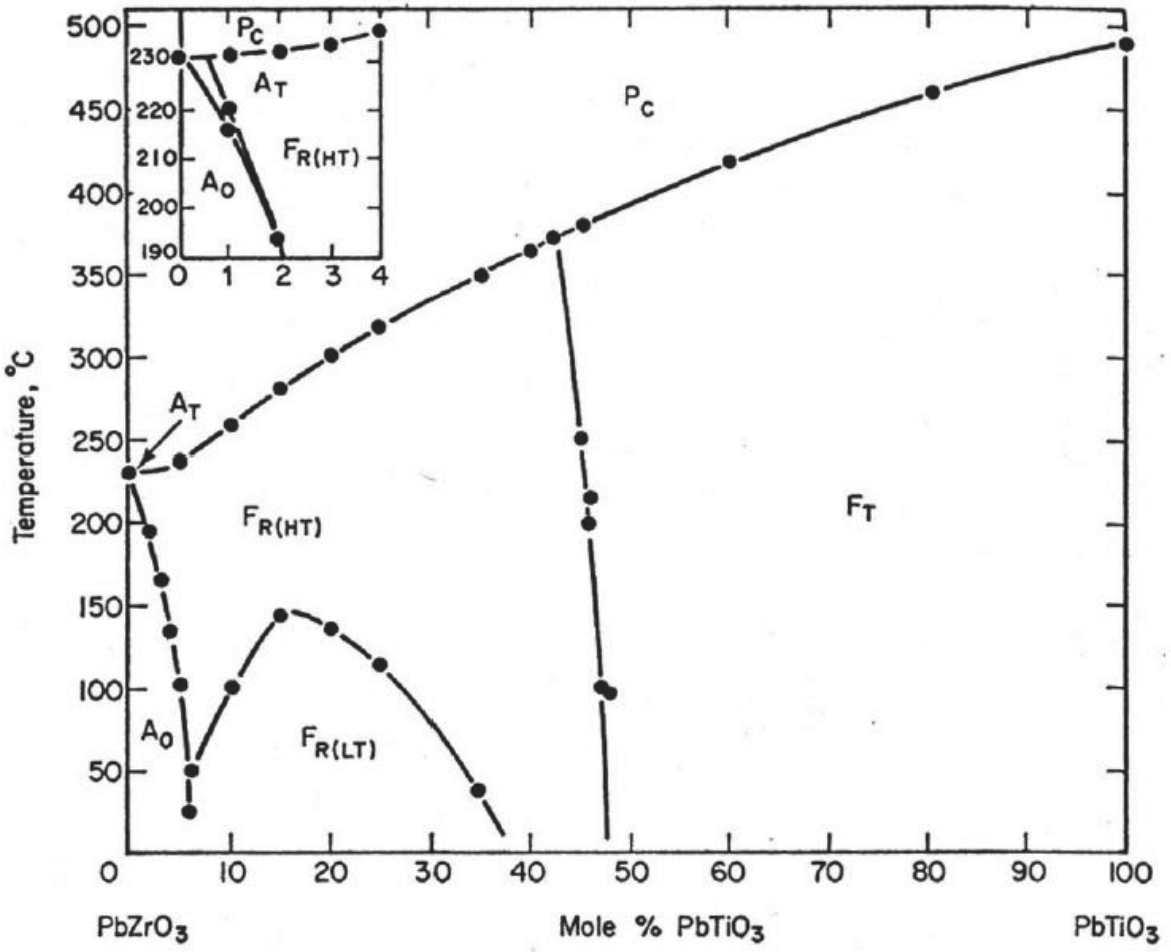

Figure 14.a

Pseudobinary $PbZrO_3$-$PbTiO_3$ system : a) phase diagram showing the morphotropic phase boundary, MPB (from http://electronicstructure.wikidot.com/first-principles-study-of-piezoelectricity-in-pzt),

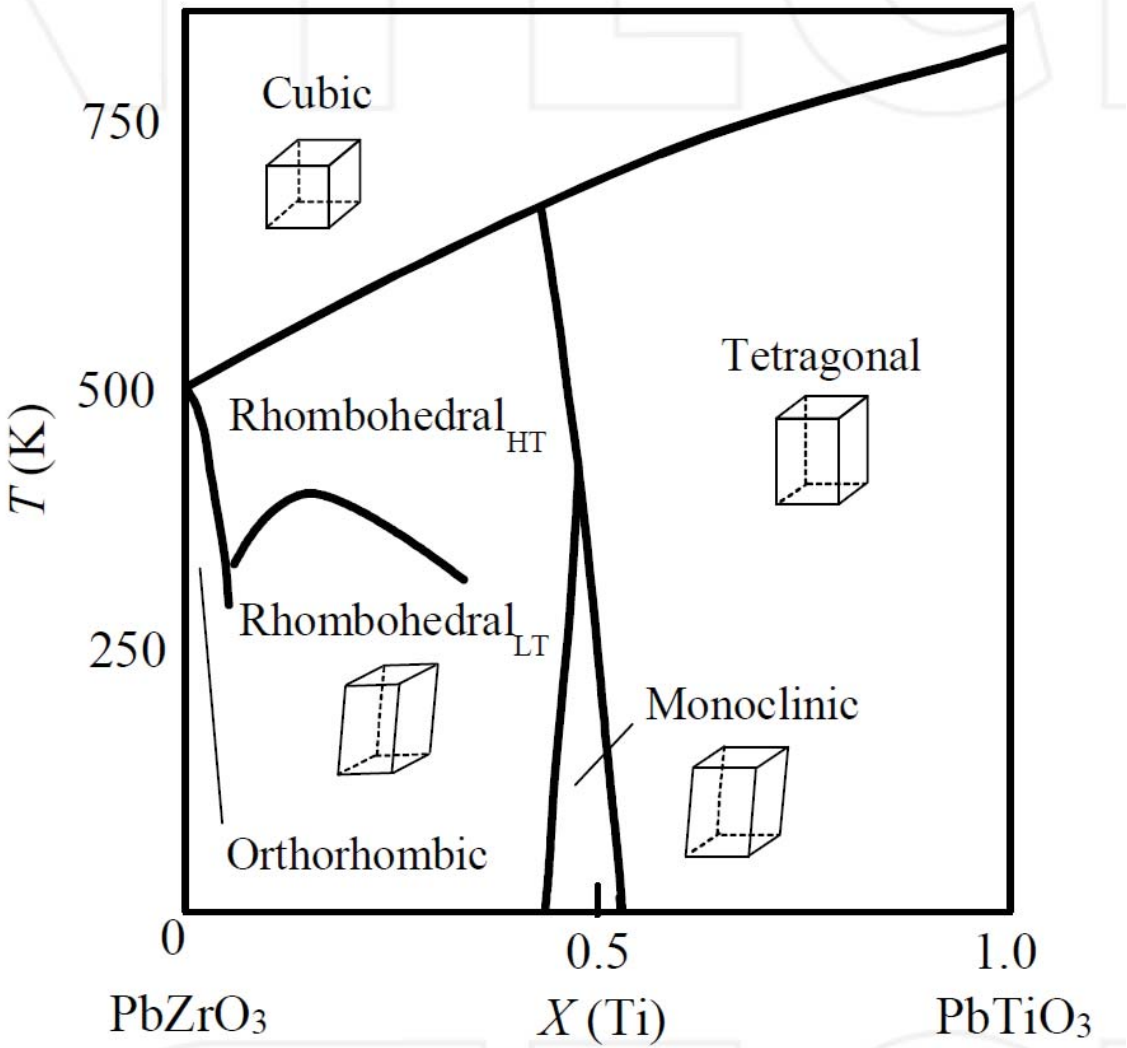

Figure 14.b

Pseudobinary $PbZrO_3$-$PbTiO_3$ system : b) Revised phase diagram showing the crystalline symmetry of the different phases
(from Ref. [79])

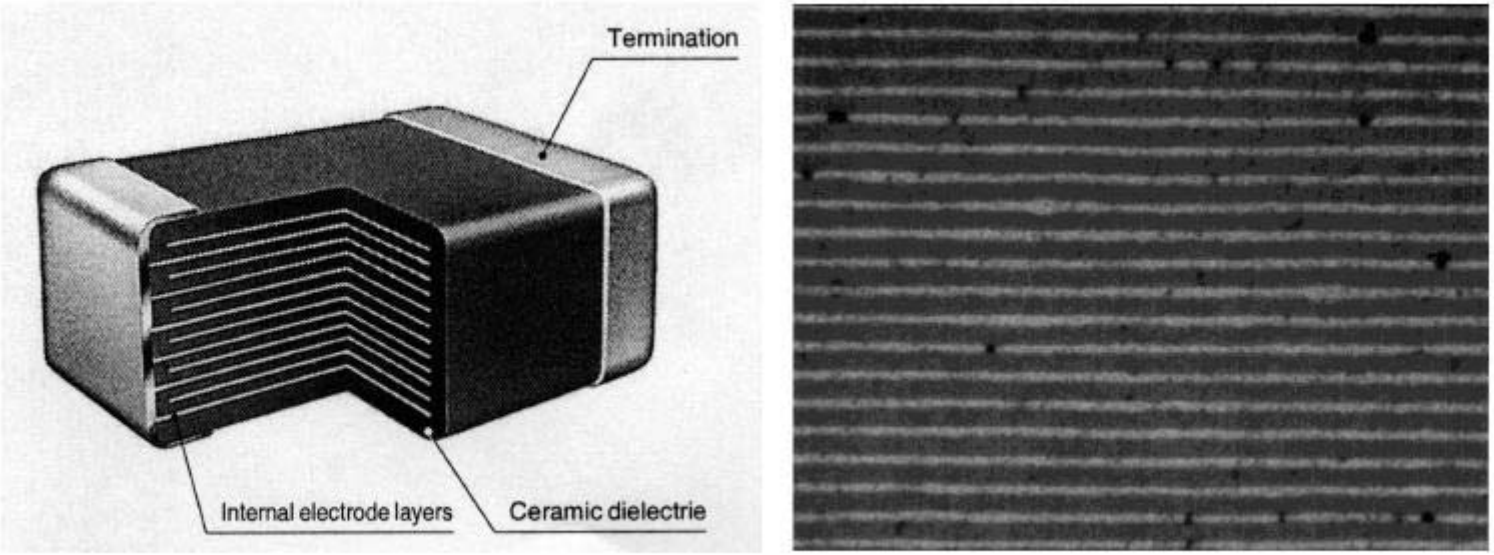

Figure 15

(a) Transversal cross section of a multilayer ceramic capacitor (MLCC) device ;
(b) SEM image of a cross section of a $BaTiO_3$ multilayer ceramic capacitor
(from "History of the first ferroelectric oxide, $BaTiO_3$" ;
http://ceramics.org/wp-content/uploads/2009/03/elec_division_member_papers1.pdf)

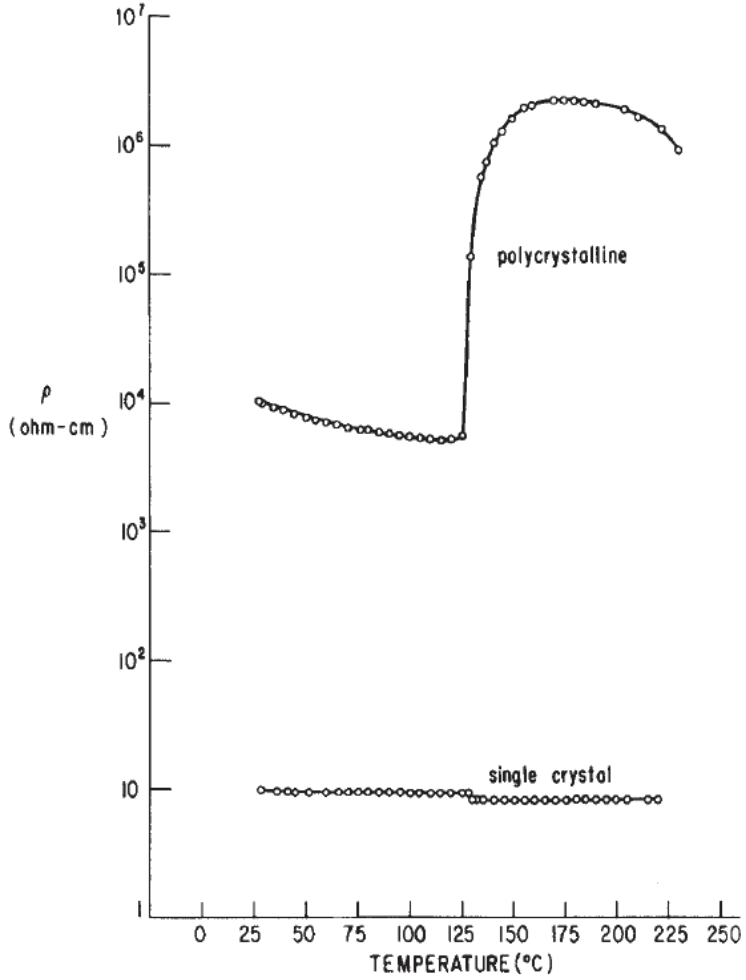

Figure 16.a

Conductivity anomaly in semiconducting (Sm-doped) $BaTiO_3$ ceramic
(from Ref. 75)

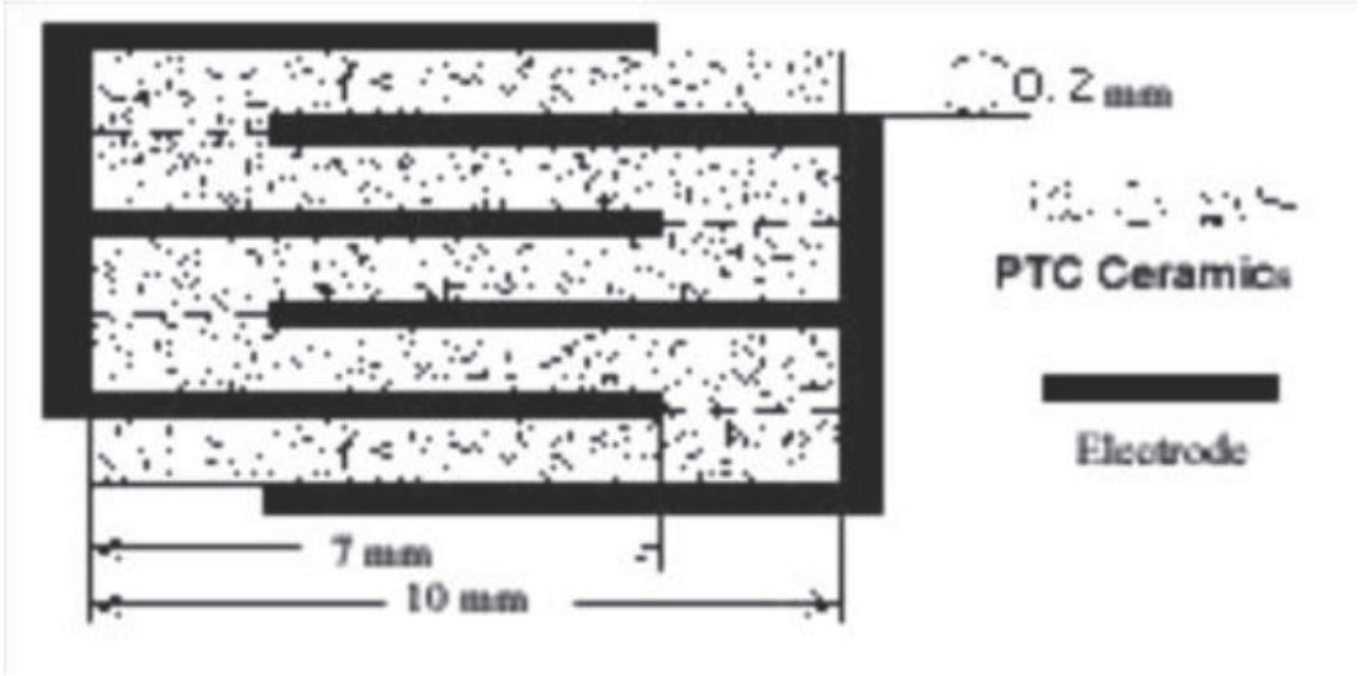

Figure 16.b

Cross section of a $BaTiO_3$-based positive-temperature-coefficient (PTC) device
(from Ref. 94])

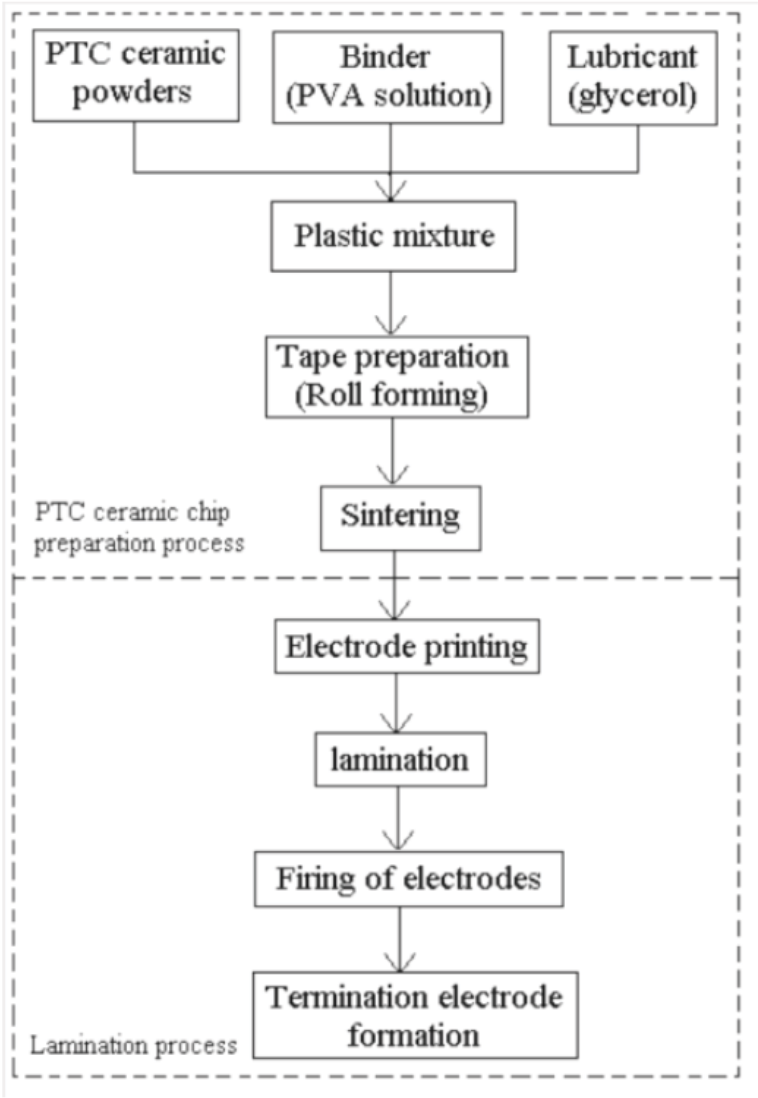

Figure 16.c

Fabrication process of a PTC multilayer chip
(from Ref. 94])

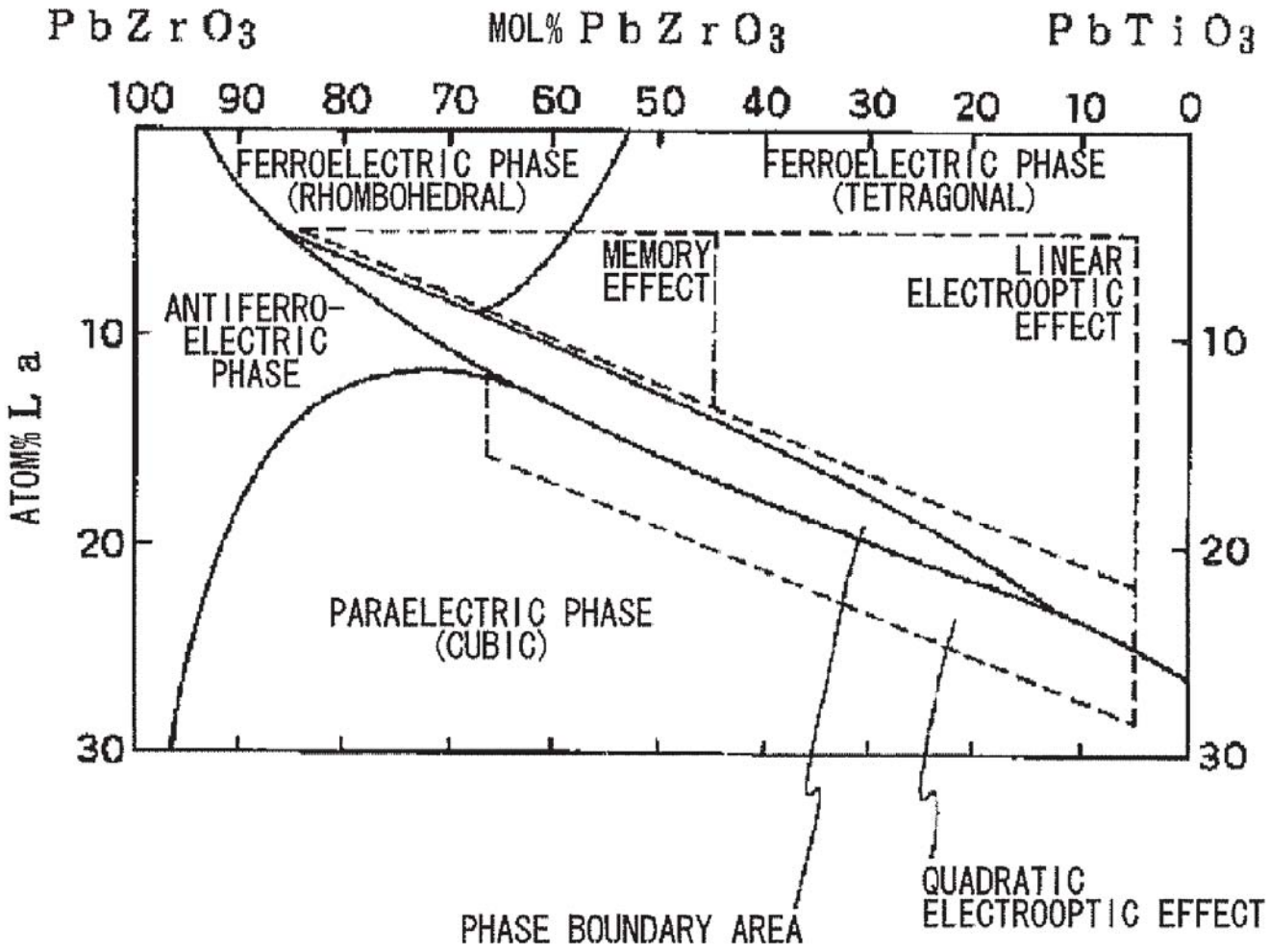

Figure 17

Quaternary phase diagram of the PLZT system
(from “Structure having light modulating film and optical controlling device using same”, Patent EP-1662298-A1 ; fig.8 / see http://www.google.com/patents/EP1662298A1)

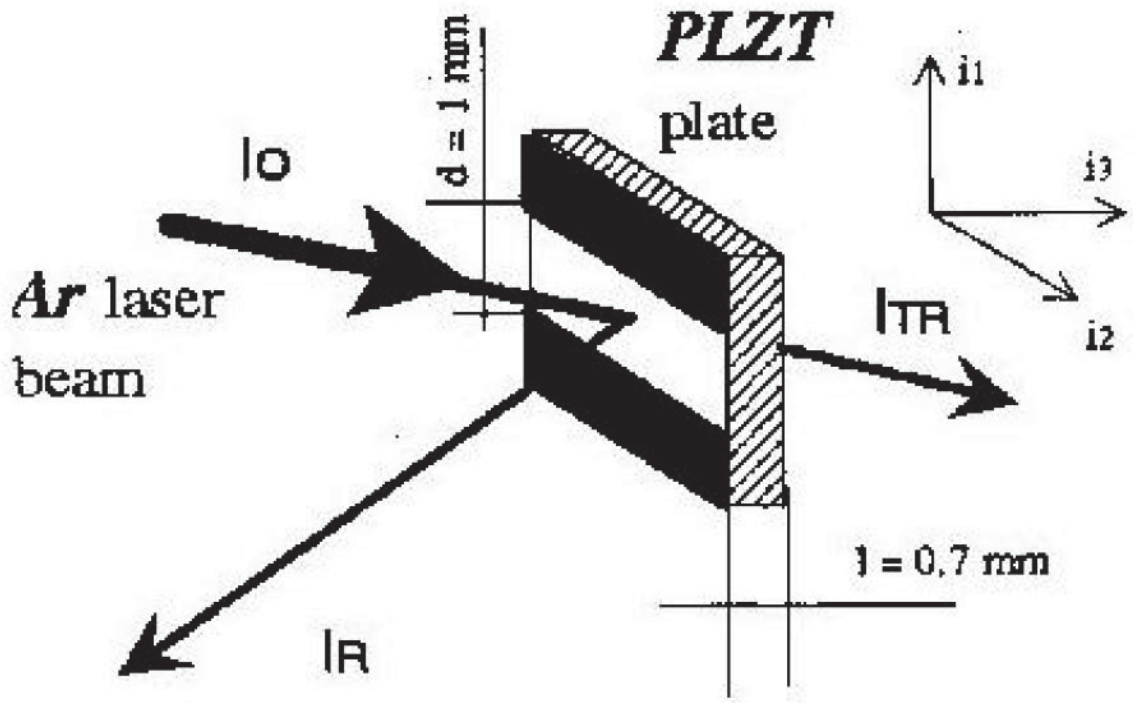

Figure 18.a

Schematic diagram of a PLZT modulator (PLZT : lead lanthanum zirconium titanate)
(from http://www.marekczerwiec.com/artykuly/TRANSPARENT_PLZT_CERAMICS.pdf)

Figure 18.b

An example of applications for transparent PLZT, the visor anti-flash
(from http://www.flightgear.dk/flash.htm)

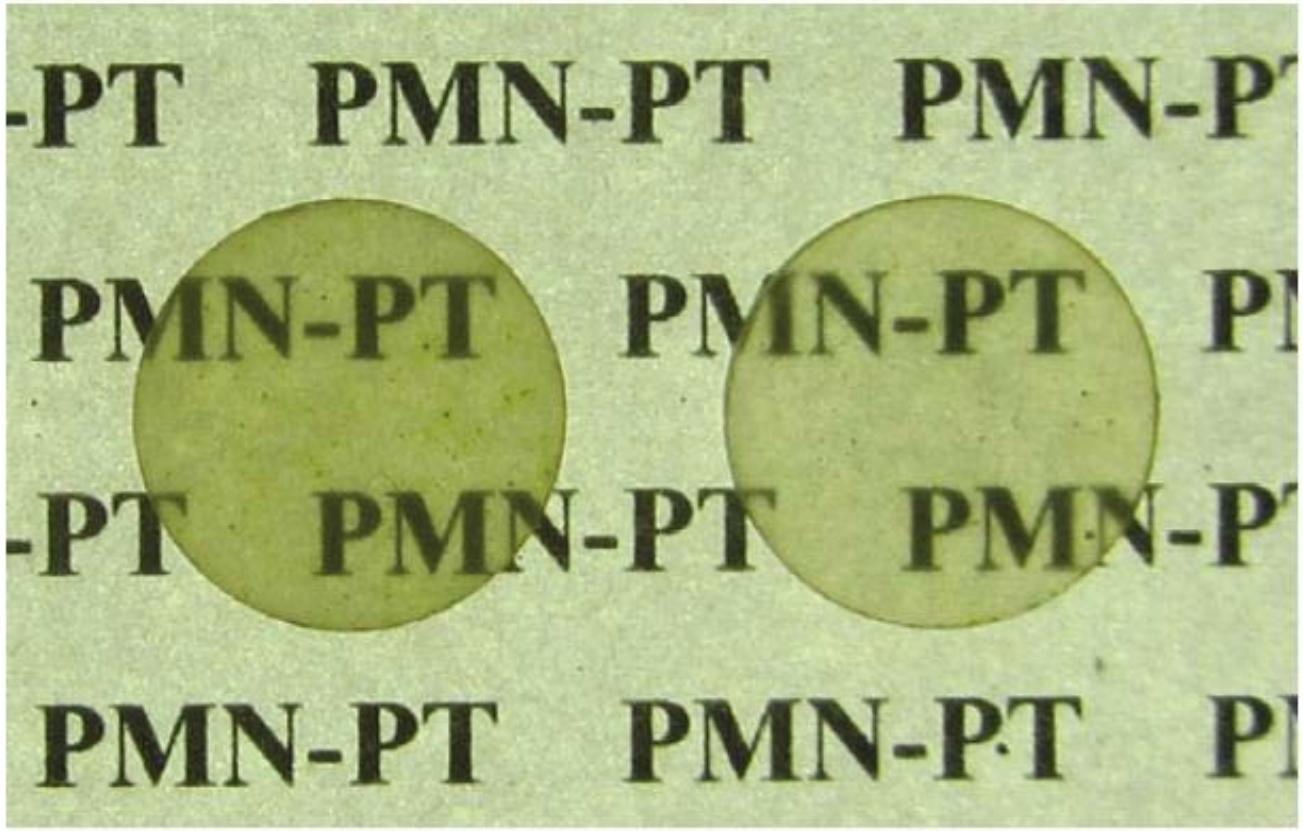

Figure 18.c

La-undoped (left) and 3 mol% La-doped (right) 0.9PMN-0.1PT ceramics
(PMN : $Pb(Mg_{1/3}Nb_{2/3})O_3$; PT : $PbTiO_3$)
(from Ref. [110])

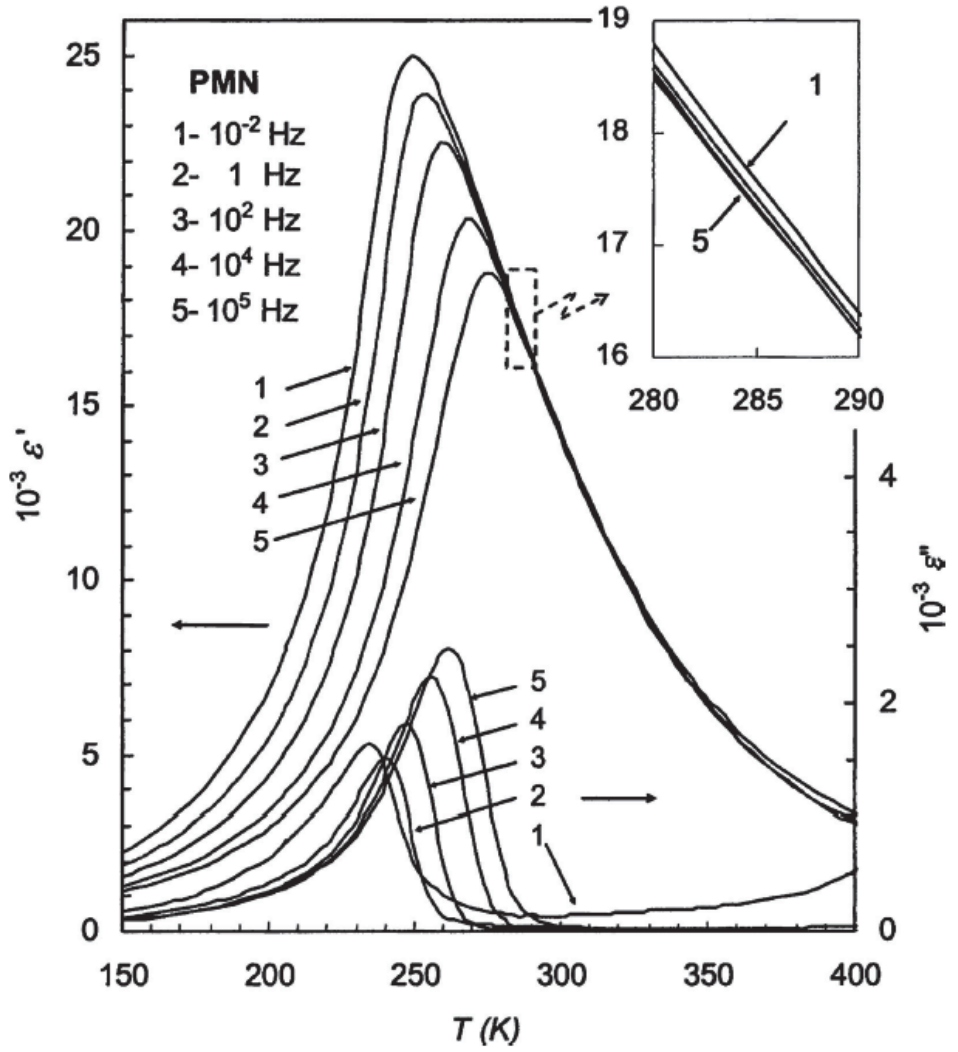

Figure 19

Temperature dependence of real and imaginary parts of the relative dielectric permittivity in a crystal of $Pb(Mg_{1/3}Nb_{2/3})O_3$ (PMN). Insert : universal relaxor dispersion (from Ref. [120])

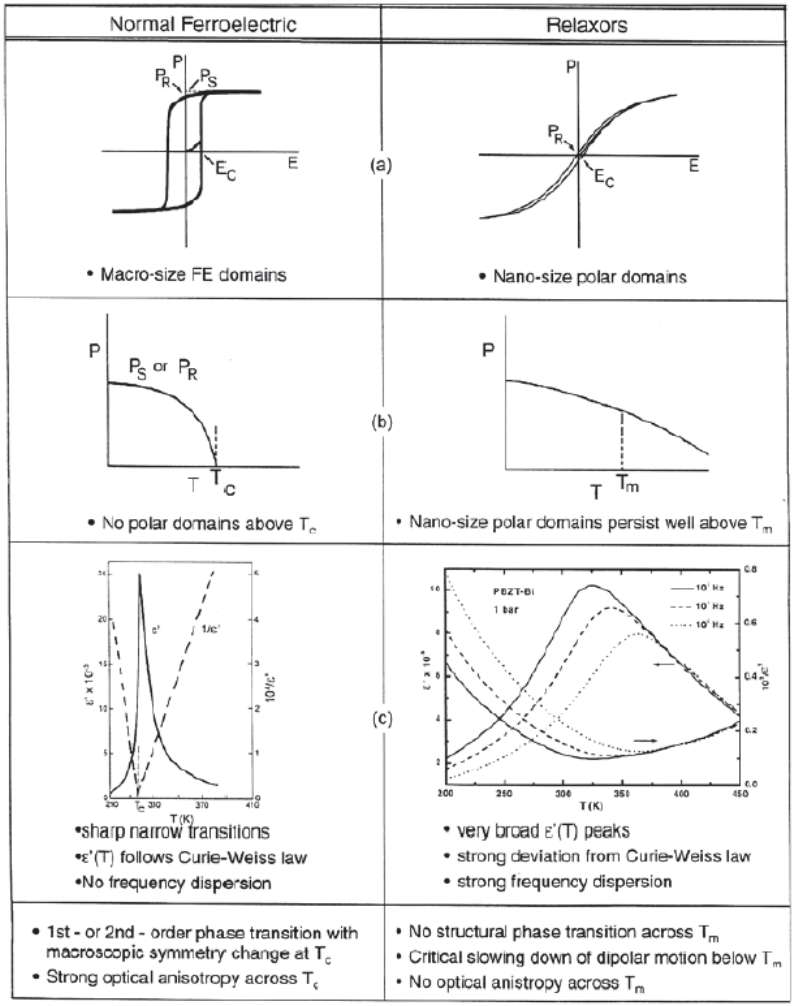

Figure 20

Comparative schemes of the relaxor and normal ferroelectric compounds
(from http://guava.physics.uiuc.edu/~nigel/courses/563/Essays_2005/PDF/delgado.pdf)

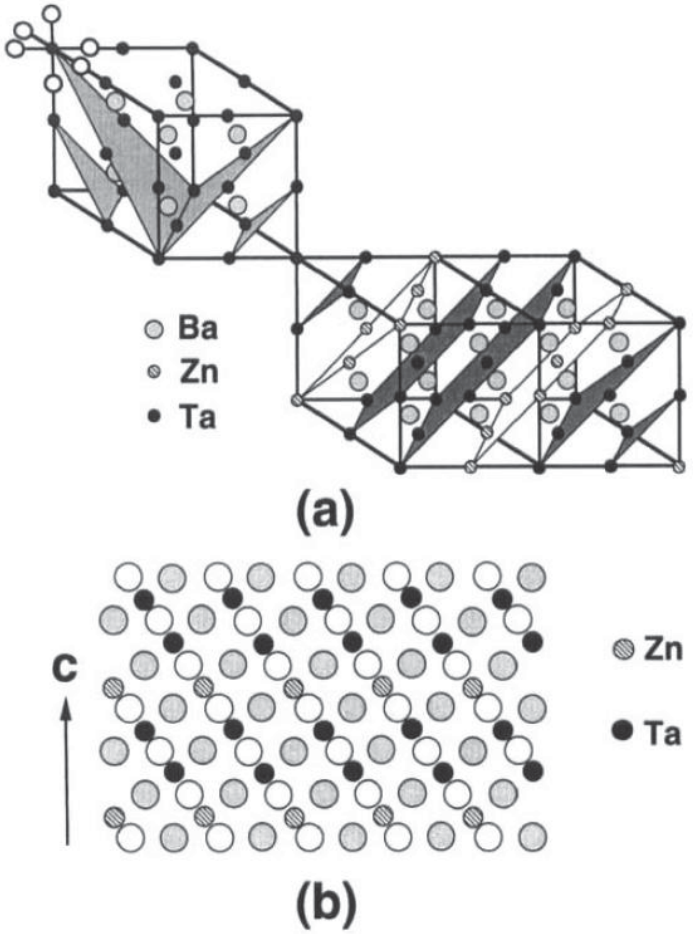

Figure 21.a

Schematic illustration of a 1:2 cation-ordering in $Ba(Zn_{1/3}Ta_{2/3})O_3$. Upper left shows two of the possible {111} directions for the ordering of Zn and Ta. Center image shows a 1:2 ordering for one of the orientational variants (oxygen anions omitted for clarity). Bottom shows an idealized $[110]_{subcell}$ projection of the ordered structure : open circles, oxygen anions; shaded circles, Ba cations; the anions that project onto the A-site positions are omitted for clarity
(from Ref. [136]).

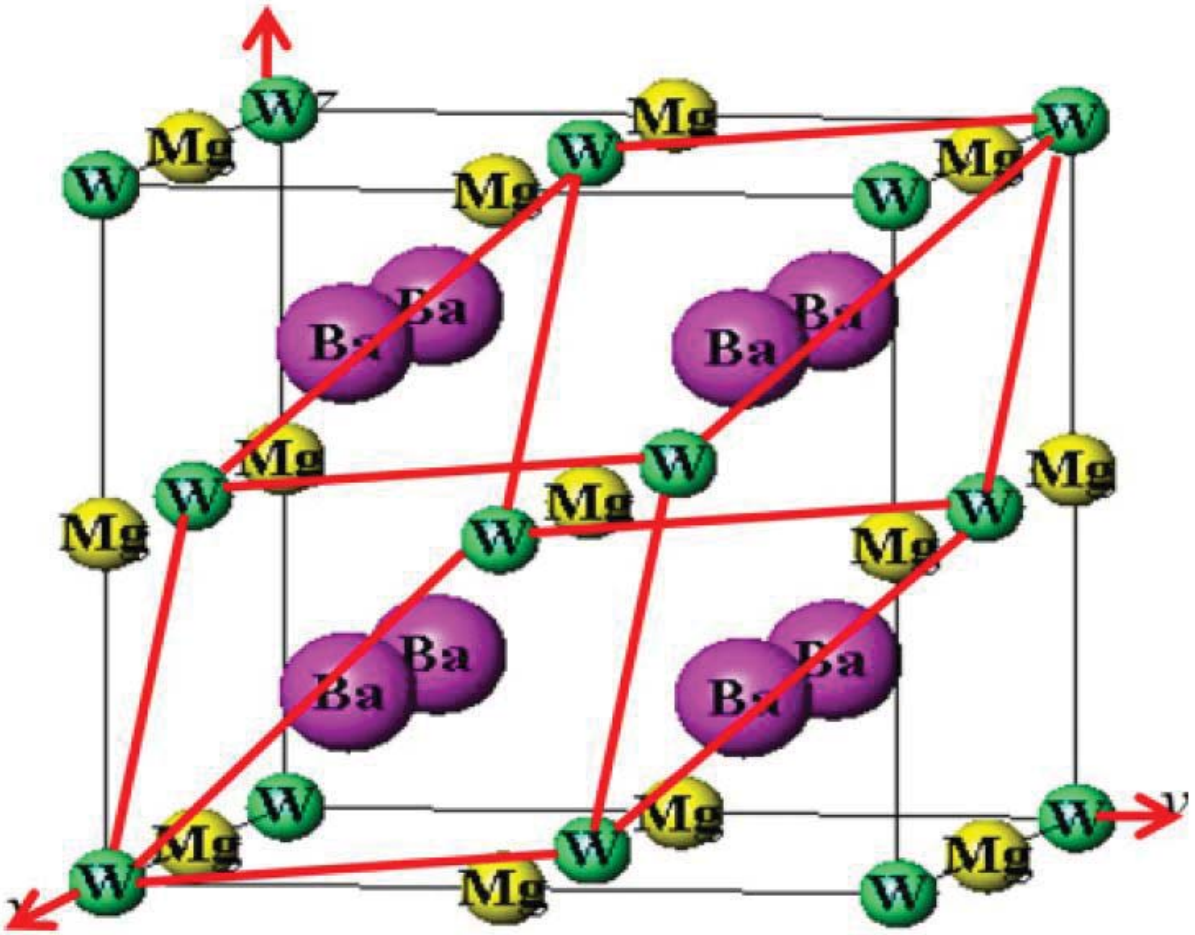

Figure 21.b

Double perovskite structure of $Ba(Mg_{1/2}W_{1/2})O_3$ (BMW); primitive cell in the unit cell (only cations are shown) (from Ref. [137])

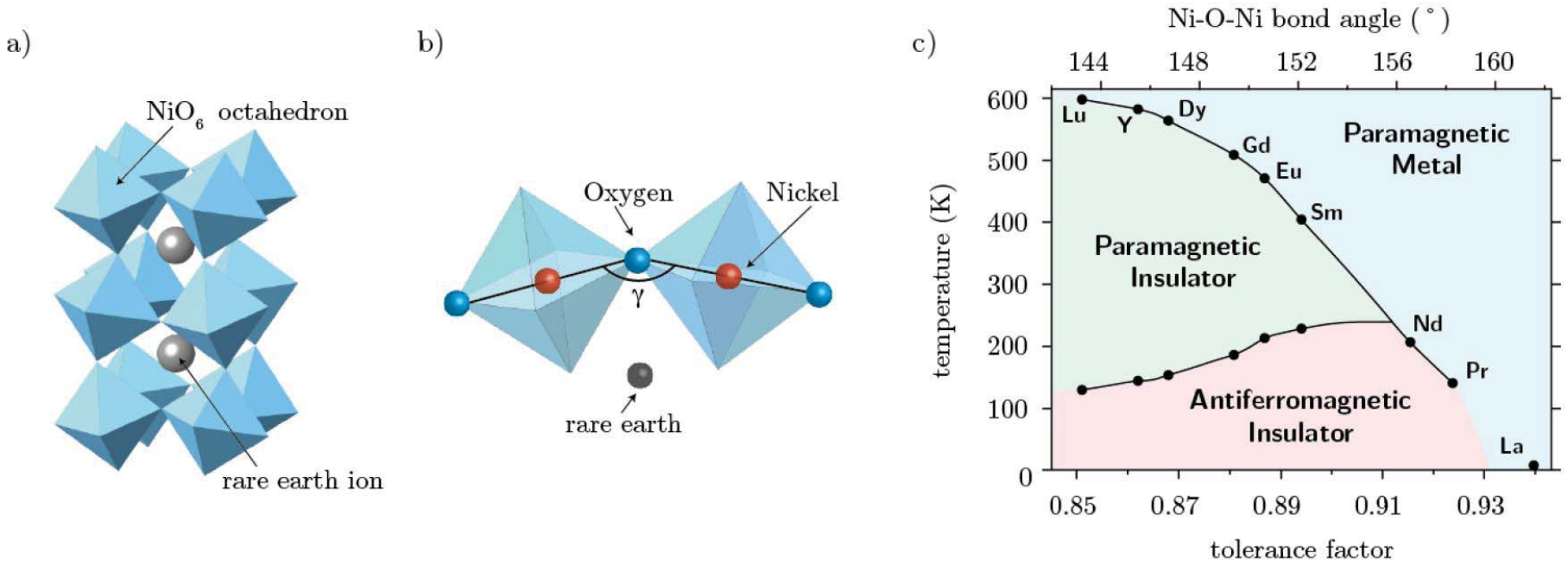

Figure 22

a) Unit cell of $RNiO_3$ with distorted NiO_6 octahedra. b) The Ni-O-Ni bond angle as a measure of the lattice distortion ; for different rare-earths the lattice distortion (described by γ) changes. c) Phase diagram of $RNiO_3$ as a function of the tolerance factor
(from http://physics.unifr.ch/de/page/547/)

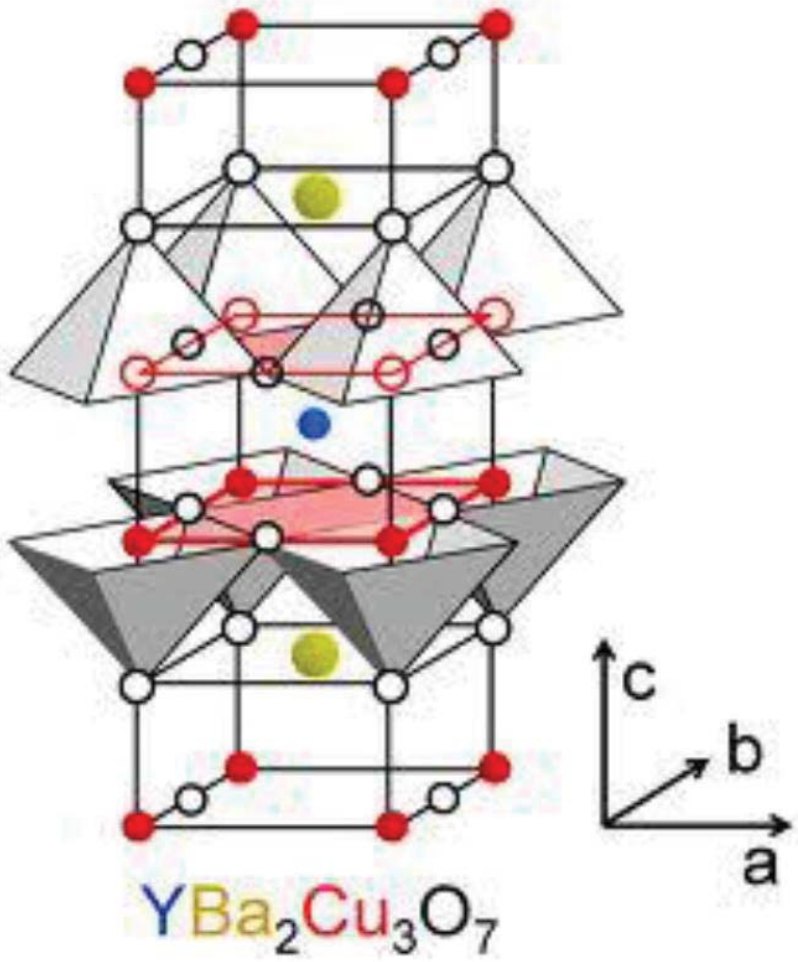

Figure 23

Crystalline structure of superconducting $YBa_2Cu_3O_{7-\delta}$
(see, for instance, J.D. Jorgensen et al, Phys. Rev. B, 41 (1990) 1863)

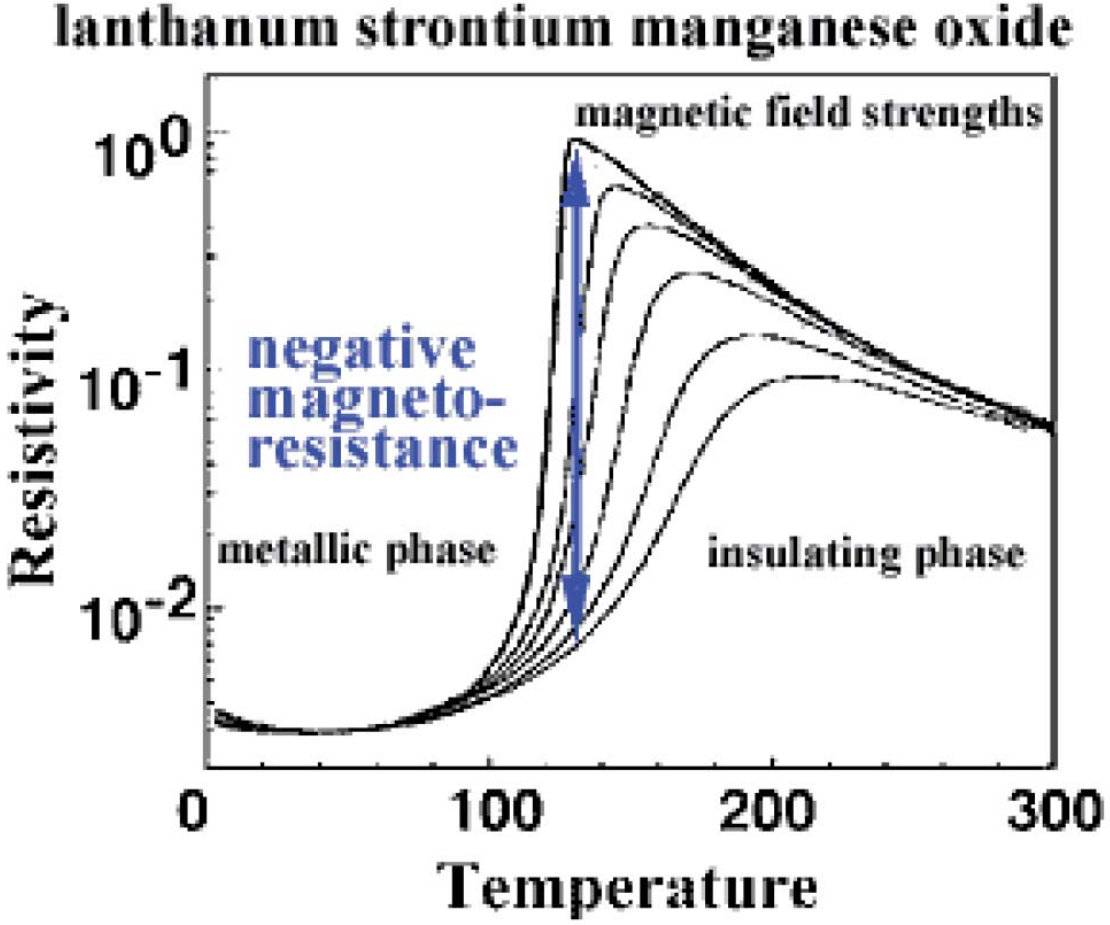

Figure 24

Temperature dependence of the resistivity of $La_{1-x}Sr_xMnO_3$ with x=0.3, at various magnetic fields
(from http://www2.lbl.gov/Science-Articles/Archive/colossal-magnetoresistance.html)

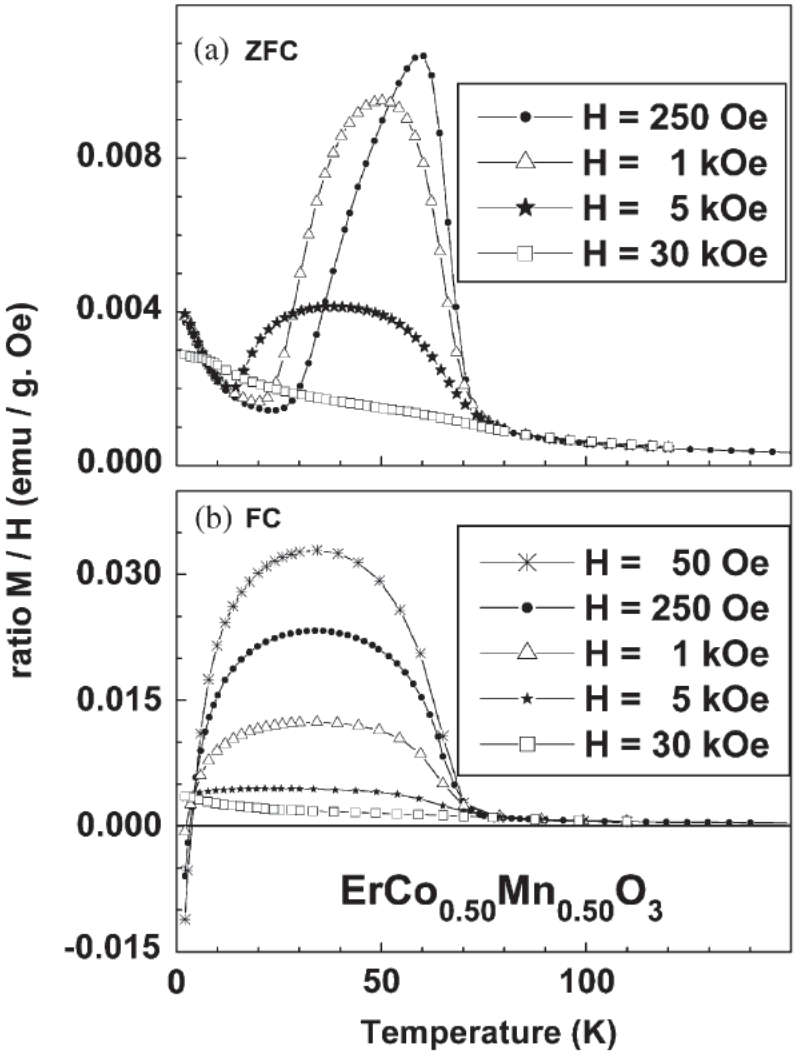

Figure 25

Temperature dependence of the ZFC (a) and FC (b) magnetizations, under given applied fields, for composition $ErCo_{0.50}Mn_{0.50}O_3$ (from Ref. [175])

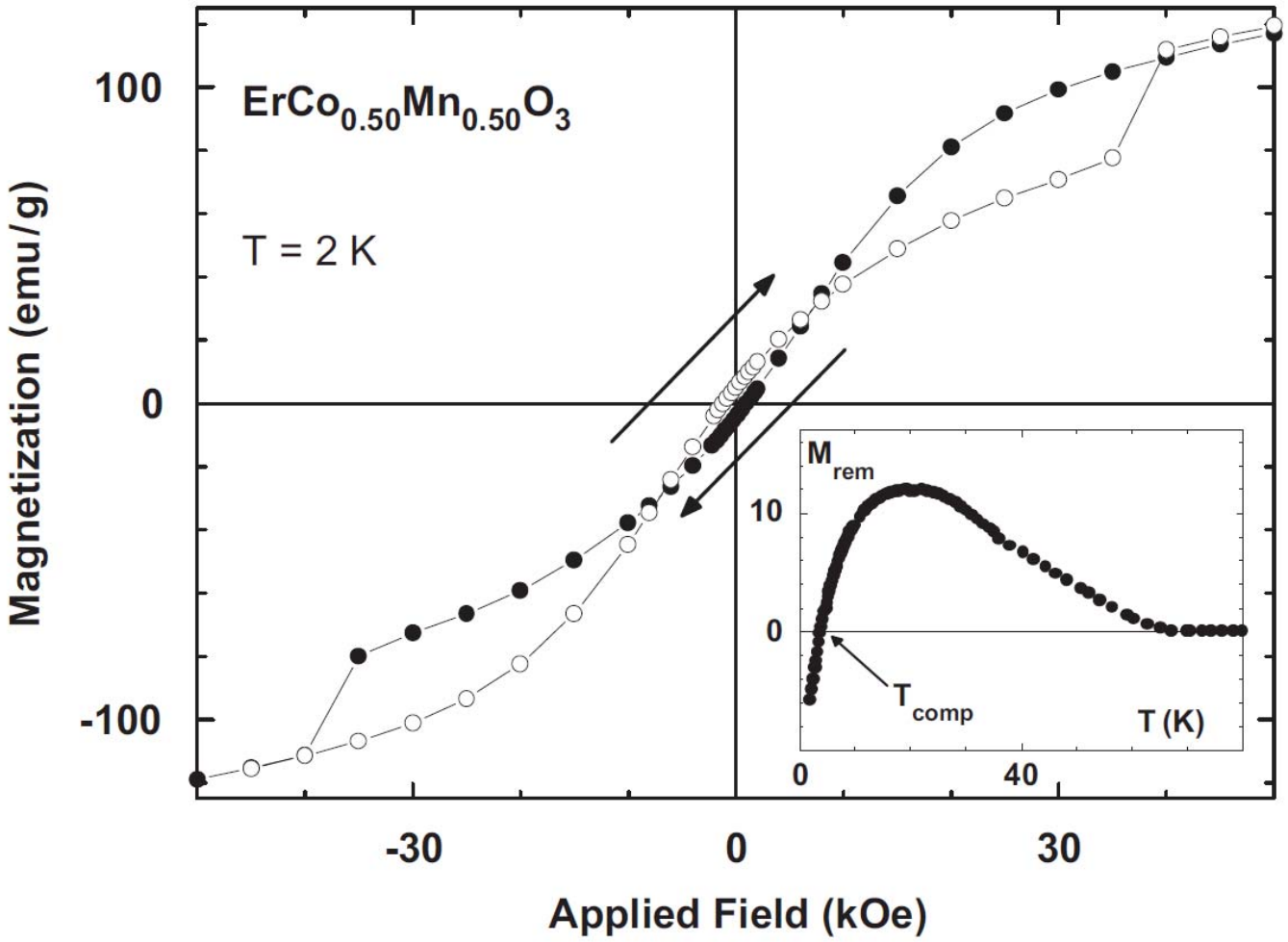

Figure 26

Magnetization loop at 2 K for $ErCo_{0.50}Mn_{0.50}O_3$ while increasing (open symbols) and decreasing the magnetic field (solid symbols). The inset shows the temperature (T_{comp}) of reverse magnetization
(from Ref. [176])

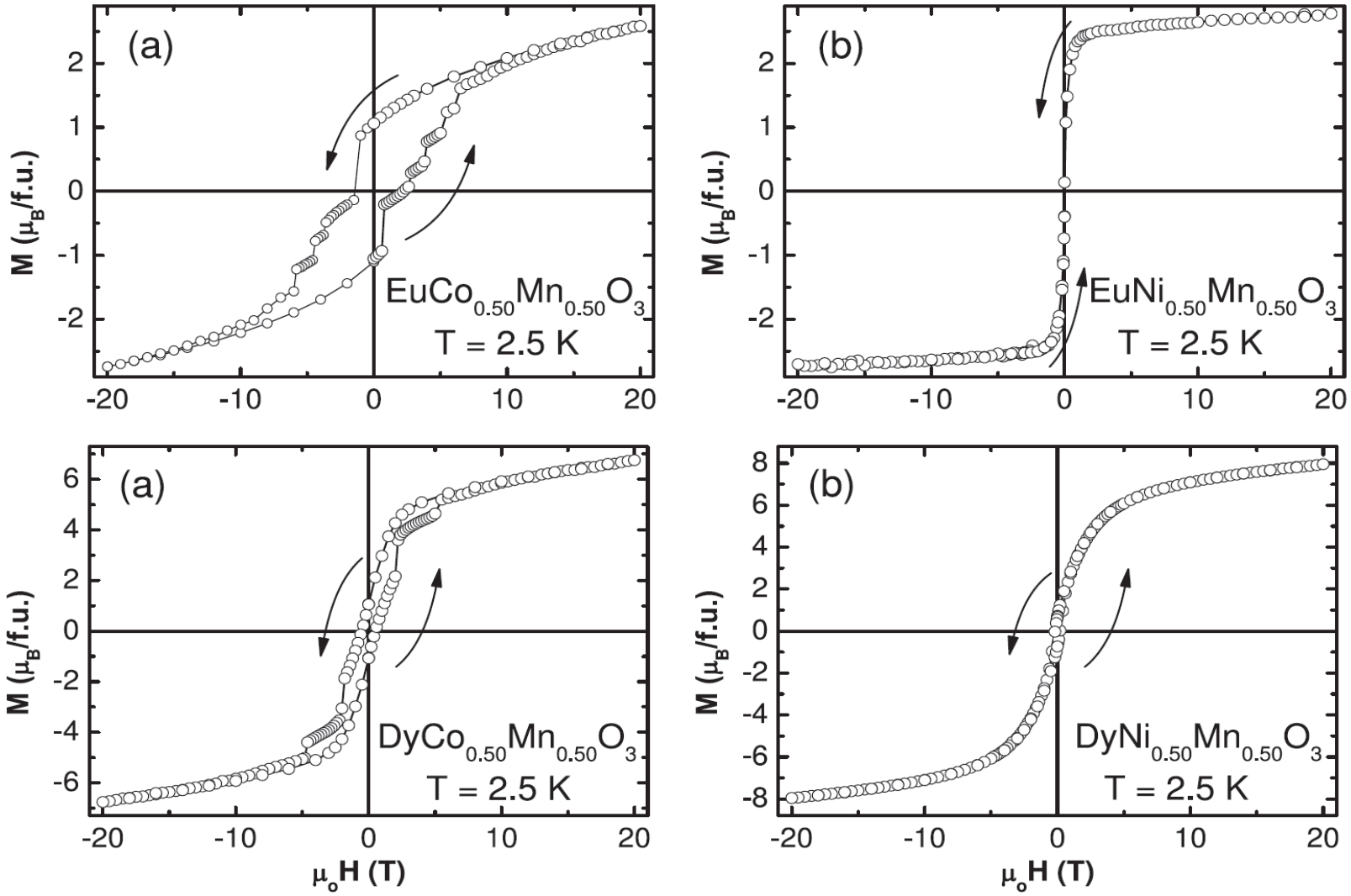

Figure 27

Top : Magnetization loops at 2.5 K for (**a**) $EuCo_{0.50}Mn_{0.50}O_3$ and (**b**) $EuNi_{0.50}Mn_{0.50}O_3$.
Bottom : Magnetization loops at 2.5 K for (**a**) $DyCo_{0.50}Mn_{0.50}O_3$ and (**b**) $DyNi_{0.50}Mn_{0.50}O_3$
(from Ref. [177])

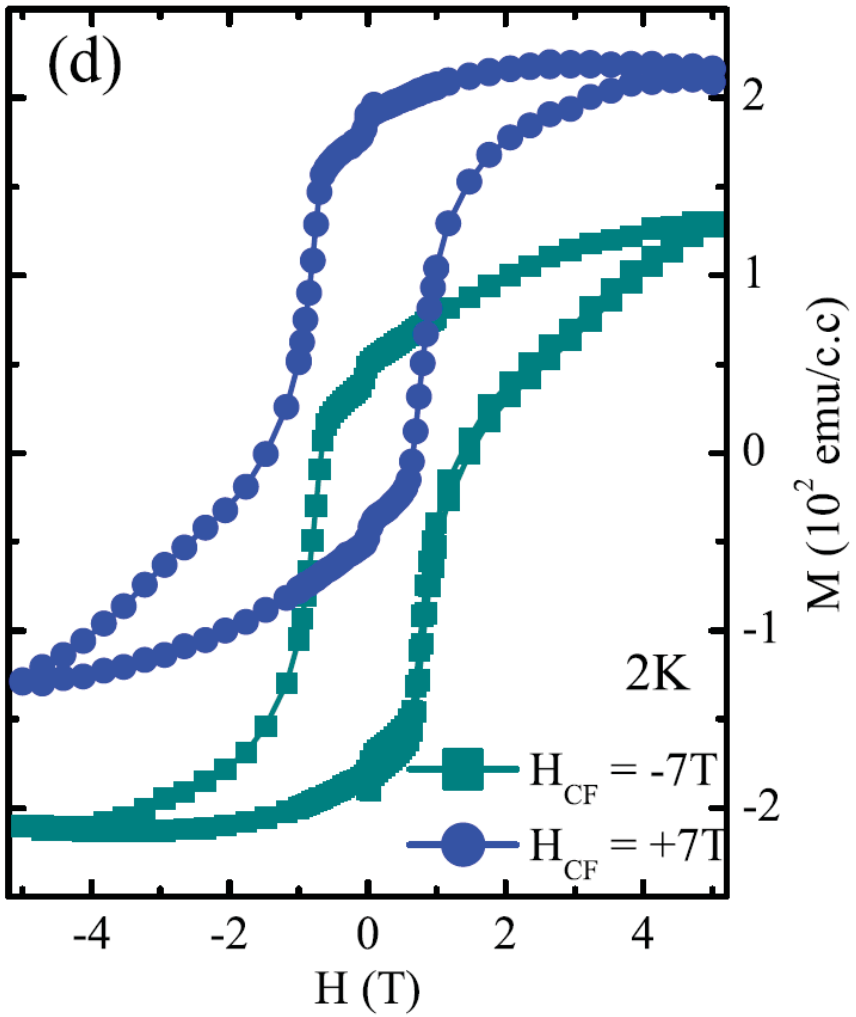

Figure 28

Maximum M_{shift} (~35%) for the optimized bilayer [$La_{0.3}Sr_{0.7}FeO_3$(110 nm)/$SrRuO_3$(10 nm)] (from Ref. [181])

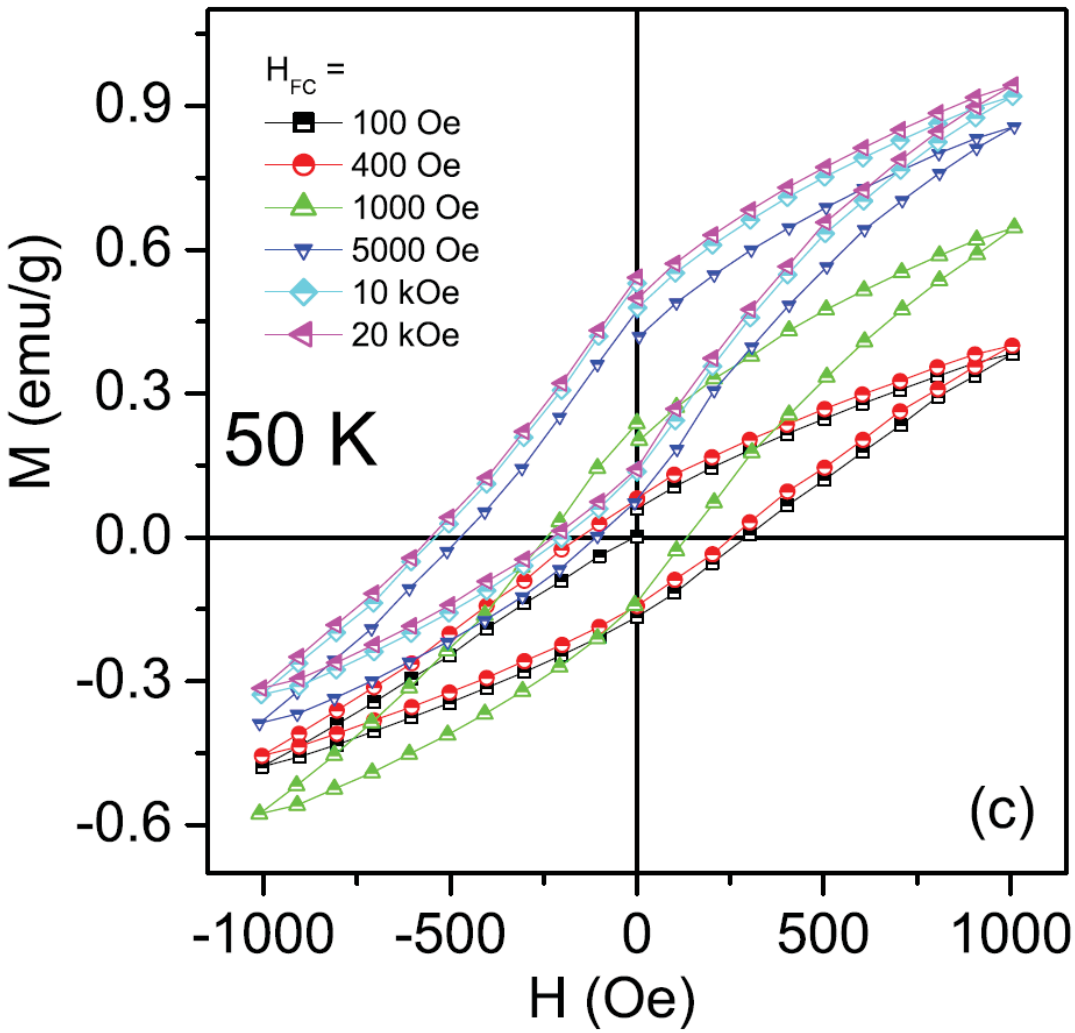

Figure 29

Exchange bias and memory effects in the double perovskite Sr_2FeCoO_6. The field-cooled hysteresis curves at different cooling fields H_{FC} display vertical displacement that signify FM clusters present in the system (from Ref. [183])